OPTIMAL DYNAMIC SOARING FOR FULL SIZE SAILPLANES

THESIS

Randel J. Gordon, Captain, USAF

AFIT/GAE/ENY06-S04 GAE 06S

DEPARTMENT OF THE AIR FORCE
AIR UNIVERSITY

AIR FORCE INSTITUTE OF TECHNOLOGY

Wright-Patterson Air Force Base, Ohio

AFIT/GAE/ENY06-S04 GAE 06S

OPTIMAL DYNAMIC SOARING FOR FULL SIZE SAILPLANES

THESIS

Presented to the Faculty

Department of Aeronautical and Astronautical Engineering

Graduate School of Engineering and Management

Air Force Institute of Technology

Air University

Air Education and Training Command

In Partial Fulfillment of the Requirements for the

Degree of Master of Science in Aeronautical Engineering

Randel J. Gordon, BS

Captain, USAF

September 2006

AFIT/GAE/ENY06-S04 GAE 06S

MANNED SAILPLANE DYNAMIC SOARING

Randel J. Gordon, BS
Captain, USAF

Approved:

Paul Blue 29 Aug 06
Blue, Paul Maj, USAF (Chairman) date

Bradley S. Liebst 29 Aug 06
Liebst, Bradley, PhD (Member) date

Donald L. Kunz 29 Aug 2006
Kunz, Donald, PhD (Member) date

29 Aug 06
Millman, Daniel Lt.Col., USAF, PhD (Member) date

AFIT/GAE/ENY06-S04 GAE 06S

Abstract

Dynamic soaring is a unique flying technique designed to allow air vehicles to extract energy from horizontal wind shears. Dynamic soaring has been used by seabirds like the Albatross to fly hundreds of kilometers a day across the ocean. Small hobby radio controlled sailplanes have also used this technique to achieve sustained speeds of over 200 miles per hour from just a simple hand toss. Dynamic soaring, however, has never before been studied for use on full size aircraft. The primary goal of this research was to prove or disprove the viability of dynamic soaring for enhancing a full size aircraft's total energy by using a manned sailplane as a demonstration air vehicle. The results of this study will have a direct impact on the sport of soaring, as well as the design of the next generation of large, sailplane-like, robotic planetary explorers for the National Aeronautics and Space Administration (NASA).

This research began with a point mass optimization study of an L-23 Super Blanik sailplane. The primary goal of this study was to develop and analyze optimal dynamic soaring trajectories. A prototype 6 degrees of freedom (DOF) flight simulator was then developed. This simulator helped to validate the dynamic soaring aircraft equations of motion derived for this research and built operational simulator development experience. This experience was then incorporated into a full dynamic soaring research simulator developed at the NASA Dryden Flight Research Facility (NASA DFRC). This NASA simulator was used to develop advanced dynamic soaring flight displays, flight test techniques, and aircrew coordination procedures. Flight test were successfully accomplished using an instrumented L-23 Super Blanik sailplane and advanced weather monitoring equipment. Through modeling and simulation, flight test, and mathematical analysis, this research provided the first documented proof of the energy benefits realized using dynamic soaring techniques in full size sailplanes.

To my wife and son

Acknowledgments

I would like to extend sincere thanks to Major Paul Blue for helping me to understand dynamic optimization theory and providing immeasurable editing and technical assistance during the development of this thesis. Thank you so very much for engaging this project with incredible determination and stamina. I only hope that future AFIT to USAF Test Pilot School students will appreciate how much of an asset you are to the program. To Dr. Brad Liebst, I would like to extend my heart felt appreciation for giving me all the tools necessary to undertake the advanced aerodynamics required for this project. You never turned me away anytime I had a question and your patience, knowledge, and demanding pursuit of academic excellence in your students will always be an example for me to strive towards. Furthermore, without the help of Dr. Donald Kunz, my successful completion of the AFIT to USAF Test Pilot School program would never have happened. Thanks for guiding me through the complex academic sequences and course pre-requisite requirements at both AFIT and Wright State so that I would have the necessary classes and credentials to truly grasp this thesis. You took the time to make sure I was taken care of and future AFIT/USAF TPS students will benefit much from your leadership. Thanks are in order to Lt.Col. Dan Millman for providing excellent technical and formatting feedback in order to make this thesis more organized and professional in its presentation. In addition, the efforts of the AFRL VACD flight simulator engineers, especially 1st Lt Jay Kemper, were extraordinary. 1st Lt Kemper’s hard work and expertise in aerodynamics were the foundation of the modeling and simulation work accomplished on this project. Without the prototype sailplane flight simulation work accomplished at Wright Patterson AFB by 1st Lt Kemper, the simulator work

accomplished at Edwards AFB would have failed and the project as a whole would have faltered. Good luck in your future endeavors!

I would also be remiss if I didn't thank the members of the SENIOR ShWOOPIN flight test team: Lt.Col Mark Stucky, Mr. Gary Aldrich, Mr. Russ Erb, Mr. Jim Payne, Mr. Joe Wurts, Major Robert Fails (USMC), Capt. Jason Eckberg, Capt. Chris Smith, Capt. Solomon Baase, and Capt. Matt Ryan. Through their outstanding flight skill, technical knowledge, and professional attitude, this thesis seamlessly matured with almost unbelievable speed from esoteric mathematical theory to proven flight test reality. I would also like to thank Mr. James Murray and Mr. Russ Franz, NASA DFRC, for their invaluable assistance with aircraft instrumentation, data collection, and analysis. In addition, I owe the entirety of the Design of Experiments work accomplished on this thesis to Capt. E. T. Waddell. These three talented engineers were the foundation on which the SENIOR ShWOOPIN test team built our successful flight test program.

Last, but certainly not the least, I would like to give special acknowledgements to God, my loving wife, and my son for helping me conquer this tremendous professional challenge. I gain strength through my faith in my creator and the love and support of my family. Without them, I am nothing.

Table of Contents

List of Figures

List of Tables

List of Symbols

Symbol	Definition
Ail	Aileron Deflection (rad)
C_D	Drag Coefficient
C_{D_0}	Drag Coefficient at Zero Angle of Attack (/rad)
C_{D_α}	Drag coefficient due to Angle of Attack (/rad)
$C_{D_{\delta E}}$	Drag Coefficient due to Elevator Deflection (/rad)
C_L	Lift Coefficient
C_{Llf}	C_L required for level flight at the maneuver start airspeed
C_{L_0}	Lift Coefficient at Zero Angle of Attack (/rad)
C_{L_α}	Lift Coefficient due to Angle of Attack (/rad)
$C_{L_{\delta e}}$	Lift Coefficient due to Elevator Deflection (/rad)
$C_{\bar{L}_P}$	Roll Moment Coefficient due to Roll Rate (/rad)
$C_{\bar{L}_R}$	Roll Moment Coefficient due to Yaw Rate (/rad)
$C_{\bar{L}_{\delta A}}$	Roll Moment Coefficient due to Aileron Deflection (/rad)
$C_{\bar{L}_{\delta R}}$	Roll Moment Coefficient due to Rudder Deflection (/rad)
$C_{\bar{L}_\beta}$	Roll Moment Coefficient due to Sideslip (/rad)
C_{M_0}	Pitch Moment Coefficient at Zero Angle of Attack (/rad)
C_{M_α}	Pitch Moment Coefficient due to Angle of Attack (/rad)

List of Symbols (cont.)

Symbol	Definition
$C_{M_{\delta E}}$	Pitch Moment Coefficient due to Elevator Deflection (/rad)
C_{M_Q}	Pitch Moment Coefficient due to Body Fixed Pitch Rate (/rad)
C_{N_0}	Yaw Moment Coefficient at Zero Angle of Attack (/rad)
C_{N_P}	Yaw Moment Coefficient due to Roll Rate (/rad)
C_{N_R}	Yaw Moment Coefficient due to Yaw Rate (/rad)
C_{N_β}	Yaw Moment Coefficient due to Sideslip (/rad)
$C_{N_{\delta A}}$	Yaw Moment Coefficient due to Aileron Deflection (/rad)
$C_{N_{\delta R}}$	Yaw Moment Coefficient due to Rudder Deflection (/rad)
C_P	Test Pitot-static nose boom pressure correction coefficient (0.095 *from flight test*)
C_Y	Side Force Coefficient
C_{Y_0}	Side Force Coefficient at Zero Angle of Attack (/rad)
C_{Y_β}	Side Force Coefficient due to Sideslip (/rad)
$C_{Y_{\delta A}}$	Side Force Coefficient due to Aileron Deflection (/rad)
$C_{Y_{\delta R}}$	Side Force Coefficient due to Rudder Deflection (/rad)
D	Drag (lb_f)
E	Translational Position along Inertial E-axis (ft)
$Elev$	Elevator Deflection (rad)
E_S	Specific Energy Height (ft)

List of Symbols (cont.)

Symbol	Definition
Fx	Sum of forces in body fixed x-axis direction (lb$_f$)
Fy	Sum of forces in body fixed y-axis direction (lb$_f$)
Fz	Sum of forces in body fixed z-axis direction (lb$_f$)
g	Acceleration due to Gravity(ft/s^2)
$H(i)$	Hamiltonian
h	Inertial Altitude (ft)
I_X	Moment of Inertia about Body Fixed x-axis (slug-ft^2)
I_y	Moment of Inertia about Body Fixed y-axis (slug-ft^2)
I_z	Moment of Inertia about Body Fixed z-axis (slug-ft^2)
J	Augmented Objective Function
K_{CL}	C_L Control Input Aggressiveness Variable Parameter
$K\varphi$	φ Control Input Aggressiveness Variable Parameter
L	Lift (lb$_f$)
$\overline{L}$	Roll Moment about Body Fixed x-axis (ft-lb$_f$)
M	Pitch Moment about Body Fixed y-axis (ft-lb$_f$)
m	Mass (lb$_m$)
N	Translational Position along Inertial N-axis (ft)
$\overline{N}$	Yaw Moment about Body Fixed z-axis (ft-lb$_f$)
OAT	Outside Air Temperature (°R)
P	Role Rate about Body Fixed x-axis (rad/s or deg/s)
$P_{static\ CORRECTED}$	Corrected Static Pressure (lbs/ft^2)

List of Symbols (cont.)

Symbol	Definition
$P_{static\ INDICATED}$	Indicated Static Pressure (lbs/ft^2)
P_s	Specific Excess Power (ft/s)
Q	Pitch Rate about Body Fixed y-axis (rad/s or deg/s)
$q_{CORRECTED}$	Corrected Dynamic Pressure (lbs/ft^2)
$q_{INDICATED}$	Indicated Dynamic Pressure (lbs/ft^2)
R	Yaw Rate about Body Fixed z-axis (rad/s or deg/s)
Rdr	Rudder Deflection (rad or deg)
R_{GAS}	Atmospheric Gas Constant (1716 ft lbf / (slug °R))
$S(i)$	Sailplane State Vector
s	Wing Area (ft^2)
$U(i)$	Sailplane Control Vector
u	Body Fixed x-axis Velocity (ft/s)
u_{wind}	Body Fixed x-axis Wind Velocity (ft/s)
V_i	Indicated airspeed (ft/s)
V_t	True Airspeed (ft/s)
v	Body Fixed y-axis Velocity (ft/s)
v_{wind}	Body Fixed y-axis Wind Velocity (ft/s)
w	Body Fixed z-axis Velocity (ft/s)
w_{wind}	Body Fixed z-axis Wind Velocity (ft/s)
$Wind_E$	Inertial Fixed Winds in East Direction (ft/s)
$Wind_h$	Inertial Fixed Winds in Up Direction (ft/s)

List of Symbols (cont.)

Symbol	Definition
$Wind_N$	Inertial Fixed Winds in North Direction (ft/s)
α	Angle of Attack (deg)
β	Side-slip Angle (deg)
$\chi(N)$	Optimization Terminal State Constraints
ϕ	Euler Roll Angle (deg)
ψ	Euler Yaw Angle (deg)
γ	Flight Path Angle/Flight Path Angle in Steady Flight (deg)
λ	Lagrange Multiplier Vector
$\mu(N)$	Optimization terminal Cost Function
ν	Lagrange Multiplier Vector
θ	Euler Pitch Angle (deg)
ρ	Air Density (slugs /ft^3)
ρ_{SL}	Air Density at Sea Level (0.002377 slugs/ft^3)

List of Acronyms

Abbreviation	Definition
AFB	Air Force Base
AFIT	Air Force Institute of Technology
AFRL	Air Force Research Laboratory
AGL	Above Ground Level
DAS	Data Acquisition System
DOE	Design Of Experiments
DFRC	Dryden Flight Research Center
DS FTT	Dynamic Soaring Flight Test Technique
FTE	Flight Test Engineer
FTN	Flight Test Navigator
GPS	Global Positioning System
GUI	Graphical User Interface
HOS	Hands On Stick
IMU	Inertial Measurement Unit
INS	Inertial Navigation System
KIAS	Knots Indicated Air Speed
LAMARS	Large Amplitude Multi-Mode Aerospace Research Simulator
MSL	Mean Sea Level
NASA	National Aeronautics and Space Administration
PC	Personal Computer

List of Acronyms (cont.)

Abbreviation	Definition
RTD	Resistive Temperature Detector
ShWOOPIN	Shear Wind Observed Optimized Investigation for NASA
SODAR	Sonic Detection and Ranging
TACAN	Tactical Air Navigation
TMP	Test Management Project
TPS	Test Pilot School
USAF	United States Air Force
VACD	Aerospace Vehicles Technology Assessment and Simulation Branch
VHF	Very High Frequency

OPTIMAL DYNAMIC SOARING FOR FULL SIZE SAILPLANES

I. Introduction

Motivation

Dynamic soaring is a unique flying technique designed to allow air vehicles to extract energy from horizontal wind shears. Dynamic soaring has been used by seabirds like the Albatross to fly hundreds of kilometers a day across the ocean. Small hobby radio controlled gliders have also used dynamic soaring to achieve sustained speeds of over 200 miles per hour from just a simple hand toss. Dynamic soaring, however, has never before been studied for use on full size aircraft. The significance of this gap in dynamic soaring research has impact on future of space exploration and the sport of soaring.

Unlike the current generation of land roving robotic explorers, the National Aeronautics and Space Administration (NASA) is developing a new series of relatively large sailplane-like aircraft that will deploy from deep space planetary probes during atmospheric entry. To reduce on board power requirements, these airborne robotic explorers will rely on soaring techniques already commonly used on manned sailplanes in order to enhance their endurance and range. By extracting energy from the atmosphere in this manner, these vehicles would be able to devote more of their limited payload to science and engineering as opposed to propulsion. Hence, the primary goal of this research was to prove or disprove the viability of dynamic soaring for enhancing a full size aircraft's total energy by using a manned sailplane as a demonstration air vehicle. Additionally, this research was dedicated to increasing the knowledge base of dynamic soaring as a new technique for the sport of soaring.

Background

By using naturally occurring phenomenon of the Earth's atmosphere, soaring pilots are able to fly distances and achieve altitudes that rival or even exceed the capabilities of many powered aircraft. Modern sailplane feature sleek, low weight, high lift to drag airframes that are designed to give them enhanced aerodynamic performance and efficiency. To understand the significance of dynamic soaring as a flight technique for full size sailplanes, it is important to understand the origins of soaring and the techniques currently employed by sailplane pilots to enhance the sailplane's total energy state.

Inventor Leonardo Da Vinci, shown in Figure 1, is credited with designing the world's first glider (Leonardo Website). Da Vinci, inspired by studying the wing designs of local birds and bats, created a harness attached to a bat wing like flying machine that was appropriately scaled to accommodate a human pilot (Short, 2004:2).

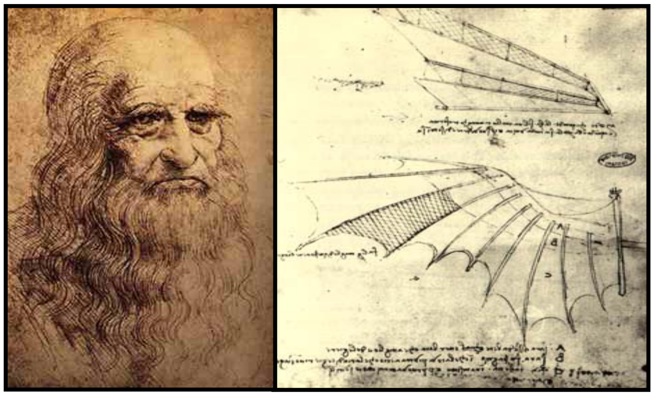

Figure 1. Leonardo Da Vinci and the Bat Wing Flying Machine

Unfortunately, as revolutionary as his design was, the bat wing never flew and languished in obscurity for several hundred years until a new study was initialed by Sir George Cayley in the early 1800's (Short, 2004:2). Cayley, shown in Figure 2, was inspired by Da Vinci's glider design and built several gliders to further investigate the possibility of manned flight (Circling Hawk Paragliding Website). Cayley was the first to quantify the primary forces of flight and proved that manned gliding flight was possible through several very short duration demonstration flights. His research ultimately laid the foundation for Otto Lilienthal first glider flights during the late 1800's (Short, 2004:2).

Figure 2. Sir George Cayley and Early Glider Design

Regarded as the world's first glider pilot, Lilienthal, shown in Figure 3, designed, built, and flew his full sized gliders based on the earlier research conducted by Cayley and Da Vinci (Invention Psychology Website). His flights were performed from a symmetric hill he constructed that allowed for brief gliding flights into a headwind based on the prevailing winds. Fittingly, Lilienthal's glider design bore a good resemblance to Leonardo Da Vinci's bat wing like design of the Renaissance. Sadly, Lilienthal suffered a severe crash during one of his glider flights and died two days later from his injuries (Short, 2004:2). His famous last words were, "Sacrifices must be made."

Figure 3. Otto Lilenthal and his Glider

To his credit, Lilienthal's life work and sacrifice provided much of the foundation for the Wright Brothers initial aeronautical research and glider designs. The Wright Brothers, shown in Figure 4, used Lilenthal's designs to help ensure their ultimate success in powered flight at Kitty Hawk in December of 1903 (Library of Congress Website).

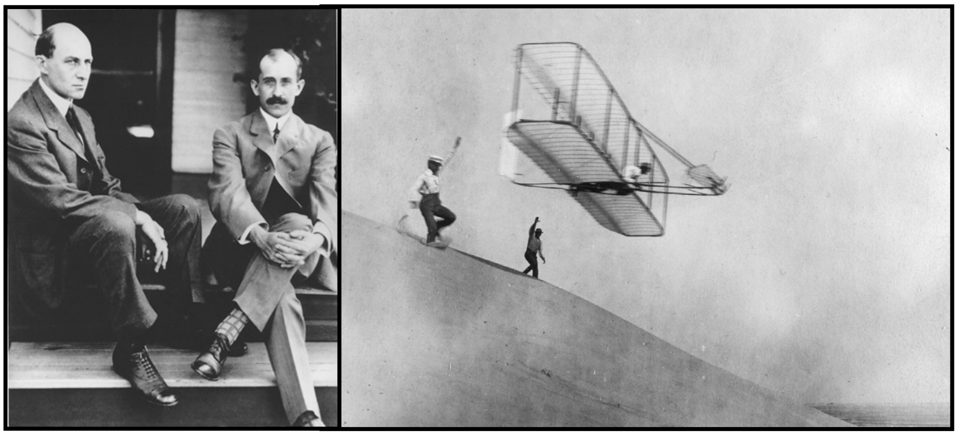

Figure 4. Wright Brothers and Early Glider Tests at Kitty Hawk North Carolina

With the birth of powered aviation, gliders became viewed as anachronistic in an age where aircraft were being pushed to achieve faster speeds, longer ranges, greater payloads, and longer endurance. The need for combat aircraft at the start of World War I only accelerated this drive. Ironically, the end of World War I unknowingly gave a second birth to the sport of soaring through the Treaty of Versailles (Short, 2004:2).

This treaty imposed heavy training and technology restrictions on the defeated German Air Force in order to destroy the threat that Germany posed. These restrictions were primarily aimed at powered aviation, but made no limitations on un-powered flight (Short, 2004:2). These restrictions were ultimately ignored by Adolf Hitler in the late 1930's, but not before many government sponsored and private gliding clubs sprang up across Germany. An example of one of these clubs is shown in Figure 5 (Vintage Sailplanes Website). These clubs ultimately served as initial pilot training for the first cadre of the Third Reich's Luftwaffe.

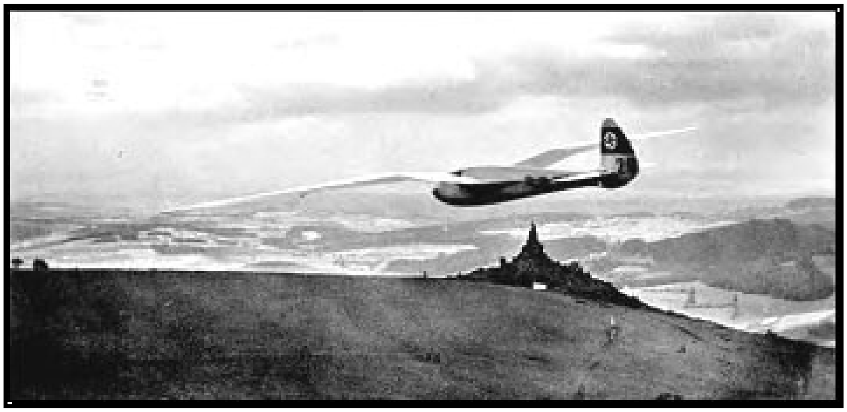

Figure 5. German Gliding Club DFS Reiher II Sailplane

The legacy of Germany's heavy involvement during the second dawn of the sport of soaring can still be seen today in two primary ways. First, the majority of current sailplane designers and manufactures are based in Germany or countries occupied by Germany during World War II. Secondly, the flying methods pioneered by these German gliding clubs still dominate the sport of soaring today in the form of three major static soaring techniques (Short, 2004:3-4).

Traditional Soaring Techniques

Successful soaring has primarily relied on mastering three techniques that exploit atmospheric conditions in order to enhance sailplane endurance. These techniques are thermaling, ridge soaring, and wave soaring. Collectively they are known as static soaring techniques and all involve using a vertical velocity component of moving air.

Thermaling, shown in Figure 6, is the most common and popular of these techniques (Civil Air Patrol National Technology Center Website). This technique can be used on sun lit days where the heated surface of the Earth radiates heat back to the atmosphere at non-uniform rates. For instance, dark ploughed fields, exposed rock outcroppings, and asphalt all radiate heat back to the atmosphere faster than other areas of the Earth's surface. Air above these surfaces heats up, becomes less dense, and hence rises faster than the cooler air surrounding it. This creates small regions of the atmosphere with rising columns of air. Soaring pilots can use these rising columns of air to offset the natural sink rate of the sailplane. If the thermal is strong enough, pilots can gain altitude by flying tight circles or weaving across the rising pockets of air.

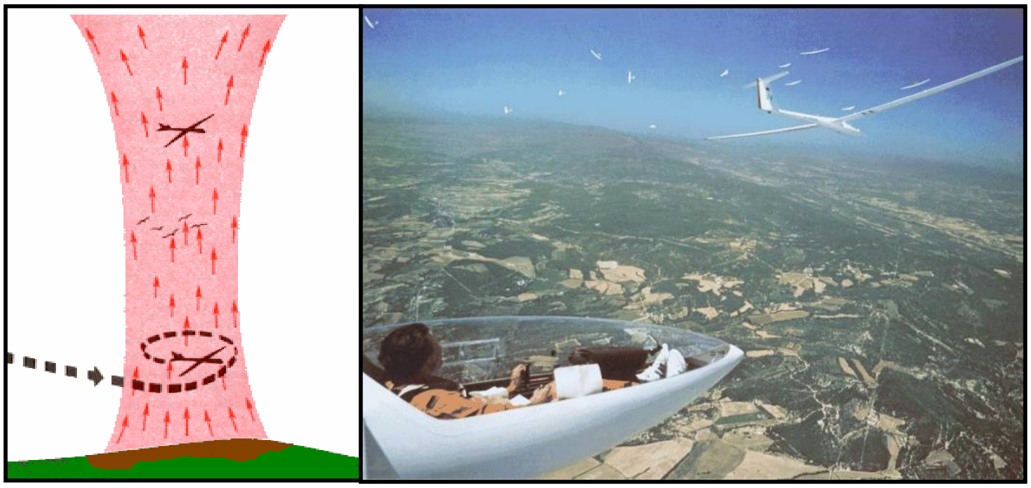

Figure 6. Thermal Soaring

Ridge soaring, shown in Figure 7, is a form of orthographic lift in the sense that it takes advantage of wind that flows up and over ridge lines much like water flows around a rock placed in a stream (Civil Air Patrol National Technology Center Website). Soaring pilots can exploit the upwards moving air on the windward side of a ridge by flying parallel to the ridge line. Ridge soaring, however, is only possible over localized areas with steady state winds and generally loses effectiveness at altitudes significantly above the height of the ridge itself.

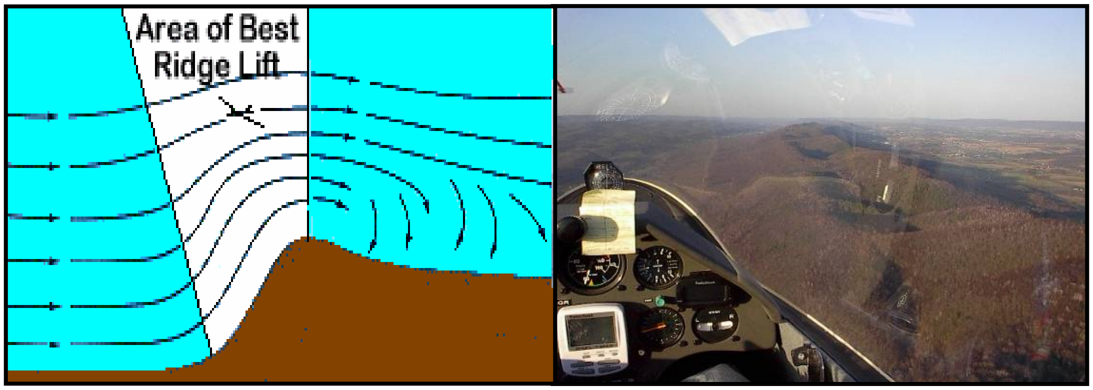

Figure 7. Ridge Soaring

Wave soaring, shown in Figure 8, is also a type of orthographic lift that functions similarly to ridge soaring (Civil Air Patrol National Technology Center Website). However, this form typically involves extremely strong, broad currents of air associated with massive weather fronts flowing over large mountain ranges. Unlike ridge soaring, these currents of moving air can flow into the upper reaches of the stratosphere. Wave soaring conditions were responsible for the current world soaring altitude record of 50,699 feet set by Steve Fossett on 31 August 2006 (Experimental Aircraft Association Website).

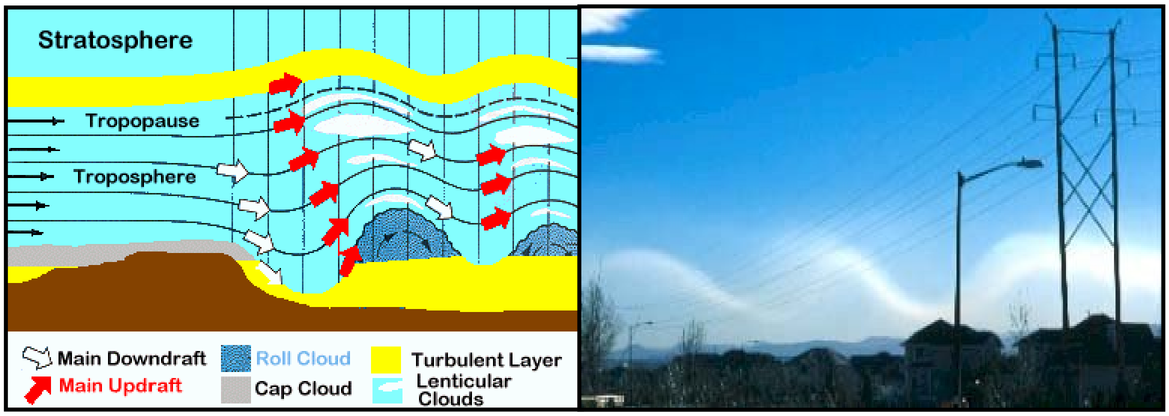

Figure 8. Wave Soaring

These static soaring techniques are popular since they are thoroughly documented, are normally of sufficient strength to be of use to full sized aircraft, and because their existence in the atmosphere can usually be physically seen. For instance, cumulous clouds indicate the position of thermals, and standing lenticular clouds mark wave soaring conditions. Dynamic soaring, however, is fundamentally different than any of these static soaring techniques.

Dynamic Soaring

Unlike static soaring, which relies on a rising vertical component of velocity to the wind, dynamic soaring involves extracting energy from strictly horizontal wind shears. This theory was first proposed by Physics Nobel Laureate Lord Rayleigh, show in Figure 9 (Physics and Advanced Technologies Website).

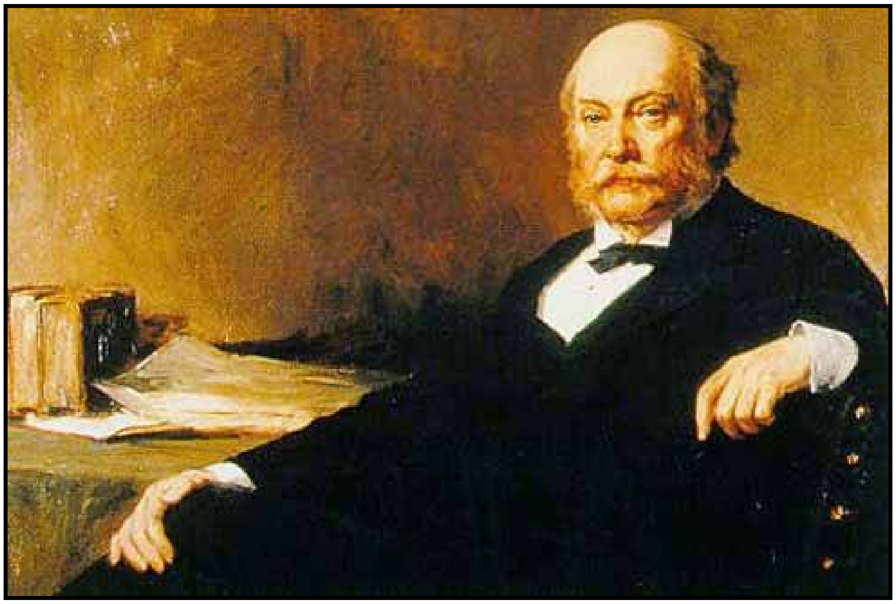

Figure 9. Lord Rayleigh

Much like Da Vinci, Lord Rayleigh observed birds in flight and noticed that, without flapping their wings to generate thrust, birds were sometimes able to traverse great distances seemingly without the presence of traditional forms of lift.

Puzzled by this phenomenon, he proposed:

> …a bird without working his wings cannot, either in still air or in a uniform horizontal wind, maintain his level indefinitely. For a short time such maintenance is possible at the expense of an initial velocity, but this must soon be exhausted. Whenever therefore a bird pursues his course for some time without working his wings, we must conclude either
> (1) that the course is not horizontal
> (2) that the wind is not horizontal
> (3) that the wind is not uniform
> It is probable that the truth is represented by (1) or (2); but the question I wish to raise is whether the cause suggested by (3) may not sometimes come into operation. (Lord, 1883:354-355)

Through this statement, Lord Rayleigh was the first to propose the idea that birds could extract energy from the atmosphere by flying between regions of air moving at different horizontal velocities. To understand this phenomenon further, a brief explanation is given below. Additional details regarding extracting energy from wind are given in (Lissaman, 2005:2-3).

A sailplane, unlike powered aircraft, is affected by only three of the forces of flight, namely lift, drag, and weight. Lift is defined as operating perpendicular to the relative wind, drag is defined as operating parallel to the relative wind, and weight points to the center of Earth regardless of aircraft's orientation. A vehicle's energy state can only be affected by forces acting parallel to its motion (Meriam, 1986: 147) in the inertial reference frame, so a sailplane's energy state is only affected by forces acting parallel to its flight path. Furthermore, gravitational forces perform conservative work and, hence, have no effect on the total energy. Therefore, in calm air, when the lift acts perpendicular to the flight path, drag is the only force that can change a sailplane's energy state and it dissipates it. This is shown in Figure 10. However, as explained in more detail below, when flying in winds it is possible for a sailplane's relative wind to be in a direction that is not parallel to its flight path, which makes it possible for the lift force to affect the energy state of the sailplane. In this case, whether the lift increases or decreases the energy state depends on the flight path relative to the wind. Exploiting this effect to increase the energy state of the sailplane is the goal of dynamic soaring.

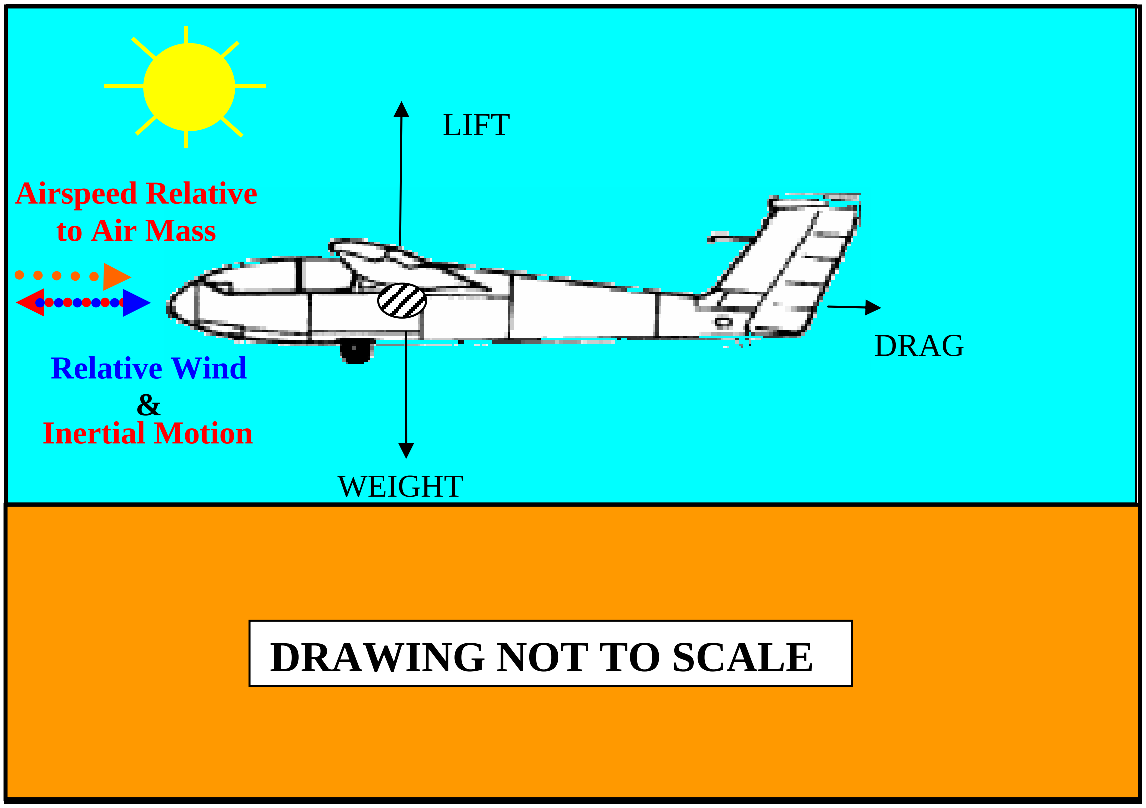

Figure 10. Sailplane in Horizontal Flight in no Wind Shear

When flying in winds, the lift force can act to affect the energy state of a sailplane. In climbing and descending flight in horizontal wind shears, a new effective angle of attack of the wing can develop. This new angle of attack is the result of a vector sum between the inertial based winds the aircraft is flying through, and the inertial velocity of the aircraft. This effect can serve to rotate the lift vector of the aircraft forward such that a component of the lift force will act parallel to the aircraft's motion. In essence, this component of lift acts like a thrust force.

This component of lift can offset the energy loss due to drag. If this effect is strong enough, the sailplane can even fly energy neutral or energy gaining profiles. This is what Lord Rayleigh described while observing birds in flight and is the essence of what has come to be known as dynamic soaring. This concept is illustrated in Figure 11 for climbing flight.

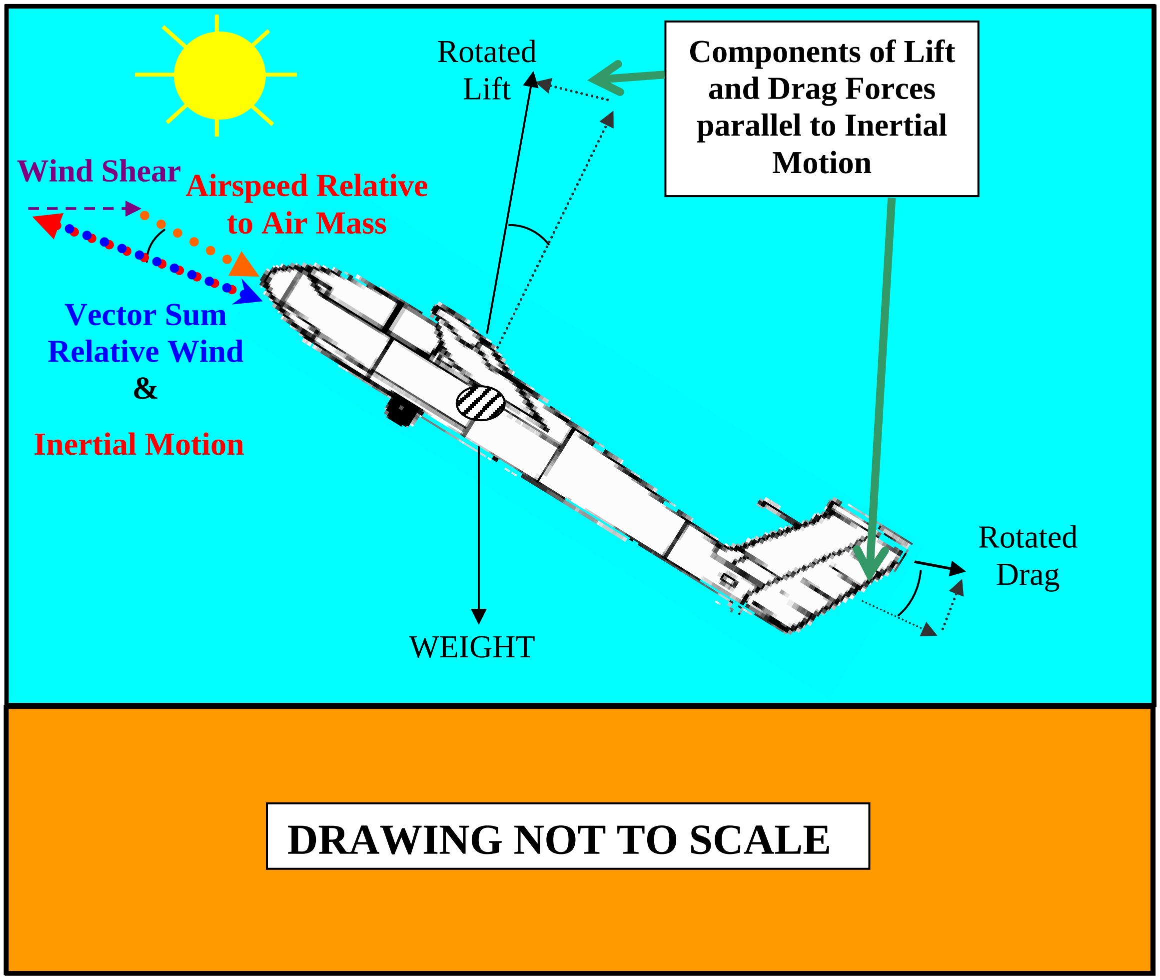

Figure 11. Sailplane in Climbing Flight in Wind Shear

In this example, the sailplane is pulled higher in altitude by this lift vector thrust effect. The opposite is true in a descent with a tailwind shear, where the sailplane is propelled faster by the thrust effect of the rotated lift vector. This is shown in Figure 12.

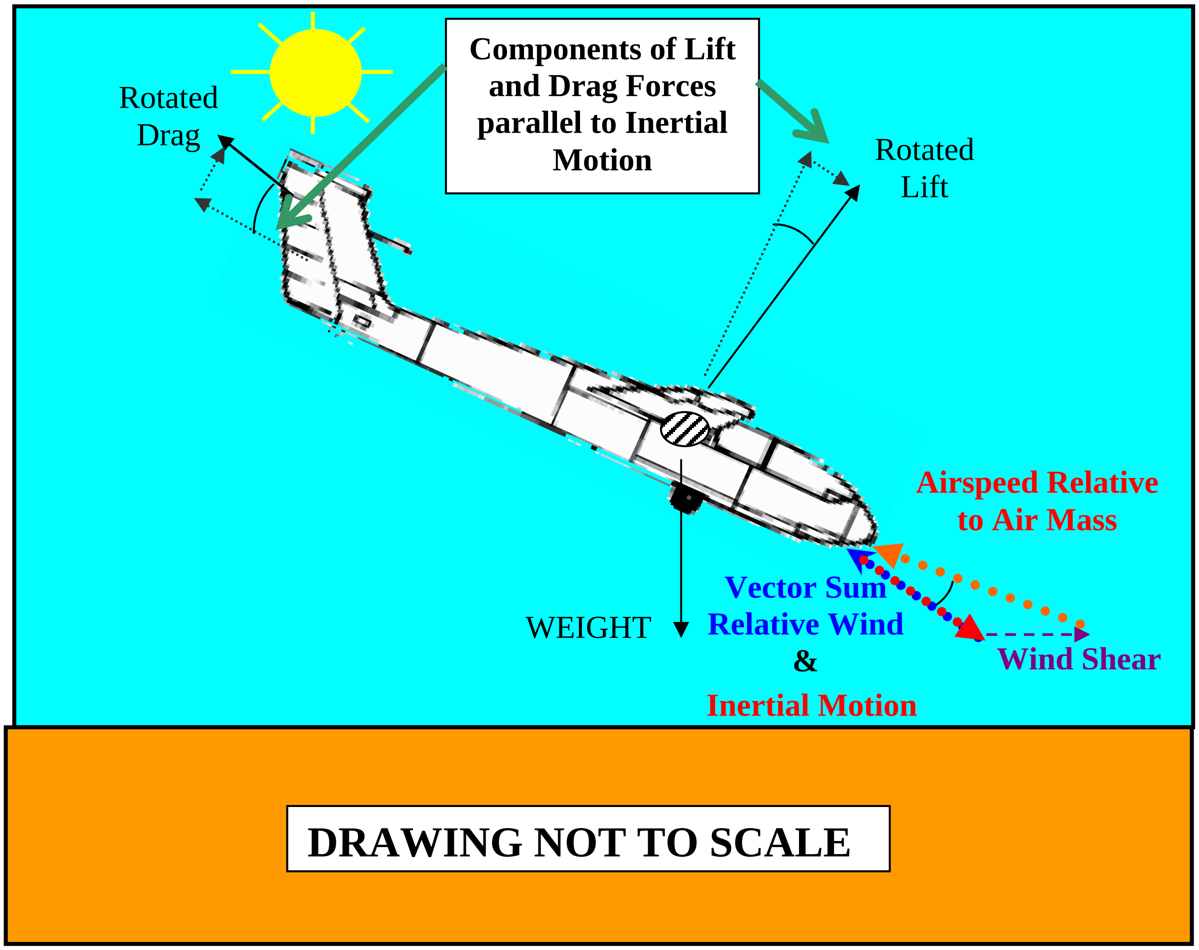

Figure 12. Sailplane in Climbing Flight in Wind Shear

Hence, the sailplane can gain both potential and kinetic energy from the wind. A wind shear is required in order to create a continuously changing wind gust effect on the sailplane as it transits shear layers. This wind gust effect continuously changes the sailplane's airspeed with respect to the airmass it is traveling through. For instance, if a sailplane were to suddenly encounter a 10 knot headwind gust, its effective airspeed with respect to the air mass would momentarily increase by 10 knots along with a momentary increase in both lift and drag. However, its ground speed for that moment in time would be nearly identical to what it was before the gust since the wind gust would primarily flow around and past the airframe as opposed to impeding its forward motion instantly. As the sailplane transits forward through the wind shear, this changing wind gust effect allows the aircraft to carry this increase in effective airspeed and corresponding lift forward to the next moving air mass reference frame where the process is repeated. The component of lift acting as a thrust resulting from the wind shear effect enables the sailplane to climb higher to achieve greater potential energy, or descend faster to increase kinetic energy. This effect is similar to the increase in inertial velocity, with respect to a non-moving observer, a roller skater would experience immediately upon "transiting a shear boundary" by entering or exiting a moving sidewalk from a stationary sidewalk. If the sailplane were to encounter no wind shear conditions (i.e. steady state or calm winds), this continuously changing gust effect and associated forward rotation of the lift vector would be eliminated and dynamic soaring would cease.

Dynamic soaring is enhanced the steeper the gradient of the wind shear. Hence, the perfect dynamic soaring environments occur when regions of calm or slower air are separated from regions of faster moving air by infinitesimally small shear boundaries. In reality, however, such an environment does not exist. Fortunately, wind shears caused by boundary layers or physical obstructions occur frequently in nature and can be sufficient to create a dynamic soaring environment.

Problem Statement

Early attempts at dynamic soaring were performed by German gliding clubs, but were ultimately unsuccessful and abandoned. However, in his book (Reichmann, 1978) titled, Streckensegelflug (*distance soaring flight*), Helmut Reichmann relates the legend of a soaring pilot named Ingo Renner, shown in Figure 13 (Fiddlers Green Website). While flying a Libelle sailplane over Tocumwal Australia on 24 October 1974, Ingo Renner encountered a sudden 40 knot wind shear caused by a strong temperature inversion. Using this wind shear, Mr. Renner was allegedly able to maintain his altitude for over 20 minutes without the presence of any traditional lift sources.

Figure 13. Ingo Renner and Libelle Sailplane

In light of this account, modern computer analytical techniques, advanced sailplane designs, and a desire by NASA to study energy enhancing techniques for its next generation of planetary explorers, a new in depth study of dynamic soaring in full size sailplanes is warranted.

Supporting Research and Dynamic Soaring Research Objective

Initial ground work for the research presented in this thesis began at the USAF TPS during the spring of 2004. A fully instrumented LET L-23 Super Blanik sailplane, shown in Figure 14, was flown using aerodynamic modeling test profiles in order to fully characterize the aircraft's lift and drag characteristics (drag polar, speed polar, etc).

Figure 14. Test Aircraft L-23 Super Blanik

The ultimate goal of this project, known as SENIOR IDS (Borror, 2004), was to lay the research basis for a full dynamic soaring study. Although the SENIOR IDS test team attempted a best guess at a dynamic soaring maneuver as the culmination of their project, their chief recommendation was given as:

> No good models or prediction tools were available to the test team, and insufficient time was available to construct such models. Optimization of the dynamic soaring maneuver is likely not possible without being able to run large numbers of trials on a representative simulation. As there was no model or comprehensive theoretical understanding of dynamic soaring, there was no prediction of energy loss and therefore there was no comparison of test results against the predicted results. Develop and use a model to optimize the dynamic soaring maneuver. (Borror, 2004:15)

Additional L-23 Super Blank aerodynamic data was collected by the HAVE BLADDER (Aviv, 2005) test team at the United States Air Force Test Pilot School (USAF TPS) during the fall of 2005. The primary goal of this project was to quantify the L-23 aerodynamic stability derivatives and the moments of inertia (Aviv, 2005:2). This data was specifically collected in direct support of dynamic soaring modeling and simulation efforts required for this research.

With this foundation of data, the primary objective of this research was to continue the work begun by the SENIOR IDS and HAVE BLADDER test teams on the L-23 Super Blanik by developing, flying, analyzing, and evaluating the viability of optimal dynamic soaring maneuvers for full size sailplanes.

Assumptions

For sake of mathematical analysis, a non-rotating, flat earth was assumed since a dynamic soaring trajectory typically occurs over a very brief period of time and over a small localized area of the Earth's surface. Hence, only the Body Fixed and North-East-Down coordinate systems were used. It was also assumed that the wind shear was steady, operated uniformly from the inertial west direction (cross-range), and featured no vertical component to its velocity. All aircraft equations developed for this research assumed a rigid body, constant mass aircraft.

General Approach

The development of an optimal dynamic soaring trajectory was of primary importance since its creation was required before any other phase of the project could begin. This was accomplished by first deriving the appropriate aircraft point mass equations of motion for the L-

23 Super Blanik from the full set of non-linear 6-DOF equations of motion. These equations were then modified to include the effects of a steady state wind shear. Control inputs for these equations were identified as the aircraft's commanded coefficient of lift, C_L, and the aircraft's commanded bank angle, ϕ. The optimization objective function was formulated so as to maximize the final energy state of the L-23 Super Blanik at the conclusion of the dynamic soaring maneuver subject to several spatial and aerodynamic constraints. A nominal initial guess trajectory was developed that approximated the dynamic soaring flight of an Albatross seabird by assuming that C_L and ϕ inputs were sinusoidal throughout the flight. The resultant state equations, controls, constraints, objective function, and initial guess trajectory were then incorporated into a MATLAB® dynamic optimization routine in order to produce converged optimal dynamic soaring trajectories.

The dynamic soaring aircraft equations of motion developed for this research were then programmed into a prototype sailplane simulator developed at the Large Amplitude Multi-Mode Aerospace Research Simulator (LAMARS). This facility is located at the Aerospace Vehicles Technology Assessment and Simulation Branch (VACD) of the Air Force Research Laboratory (AFRL) in Wright Patterson AFB Ohio. This simulator was used to validate these dynamic soaring aircraft equations of motion and to obtain simulator experience to be incorporated into a final dynamic soaring research simulator developed at the NASA DFRC. This NASA L-23 Super Blanik sailplane flight simulator was used to develop advanced dynamic soaring cockpit displays, develop appropriate flight test techniques, and to practice aircrew coordination. Dynamic soaring maneuvers, known as hairpins due to their trajectory shape as viewed from above, were then flown in the simulation in horizontal wind shear conditions representative of Edwards AFB. These wind shears were modeled based on ten years worth of historical wind shear data above the Rogers dry lakebed. In order to further demonstrate the energy benefit of a properly executed hairpin maneuver, a mirror image of the optimal dynamic soaring trajectory was developed. Known as the anti-dynamic soaring maneuver, or anti-hairpin, this profile was designed to illustrate the energy loss realized when flying the sailplane contrary to dynamic soaring theory. The hairpin and the anti-hairpin maneuvers were developed to provide a large enough spread in the final energy data results so that a sufficient statistical analysis could be performed and conclusions could be made more obvious. Multiple flight simulator runs were conducted as a risk mitigation strategy to help ensure the success of the actual flight test and to evaluate the optimal trajectories obtained through mathematical analysis.

Finally, a fully instrumented L-23 Super Blanik sailplane was flown in real world wind shear conditions in both the hairpin and anti-hairpin maneuvers in order to gather flight test data. Results from the flight test were compared against mathematical analysis, and simulation predictions.

Overview of Thesis

Chapter I of this thesis began with a brief overview of the motivation behind this research, the history of the sport of soaring, and an explanation of traditional static soaring techniques that have been in use by sailplane pilots for almost 80 years. This built the foundation for the next section of Chapter 1 which explained the theory of dynamic soaring and allowed for the development of the thesis problem statement. Chapter II explains how this problem statement is then formulated into non-linear point mass aircraft equations of motion based on the modeled aerodynamic performance characteristics of a specially modified L-23 Super Blanik owned by the USAF TPS. The resulting dynamic soaring point mass equations of motion are then transformed into discrete equations designed for use with trajectory dynamic optimization. Chapter III explains how the results of this optimization analysis and L-23 Super Blanik stability derivatives and moment of inertia data are used to develop a prototype sailplane simulator at the VACD LAMARS facility of the AFRL. This simulator is used as a build up to a full 6-DOF L-23 dynamic soaring flight simulator developed at the NASA DFRC. In Chapter IV, the results of sailplane flight test in an instrumented L-23 Super Blanik are described. This flight test program was performed at Edwards Air Force Base (AFB) in real world wind shear conditions in order to collect dynamic soaring data. The thesis then concludes with Chapter V, which provides overall dynamic soaring conclusions and recommendations based on the sum total of dynamic optimization, flight simulator data, and flight test results.

II. Development of Optimal Dynamic Soaring Trajectory

Point Mass Equations

In order to develop the optimal dynamic soaring trajectory, the L-23 Super Blanik was first reduced to a point mass model. This technique was chosen due to its success in previous trajectory optimization research projects, such as developing the minimum time to climb trajectories for the F-4 Phantom and energy maneuverability profiles for the F-15 *Streak Eagle* flights of the 1970's (Bryson, 1999:172). Hence, a point mass model was considered sufficient to yield an optimal dynamic soaring flight profile for a sailplane. In order for this method to be successful, however, accurate data about the aircraft's weight and performance characteristics were first required. This information is shown in Figure 15 (LET,1993:1-5 - 2-3).

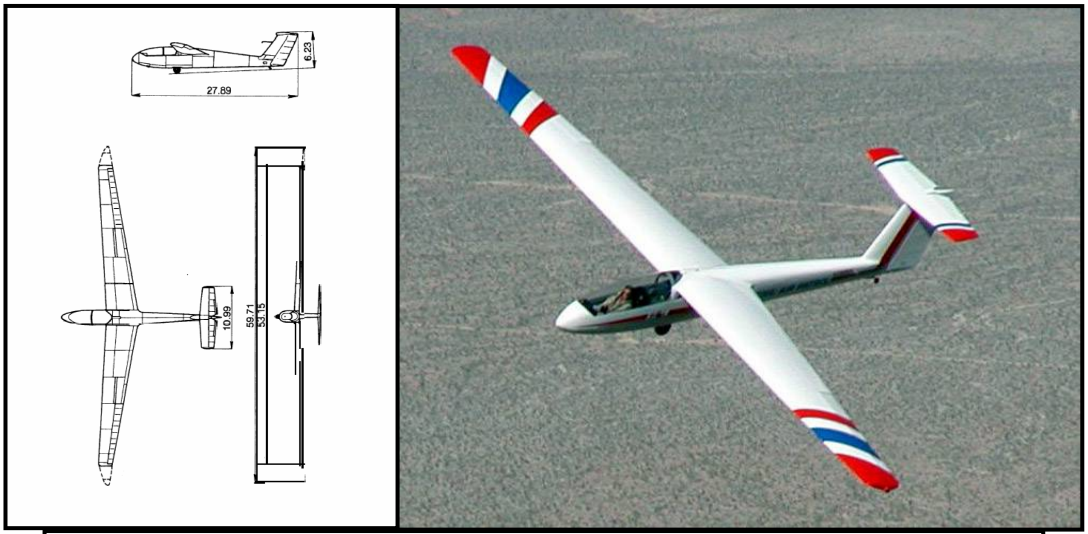

weight = 1124 lbs
V_{Stall} = 60 ft/s
Wing Area (S) =215.27ft^2
$V_{manuvering}$=132 ftft/s/ft
V_{max} = 206.7 ft/s
C_{Lmax} = 1.239

Figure 15. L-23 Super Blanik Data

Neglecting the aircrafts rotational dynamics and treating it as a point mass with no thrust, the twelve nonlinear equations of motion (EOMs) used to represent 6-DOF aircraft motion (Honeywell, 1996:65-66) reduce to the following six nonlinear differential equations.

$$\dot{V}_t = \frac{1}{m}\left[-D - mg\sin(\gamma)\right]$$

$$\dot{\psi} = \frac{1}{mV_t\cos(\gamma)}\left[L\sin(\phi)\right]$$

$$\dot{\gamma} = \frac{1}{mV_t}\left[L\cos(\phi) - mg\cos(\gamma)\right]$$

$$\dot{h} = V_t\sin(\gamma)$$

$$\dot{E} = V_t\cos(\gamma)\sin(\psi)$$

$$\dot{N} = V_t\cos(\gamma)\cos(\psi)$$

Where:

V_t = True airspeed (ft/s)
ψ = Heading Angle (deg)
γ = Flight Path Angle (deg)
h = Inertial Altitude (ft)
N = Inertial Downrange Distance (ft)
E = Inertial Cross range Distance (ft)

ϕ =Roll Angle (deg)
m = Mass (lb_m)
g = Gravitational Acceleration (ft/s^2)
D = drag (lb_f)
L = lift (lb_f)

In order to use these point mass equations to optimize dynamic soaring trajectories in horizontal wind gradients, the effects of the horizontal winds were added to the EOMs above (Jackson, 1999:220) to obtain the point mass equations of motion used by Professor Yiyuan Zhao of the University of Minnesota in an earlier dynamic soaring study (Zhao, 2004:70-71). The following assumptions were made about the winds:

1. Winds operate only in the direction of the inertial *E*-axis (cross-range). Hence, winds in the inertial *N*-axis direction (down-range) were zero.
2. Thermal, ridge, and wave soaring conditions were non existent. Hence, there were no vertical winds.

These assumptions resulted in the following equations of motion.

$$\dot{V}_t = \frac{1}{m}\left[-D - mg\sin(\gamma) - m\dot{Wind}_E\cos(\gamma)\sin(\psi)\right] \tag{1}$$

$$\dot{\psi} = \frac{1}{mV_t\cos(\gamma)}\left[L\sin(\phi) - m\dot{Wind}_E\cos(\psi)\right] \tag{2}$$

$$\dot{\gamma} = \frac{1}{mV_t}\left[L\cos(\phi) - mg\cos(\gamma) + m\dot{Wind}_E\sin(\gamma)\sin(\psi)\right] \tag{3}$$

$$\dot{h} = V_t\sin(\gamma) \tag{4}$$

$$\dot{E} = V_t\cos(\gamma)\sin(\psi) + Wind_E \tag{5}$$

$$\dot{N} = V_t\cos(\gamma)\cos(\psi) \tag{6}$$

Where:

$Wind_E$ = Wind in the east (cross-range) direction

Lift and drag were determined by equations (7) and (8) respectively.

$$L = \tfrac{1}{2}\rho V_t^2 s C_L \tag{7}$$

$$D = \tfrac{1}{2}\rho V_t^2 s C_D \tag{8}$$

Where:

ρ = Atmospheric Density (lbm/ft^3)

s = Wing Area (ft^2)

C_L = Coefficient of lift

C_D = Coefficient of drag

The use of equations (7) and (8) required accurate models for the L-23 sailplane's C_L and C_D in order to be precise. These were provided by the USAF TPS SENIOR IDS project accomplished in 2004 (Borror, 2004). Derived using aerodynamic modeling flight test techniques, the lift curve slope and drag polar for the test aircraft L-23 Super Blanik were determined as shown in equations (9) and (10).

$$C_L = -0.0029*\alpha^2 + 0.0917*\alpha + 0.6041 \tag{9}$$

$$\left.\begin{array}{ll}\text{When } C_L \leq 1.0: & C_D = 0.027*C_L^2 + 0.017 \\ \text{When } C_L > 1.0 & C_D = (C_L - 0.7)/7.2\end{array}\right\} \qquad (10)$$

Where:

α = Angle of Attack (deg)

Equations (1) through (6) included a unique $Wind_E$ term that was is not normally featured in standard point mass aircraft equations of motion. This $Wind_E$ term described the strength of the horizontal wind at a given altitude (i.e. it described the wind shear). This term was significant to this research and merits further explanation.

The development of the $Wind_E$ term first required a valid wind model representative of typical wind conditions at Edwards AFB during the proposed research flight test window (March through May of 2006). This wind model was developed by analyzing the previous ten years worth of Edwards AFB wind data as complied by the NASA DFRC weather observatory. A typical wind observation across the proposed dynamic soaring altitude band over the Rogers dry lakebed at Edwards AFB is shown in Figure 16.

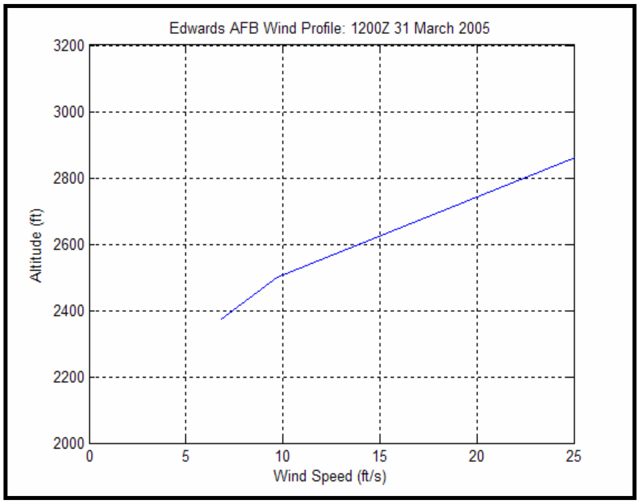

Figure 16. Winds at Edwards AFB

The NASA DFRC weather observatory regularly measured wind conditions at Edwards AFB through the use of instrumented weather balloons launched from the field elevation of 2378 ft above Mean Sea Level (MSL) and Sound Detection And Ranging equipment (SODAR). Based on these observations, winds across the Rogers dry lakebed generally blew from the West on a heading of 090°. Wind strengths varied linearly with altitude with the slowest velocities at the surface due to boundary layer and/or temperature inversion effects. Accordingly, the $Wind_E$ terms shown in equations (11) and (12) were developed as a linear approximation of actual wind shear conditions across the Rogers dry lake bed at Edwards AFB.

$$Wind_E = WIND_{SLOPE}\, h \tag{11}$$

Taking the derivative of equation (11) with respect to time and using equation (4) gives,

$$\dot{Wind}_E = \frac{\partial Wind_E}{\partial h}\frac{dh}{dt} = WIND_{SLOPE}\,\dot{h} = WIND_{SLOPE}\, V_t \sin(\gamma) \tag{12}$$

Where:

$Wind_{SLOPE}$ = Change in the wind velocity per foot of altitude gain (ft/s / ft)

An understanding of the current energy state of the sailplane was also critical to the success of this project. Insight into this aspect of the research was obtained by beginning with the classic definition for energy shown in equation (13).

$$E = \frac{mV_t^2}{2} + hmg \tag{13}$$

Dividing this classical total energy equation by weight yielded the specific energy equation, or $E_{S,}$ of the sailplane as shown in equation (14).

$$E_S = \frac{V_t^2}{2g} + h \tag{14}$$

The equation for specific excess power, or P_s, as shown in equation (15), is found by taking the derivative of equation (14) with respect to time.

$$P_S = \frac{dE_s}{dt} = \frac{V_t \dot{V}_t}{g} + \dot{h} \tag{15}$$

By substituting in equation (1), (4), and (12) as appropriate, the specific excess power equation becomes as shown in equation (16).

$$P_S = -\frac{DV_t}{mg} - \left[\frac{WIND_{SLOPE} \sin(\gamma)\cos(\gamma)\sin(\psi) V_t^2}{g} \right] \tag{16}$$

Equation (16) held the key to understanding dynamic soaring. This equation illustrated the interplay between energy loss due to drag and energy gained from exploiting horizontal wind shears. The first term in equation (16), $-\frac{DV_t}{mg}$, demonstrated that as a sailplane flies through the air, it will always lose energy to drag effects. This loss increases with an increase in airspeed. However, this energy loss due to drag could be offset or even eliminated by the second term in equation (16), $\left[\frac{WIND_{SLOPE}\sin(\gamma)\cos(\gamma)\sin(\psi)V_t^2}{g}\right]$. This term, henceforth referred to as the dynamic soaring term, or (*DST*), was the centerpiece of the mathematical analysis accomplished in this research.

The *DST* was primarily a function of wind shear, defined as $Wind_{SLOPE}$ because of the slope or gradient of the wind shear, the flight path angle, γ, the heading angle, ψ, and the true airspeed V_t. The relationship between these variables dictated the performance of the sailplane in dynamic soaring conditions. For instance, if the sailplane were to fly in a region where there was no wind gradient, then the $Wind_{SLOPE}$ variable would be zero and the energy rate of the sailplane would be governed only by the loss rate due to drag. Of greater significance, however, is the relationship between γ and ψ.

In order to offset energy loss due to drag, the *DST* as a whole must be negative. Under this circumstance, the specific excess power equation becomes a negative drag loss term minus a negative *DST*. From basic algebra, depending on the relative magnitude of the drag loss term to the *DST*, this situation has the possibility to develop an overall positive P_s for the sailplane. A positive P_s results in a positive, or at least a less negative, E_s for the sailplane. This only occurs when either:

1. $0° < \gamma \leq 90°$ while $180° < \psi \leq 360°$

or

2. $-90° < \gamma \leq 0°$ while $0° < \psi \leq 180°$

These two situations mean that when encountering a wind shear (in this case from the West), the sailplane must either climb while facing a headwind or descend while traveling with a tailwind in order to realize an energy benefit. If the sailplane were to fly contrary to this rule, the rate of energy loss would only be greatly exacerbated since losses would occur from both drag and horizontal wind shear effects.

Dynamic Optimization Problem Formulation

The development of an ideal dynamic soaring trajectory required the use of dynamic optimization (Bryson, 1999: Larson, 2005: Zhao, 2004). The first step was to properly pose the dynamic soaring optimal path problem as a dynamic optimization problem. To facilitate solving this dynamic optimization problem numerically, the equations were expressed in discrete form. The first step of this process was to express the point mass equations of motion parametrically.

Equations (1) through (6), when expressed in parametric form, become the following.

$$u(t) = u(t_0) + \int_{t_0}^{t} \dot{u}(t)dt \tag{17}$$

$$\psi(t) = \psi(t_0) + \int_{t_0}^{t} \dot{\psi}(t)dt \tag{18}$$

$$\gamma(t) = \gamma(t_0) + \int_{t_0}^{t} \dot{\gamma}(t)dt \tag{19}$$

$$h(t) = h(t_0) + \int_{t_0}^{t} \dot{h}(t)dt \tag{20}$$

$$E(t) = N(t_0) + \int_{t_0}^{t} \dot{E}(t)dt \tag{21}$$

$$N(t) = N(t_0) + \int_{t_0}^{t} \dot{N}(t)dt \tag{22}$$

Using equations (17) through (22)**,** the state equations could be analyzed using discrete time increments. The time interval was defined as:

$$t_0 \le t \le t_f \tag{23}$$

When the time interval was divided into *N* discrete steps, then time became defined by the following.

$$t_i = t_0 + N\Delta T \tag{24}$$

Where:

t_i is the time at the i^{th} step

ΔT is the time increment defined as $\frac{t_f - t_0}{N}$

Hence, the sailplane's flight state at any "i^{th}" time, t_i could be expressed as:

$$S(i) = \begin{bmatrix} u(i) \\ \psi(i) \\ \gamma(i) \\ h(i) \\ E(i) \\ N(i) \end{bmatrix} \quad where \quad i = 0,1,2,...N \tag{25}$$

The sailplane state vector shown in equation (25) was subject to the 2x1 control vector comprised of C_L (coefficient of lift), and ϕ (bank angle). This control vector is shown below in discrete form.

$$U(i) = \begin{bmatrix} C_L(i) \\ \phi(i) \end{bmatrix} \quad where \quad i = 0,1,2,...N-1 \tag{26}$$

For sake of visualization, C_L and ϕ could be thought of controls used to position the sailplane in three dimensional space, much like a pilot would deflect aileron, rudder, and elevator for this task.

Expressing the equations in this parametric form facilitated the use of Euler's integration technique to propagate state equations (1) through (6) forward in time. Since Euler's integration technique is sensitive to the magnitude of the time step used, a time convergence study was accomplished in order to determine that a time step of approximately 0.3 seconds was sufficient for this research to allow for convergence. By using this technique, the discrete state equations became:

$$S(i+1) = f(S(i), U(i), \Delta T) = \begin{bmatrix} u(i+1) \\ \psi(i+1) \\ \gamma(i+1) \\ h(i+1) \\ E(i+1) \\ N(i+1) \end{bmatrix} = \begin{bmatrix} u(i) + \dot{u}(i)\Delta T \\ \psi(i) + \dot{\psi}(i)\Delta T \\ \gamma(i) + \dot{\gamma}(i)\Delta T \\ h(i) + \dot{h}(i)\Delta T \\ E(i) + \dot{E}(i)\Delta T \\ N(i) + \dot{N}(i)\Delta T \end{bmatrix} \quad where \quad i = 0,1,2 \ldots N-1 \tag{27}$$

To help ensure a realistic converged solution, the optimized trajectory was subject to constraints placed on the control vectors and terminal states. The control inputs were limited by the following restrictions.

$$\begin{gathered} C_{L_{MIN}} \le C_L(i) \le C_{L_{MAX}} \\ \phi_{MIN} \le \phi(i) \le \phi_{MAX} \end{gathered} \tag{28}$$

Bank angles were limited to a maximum of ±120° to enforce compliance with USAF low altitude safety restrictions. The C_L was limited such that it could not exceed 1.329, the maximum lift coefficient capability of the sailplane as reported by the SENIOR IDS test team (Borror, 2004:17). The C_L was also limited to not be less than zero so as to minimize the possibility of negative *g* "bunting" at low altitude. Detailed state and control vectors, however, were not enough to begin optimization runs. The optimization routine also required an initial guess at a control sequence and a list of sailplane terminal state constraints.

Much like Da Vinci or Lord Rayleigh, modeling for this initial guess at a dynamic soaring profile was develop by studying the flight of the Albatross sea bird. This bird is well known for its ability to soar great distances across the ocean without flapping its wings through its innate mastery of the dynamic soaring technique. A typical Albatross flight profile is shown below in Figure 17 (Hoppi Segelflug Website).

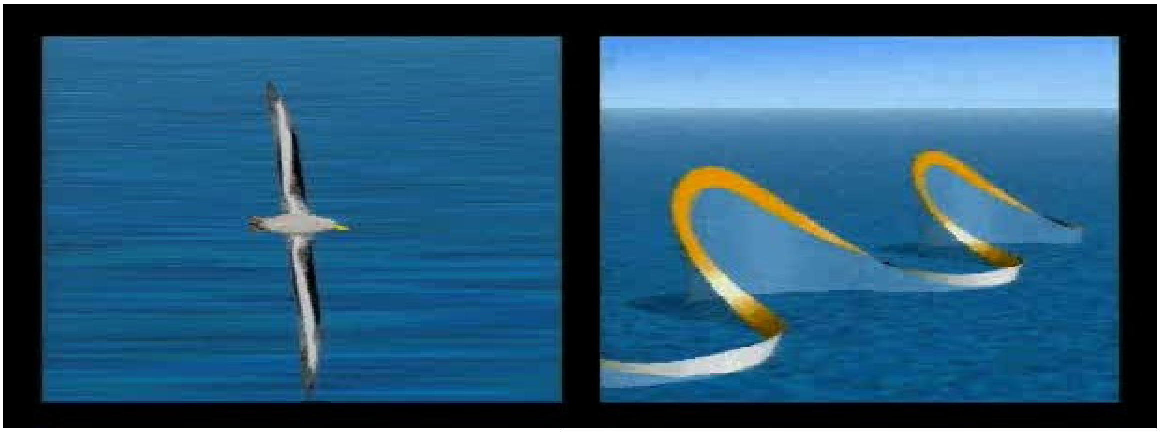

Figure 17. Albatross on a Dynamic Soaring Profile

By observation, this profile is cyclical in nature. The final heading, altitude, and flight path angle are identical to the initial values of these parameters. This profile was approximated by functions that varied the control inputs according to the following equations:

$$
\begin{aligned}
&C_L(i) = \left(K_{C_L} C_L - C_{L_{lf}}\right)\sin\left(\pi \frac{i}{N}\right) + C_{L_{lf}} \\
&\phi(i) = K_{\phi} 120 \frac{\pi}{180} \sin\left(3\pi \frac{i}{N} + \pi\right)
\end{aligned}
\qquad (29)
$$

Where:

K_{CL} and K_{φ} = parameters that could be adjusted between zero and one to vary the aggressiveness of the initial maneuver
C_{Llf} = C_L required for level flight at the maneuver starting airspeed

In order to minimize the potential for noise in actual flight test data, only one cycle of the Albatross trajectory was desired. This prevented errors from one cycle of dynamic soaring from corrupting subsequent cycles. Hence, to build this “half-wave” shape, these control input sinusoids were allowed to propagate forward in time to only half of their respective periods. The resulting three dimensional profile was similar enough in shape to one cycle of the actual Albatross dynamic soaring trajectory. This allowed for an optimization routine to build on this initial trajectory and converge to an appropriately shaped solution. This initial trajectory shape, however, was very dependent on choosing an appropriate starting velocity.

The Maneuvering Airspeed of the sailplane was chosen as an initial guess at a dynamic soaring entry speed. Maneuvering Airspeed was defined by the Federal Aviation Administration as the maximum speed where full, abrupt control movement could be used without overstressing the airframe (FAA, 2004:G-10). This airspeed decreases with increasing gross weight. Maneuvering Airspeed for the L-23 at the projected test gross weight of 1124 lbs was defined by the flight manual as 143 ft/s or 85 knots indicated airspeed (KIAS). This airspeed represented an acceptable middle ground between stall airspeed and the never exceed airspeed, and was sufficient to form the appropriate trajectory shape. Based on the analysis described above, the final altitude, heading, and flight path angle had to equal the initial values of these respective states. The terminal constraints required to enforce the Albatross half wave trajectory shape are shown below.

$$\chi_{t_f}(N) = \begin{bmatrix} h(t_f) - h(t_o) \\ \psi(t_f) - \psi(t_o) \\ \gamma(t_f) - \gamma(t_o) \end{bmatrix} = 0 \tag{30}$$

Finally, an optimization objective function needed to be developed that was simple, but still emphasized the end goal of dynamic soaring. Ultimately, the goal of an optimal trajectory was to arrive at the final position of the path with the maximal amount of energy achievable given the environmental conditions. This goal was captured by the objective function shown below.

$$\mu_f(N) = -E_s(N) = -\left[h(N) + \frac{V_t(N)^2}{2g} \right] \tag{31}$$

The complete optimization problem was defined as:

$$\left.\begin{aligned}
&\min_{U(i),\Delta T} \quad \mu_f(N) \\
&\text{Subject to:} \\
&S(i+1) = f\left[S(i), U(i), \Delta T\right] \\
&i = 0,1,2,\ldots N-1 \\
&\chi_{t_f}\left[S(N)\right] = 0 \\
&C_{L_{MIN}} \le C_L(i) \le C_{L_{MAX}} \\
&\phi_{MIN} \le \phi(i) \le \phi_{MAX}
\end{aligned}\right\} \tag{32}$$

In addition to optimizing over the control sequence, the time increment, *ΔT*, was included to allow the dynamic optimization routine free reign over the required trajectory time of flight.

When the equality constraints were adjoined to the objective function using vectors of Lagrange multipliers, defined as λ and ν, the augmented objective function became:

$$J = \mu_f(N) + \upsilon^T \chi_{t_f} + \sum_{i=0}^{N-1} \lambda^T(i+1)\Big[f\left[S(i), U(i), \Delta \mathrm{t}\right] - S(i+1)\Big] + \lambda^T(0)\left[S_0 - S(0)\right] \tag{33}$$

The Hamiltonian function for this problem was defined as:

$$H(i) = \lambda^T(i+1) f\left[S(i), U(i), \Delta t\right] \tag{34}$$

The combination of terminal costs and constraints was defined as

$$\Phi(N) = \mu(N) + \nu^T \chi(N) \tag{35}$$

The boundary conditions and Euler-Lagrange Equations used to solve the dynamic optimization problem for the optimal control sequence were:

$$\left.\begin{aligned} &S(i) = f\left[S(i), U(i), \Delta t\right] \\ &\lambda^T(i) = H_S(i) = \lambda^T(i+1)\, f_S\left[S(i), U(i), \Delta t\right] \\ &H_U(i) = \lambda^T(i+1)\, f_U\left[S(i), U(i), i\right] = 0 \\ &i = 0, 1, 2, \ldots N-1 \\ &S(0) = S_0 \\ &\lambda^T(N) = \Phi_S = \mu_S + \upsilon^T \chi_S \end{aligned}\right\} \tag{36}$$

The Transversality condition was defined as:

$$\Phi_{\Delta T} + \sum_{i=0}^{N-1} H_{\Delta T}(i) = 0 \tag{37}$$

The subscripts *S*, *U*, and *ΔT* in equations (36) and (37) indicate partial derivatives.

The dynamic optimization problem posed above was solved using MATLAB® and the Optimization Toolbox. Note that the Euler-Lagrange Equations above do not account for the inequality constraints imposed on the control inputs; however, these constraints were enforced within the optimization algorithm. The results of this dynamic optimization are presented in the following section.

Point Mass Dynamic Optimization Results

A comparison trajectory analysis was performed in order to illustrate the energy benefits of dynamic soaring. The first step in this analysis was accomplished by modeling a dynamic soaring profile in zero wind conditions. This established a baseline set of maneuver and energy data with which to compare other trajectories against. The results from this trajectory dynamic optimization are presented in detail in the following set of figures beginning with Figure 18.

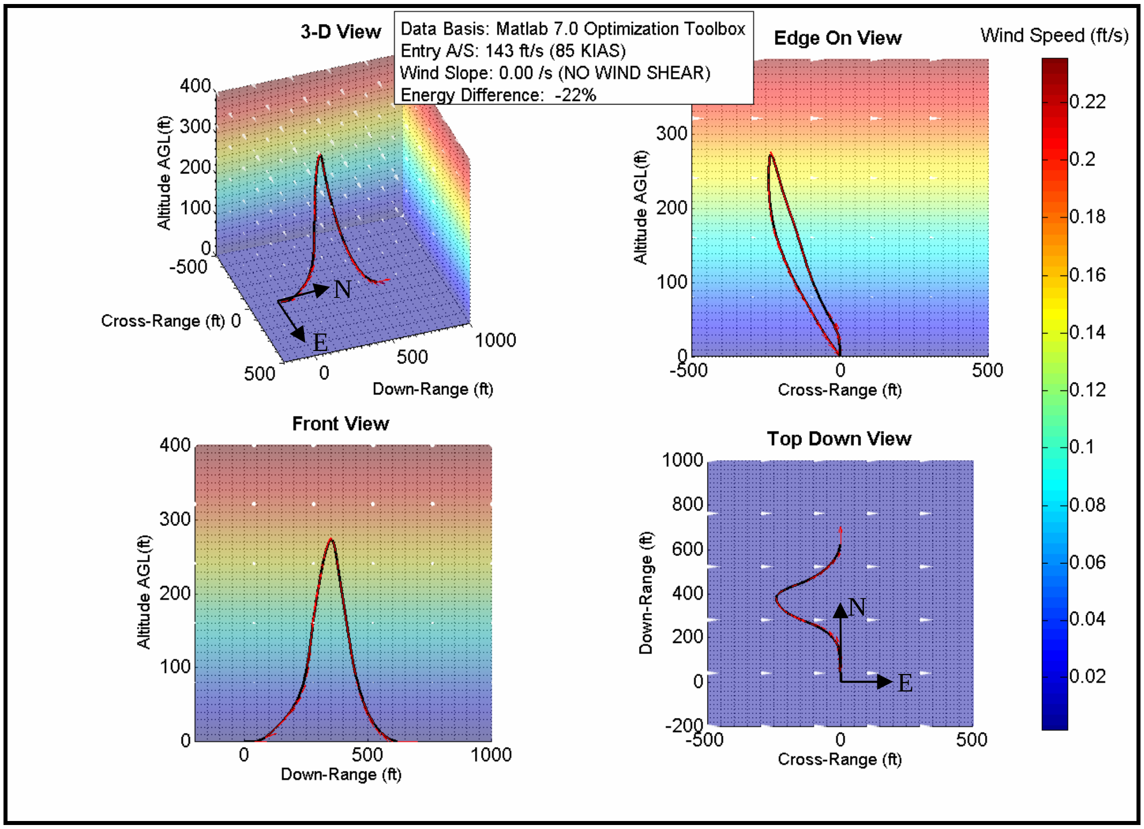
Data Basis: Matlab 7.0 Optimization Toolbox
Entry A/S: 143 ft/s (85 KIAS)
Wind Slope: 0.00 /s (NO WIND SHEAR)
Energy Difference: -22%

Figure 18. Dynamic Soaring 4-View Trajectory (No Wind Shear Baseline)

Figure 18 shows four different perspectives of the same dynamic soaring profile in zero wind shear conditions. The sailplane's position was initialized at the origin of an inertial North-East-Down reference frame with the sailplane pointed North. The white translucent cones depict the direction and strength of the wind. In all cases, the wind is blowing directly from the West and the wind speed increases linearly with altitude according to the given wind shear. In this particular case, a wind shear of 0.001 ft/s / ft, or a 0.1 knot increase in wind velocity per 100 feet of altitude gain, was used to approximate a zero wind shear gradient in order to avoid numerical singularities in some state equations. The color bar depicts wind strength, with blue colors indicating lower velocity winds and red/orange colors depicting higher velocity winds. The black line represent the sailplane's trajectory while the red arrows attached to the black line represent the velocity vector of the sailplane at that corresponding trajectory position. This symbology combines to yield insight into dynamic soaring profiles.

In this particular case, the optimal dynamic soaring profile in a zero wind shear condition resulted in a loss of 78 specific energy height feet. This equated to an energy loss of 22%. Even with the very light wind shear used in this case, a quick glance at Figure 18 reveals that the sailplane indeed climbed into the headwind, reversed direction quickly once it nearly ran out of airspeed, and descended with the tailwind. This is in keeping with earlier mathematical predictions provided by equation (16). Furthermore, this trajectory matched closely the hairpin shape of the dynamic soaring profile flown by the Albatross in wind shears over the ocean. Further detail about this trajectory is shown in Figure 19.

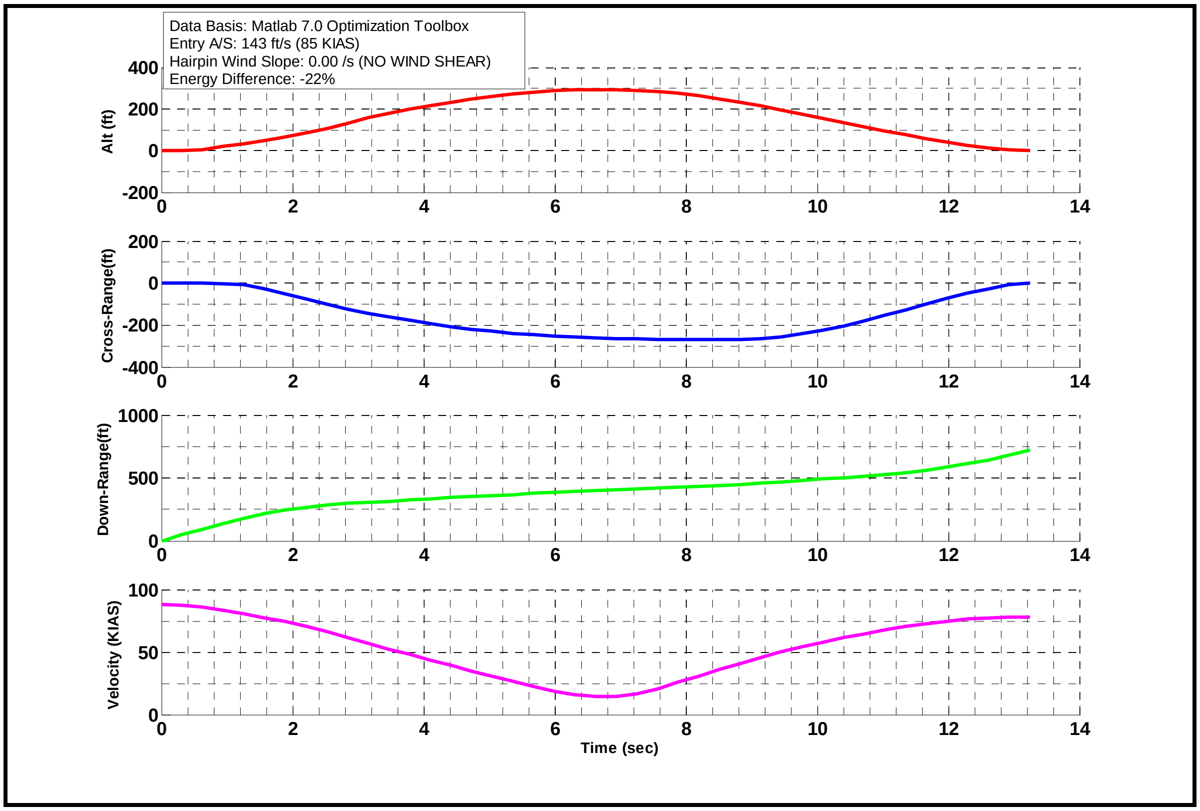

Figure 19. Trajectory Data (No Wind Shear Baseline)

During the flight of this trajectory, the sailplane traveled down-range *(North)* approximately 600 feet and achieved a peak altitude gain of approximately 275 feet before returning back to the initial altitude (*0 ft*). Because of the very light wind shear, the sailplane was able to return to its initial cross-range position (*0 ft*) after achieving a maximum cross range distance of approximately -200 ft (*200 ft West of the initial position*). Since the trajectory was structured such that the sailplane returned to its initial altitude, all changes in energy state were represented in the sailplane's final velocity as compared to its initial velocity. In this example, the sailplane began at 85 knots indicated airspeed (KIAS) and finished at 75 KIAS. This accounted for the sailplane's loss of 22% of its initial energy. The maneuvering required to achieve this trajectory is shown in Figure 20.

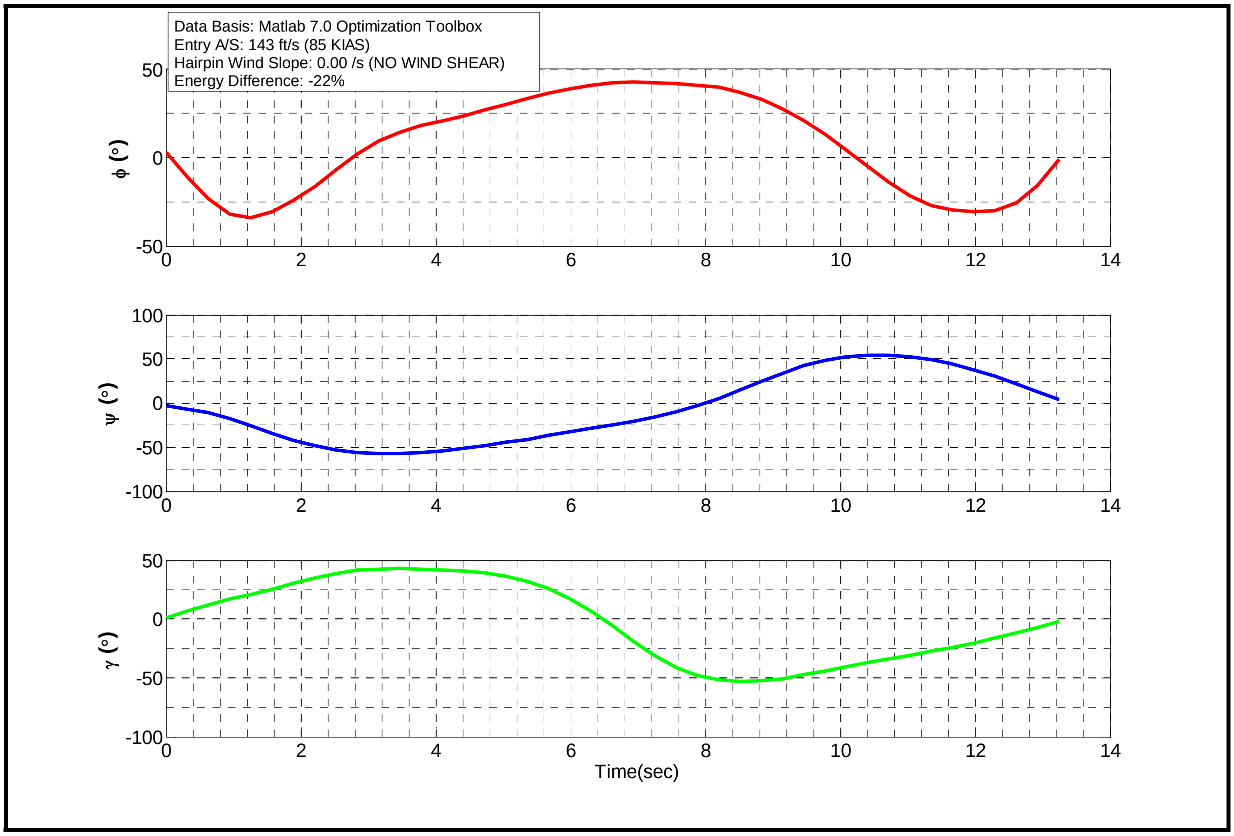

Figure 20. Euler Angles (No Wind Shear Baseline)

Figure 20 depicts bank angle (ϕ), heading angle (ψ), and flight path angle (γ) vs. time during the dynamic soaring trajectory. In the figure, negative angles equate to left bank angles, heading changes to the West, and/or flight path angles below the horizon while positive angles represent the opposite direction of these maneuvers respectively. Collectively, these figures depict a sailplane that entered a climbing left hand turn to the West with decreasing airspeed for approximately the first 6 seconds. This was followed by a descending right hand turn with increasing airspeed as the sailplane returned to the starting altitude, heading, and cross range position. Of note, the sailplane achieved a maximum left bank angle of -40°, and a maximum right bank angle of 45°. Heading changes were limited to a cone of ± 60º from North. During the climbing portion of the trajectory, the sailplane achieved a maximum flight path angle approximately 45º above the horizon while climbing, and a maximum -50º nose low flight path angle during the descending portion of the trajectory. Aerodynamic performance during this dynamic soaring trajectory is presented in Figure 21.

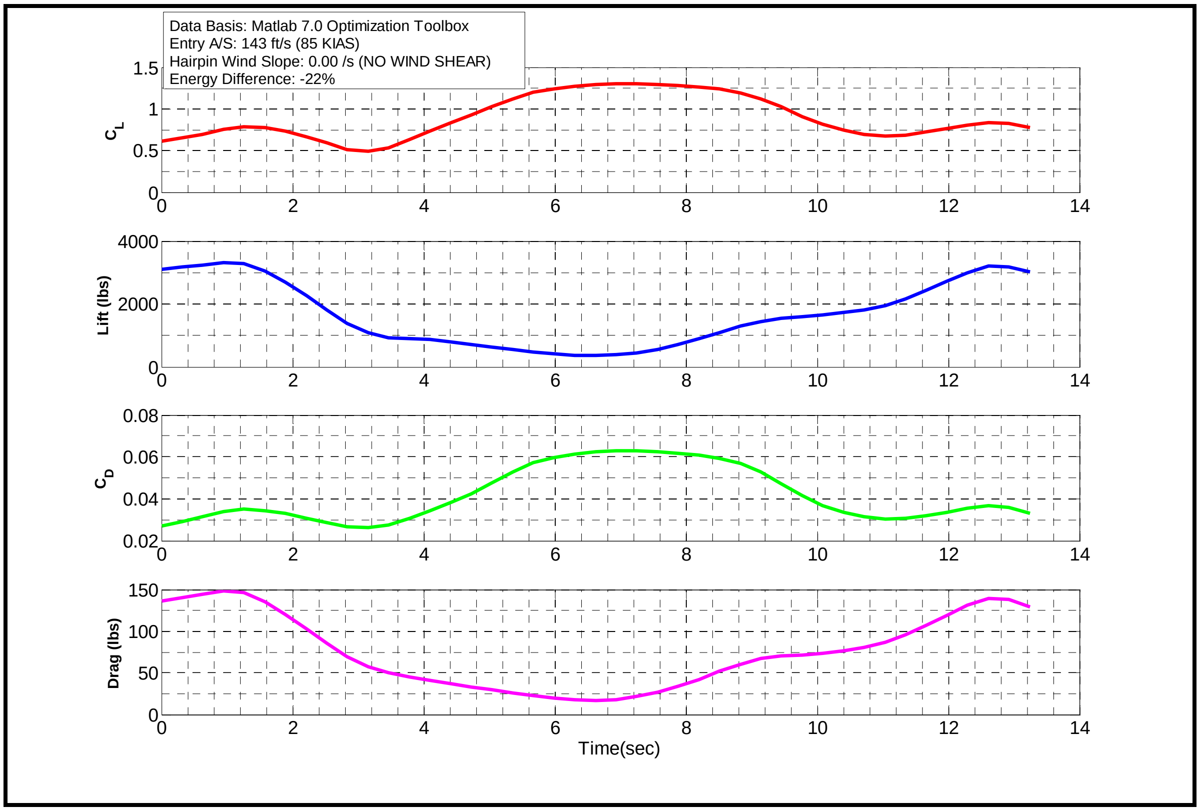

Figure 21. Aerodynamic Performance (No Wind Shear Baseline)

Of particular note during this trajectory was the initial rolling/climbing pull to the West and the final dive recovery. At these stages of the profile, the sailplane was traveling relatively fast (75-85 KIAS), as compared to the airspeeds experienced elsewhere in the trajectory, and generating approximately 5000 lbs of lift. Since the sailplane's weight in this analysis was at its maximum gross weight of 1124 lbs, these pulls represented an acceleration of nearly 5*g*'s. From a practical employment standpoint, these portions of the trajectory represented the greatest risk of an over-*g* since the published limit load factor of the sailplane in this weight configuration was 5.33 g’s (LET,1993:1-5 - 2-3). As will be discussed in chapter III of this Thesis, this fact was a contributing factor to a modified dynamic soaring profile used in actual flight test in order to provide an adequate flight safety margin.

Figure 21 also illustrates the relative magnitudes of lift and drag for a sailplane in maneuvering flight. While the lift force was generally on the order of thousands of pounds, the drag generated was only on the order of hundreds of pounds. This is testament to the relatively good lift to drag performance of sailplanes as opposed to other air vehicles. This point also illustrates the fact that relatively small forward rotations of the lift vector due to flight through wind shear can be significant enough to generate a horizontal component of lift large enough to offset the drag loses.

Figure 18 through Figure 21 illustrate the fine details of this dynamic soaring hairpin trajectory and ultimately form the basis for the energy state performance of the sailplane during this maneuver. This energy performance is illustrated in Figure 22.

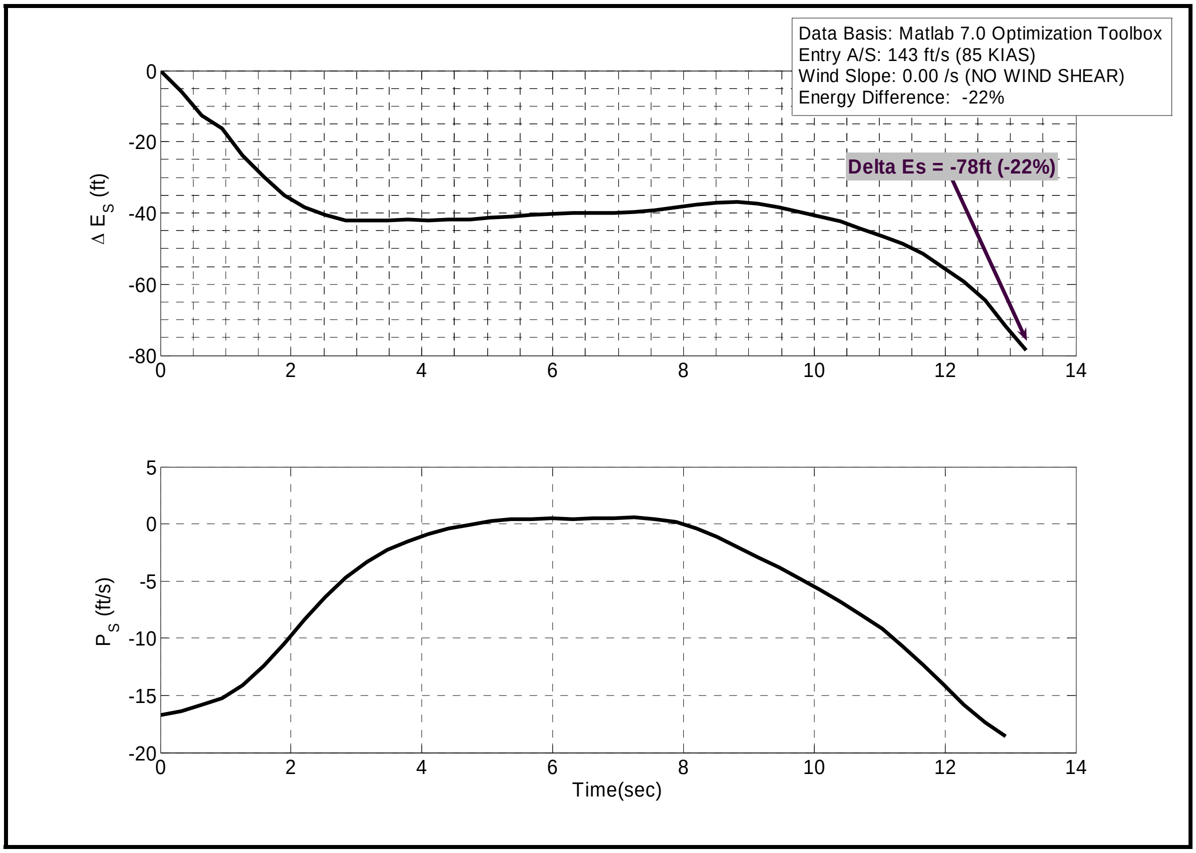

Figure 22. Energy State Performance (No Wind Shear Baseline)

Figure 22 is the most significant figure of this set as it shows specific energy, E_s, and specific excess power, P_s, vs. time. The top chart in Figure 22 depicts the Δ specific energy height of the sailplane at any moment in time along the trajectory. In the baseline case, the sailplane lost 78 specific energy height feet from its initial energy height. The underlying cause for this loss is shown in the bottom chart in Figure 22. This chart illustrates specific excess power vs. time. Since there was essentially no wind shear, the energy losing P_s performance was due exclusively to drag *(the brief positive P_s portions of the trajectory were due to effects from the very light wind shear used to approximate zero wind shear conditions).*

Now that a baseline dynamic soaring hairpin profile had been constructed, performance comparisons could now be made by introducing various wind shear strengths. For instance, a wind shear of 0.04ft/s / ft was used to construct the following set of figures. This wind shear was chosen since, according to the ten year compiled weather data from the NASA DFRC weather observatory, it represented a relatively strong wind shear that was occasionally generated across the Rogers dry lakebed by natural phenomenon such as temperature inversions and boundary layer winds. This wind shear was equivalent to a 2.4 knot wind speed increase per 100 feet of altitude gain. The results are shown in Figure 23.

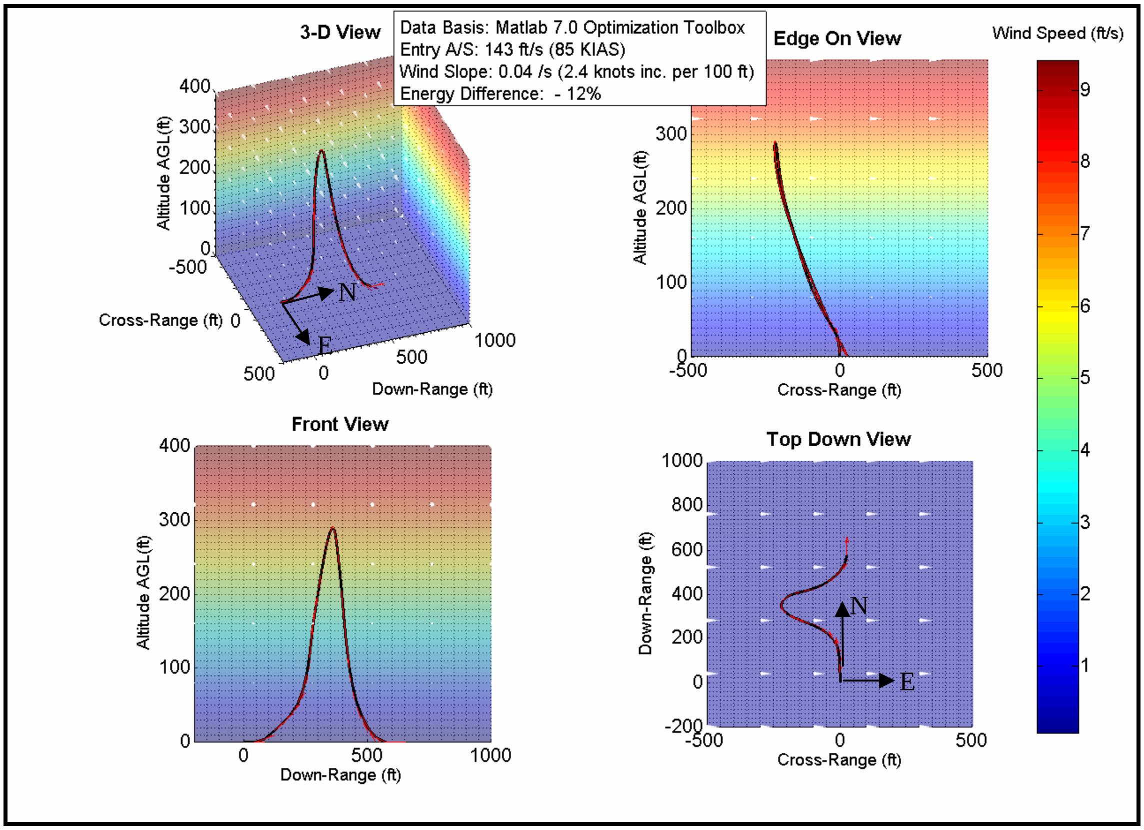

Data Basis: Matlab 7.0 Optimization Toolbox
Entry A/S: 143 ft/s (85 KIAS)
Wind Slope: 0.04 /s (2.4 knots inc. per 100 ft)
Energy Difference: - 12%

Figure 23. Hairpin 4-View Trajectory (0.04ft/s / ft Wind Shear)

In this case, since the sailplane was able to extract energy from the existing 0.04 ft/s / ft wind shear, its energy loss was only 42 specific energy height feet. This equated to an energy loss of only 12% or only approximately half as much energy loss as compared to the baseline profile. This was a tremendous energy state improvement. Further comparisons with the baseline trajectory are provided in Figure 24.

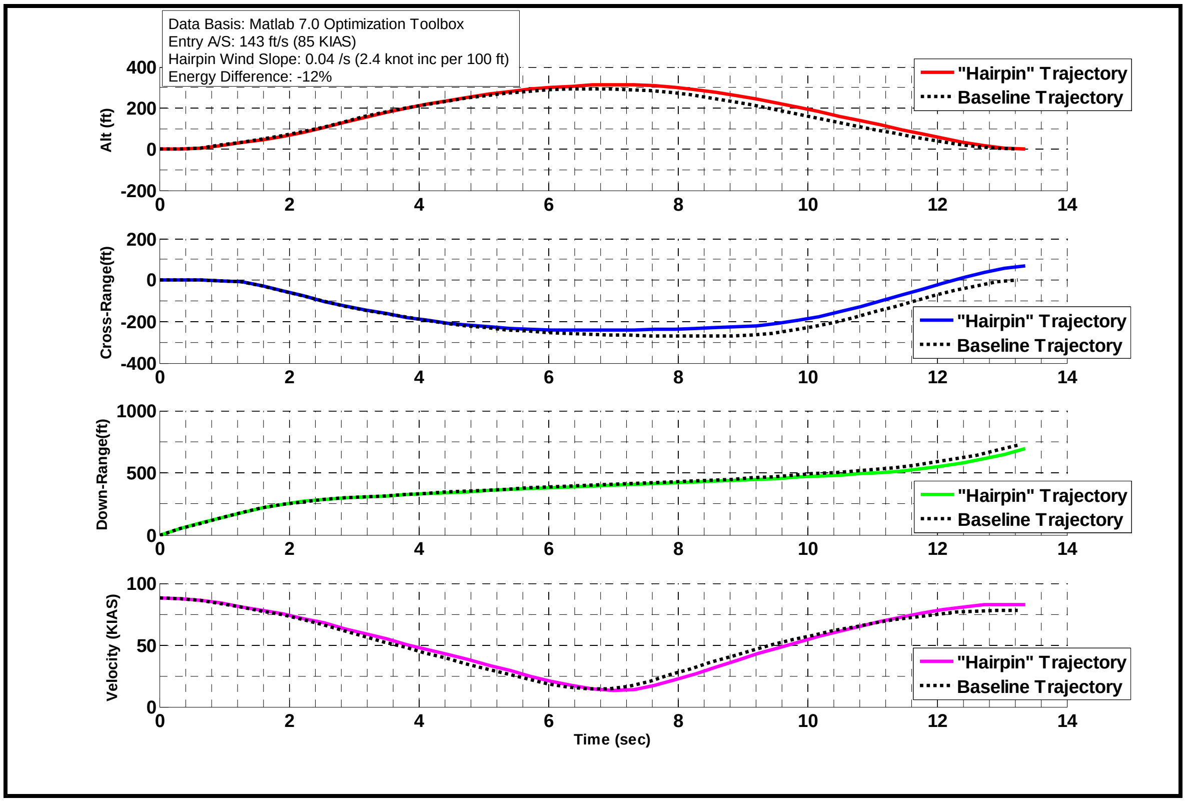

Figure 24. Trajectory Comparison (0.04ft/s / ft Wind Shear)

With a 0.04 ft/s / ft wind shear, the maximum altitude, cross-range, and downrange distances increased by only approximately 20 to 30 feet. The most significant change in distance measurements was that the stronger wind shear caused the final cross range position to drift downwind from the initial start position by approximately 70 feet. Because the range increases were relatively modest, the trajectory time of 12.4 seconds was nearly identical to the baseline trajectory time of 12.6 seconds. Furthermore, the minimum airspeed experienced during the profile only decreased by 3 KIAS as compared to the baseline trajectory. However, because of the stronger wind shear, the sailplane recovered back to 80 KIAS at the end of the profile, a 5 KIAS increase over the baseline trajectory final velocity. This resulted in the improved energy state performance as compared to the baseline trajectory. However, one of the most significant observations from Figure 24 is the relatively minor differences between the baseline trajectory and the hairpin trajectory in a 0.04 ft/s / ft wind shear. This is further emphasized by Figure 25.

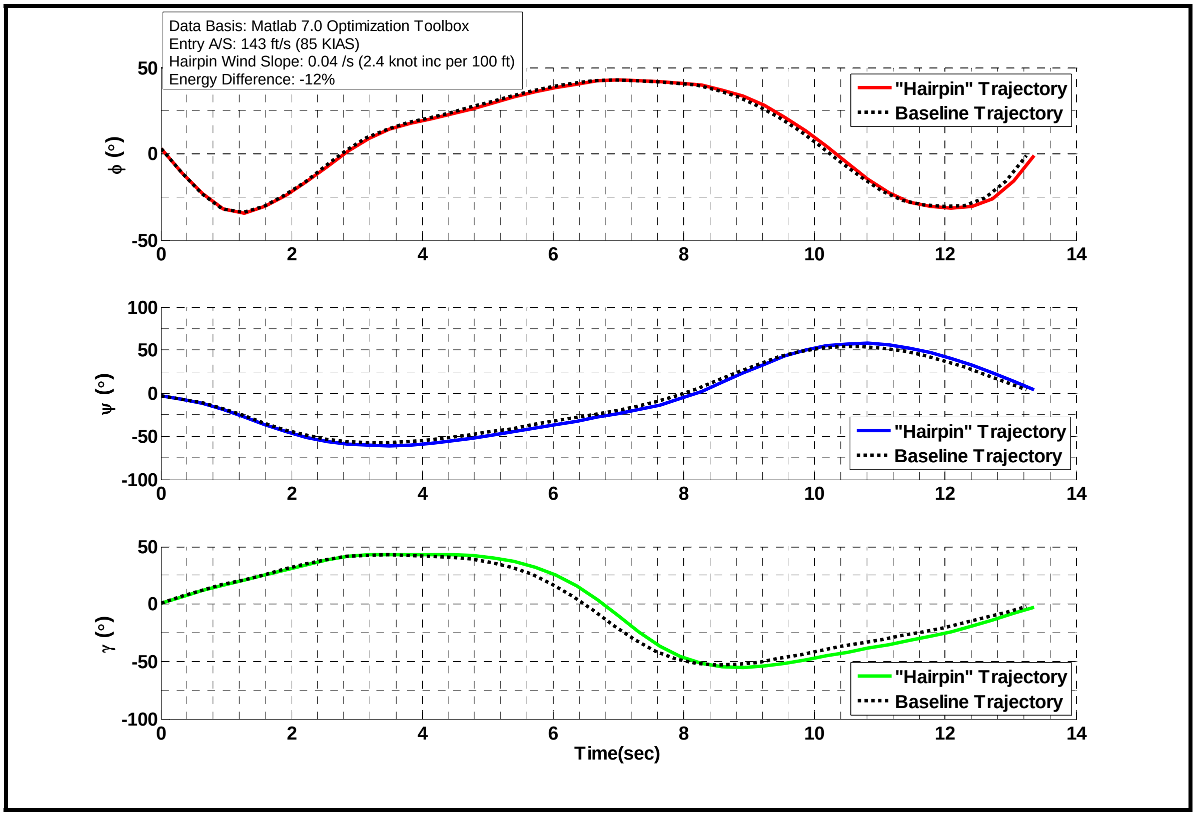

Figure 25. Euler Angle Comparison (0.04ft/s / ft Wind Shear)

Here, bank, heading, and flight path angles were all very similar to the baseline trajectory with only slight increases in magnitudes on the order of 3º to 5º. These changes would be relatively imperceptible to a pilot trying to fly these trajectories.

Because of the similarities in the profiles, the aerodynamic performance of the sailplane was also very similar to the baseline profile. This is illustrated in Figure 26.

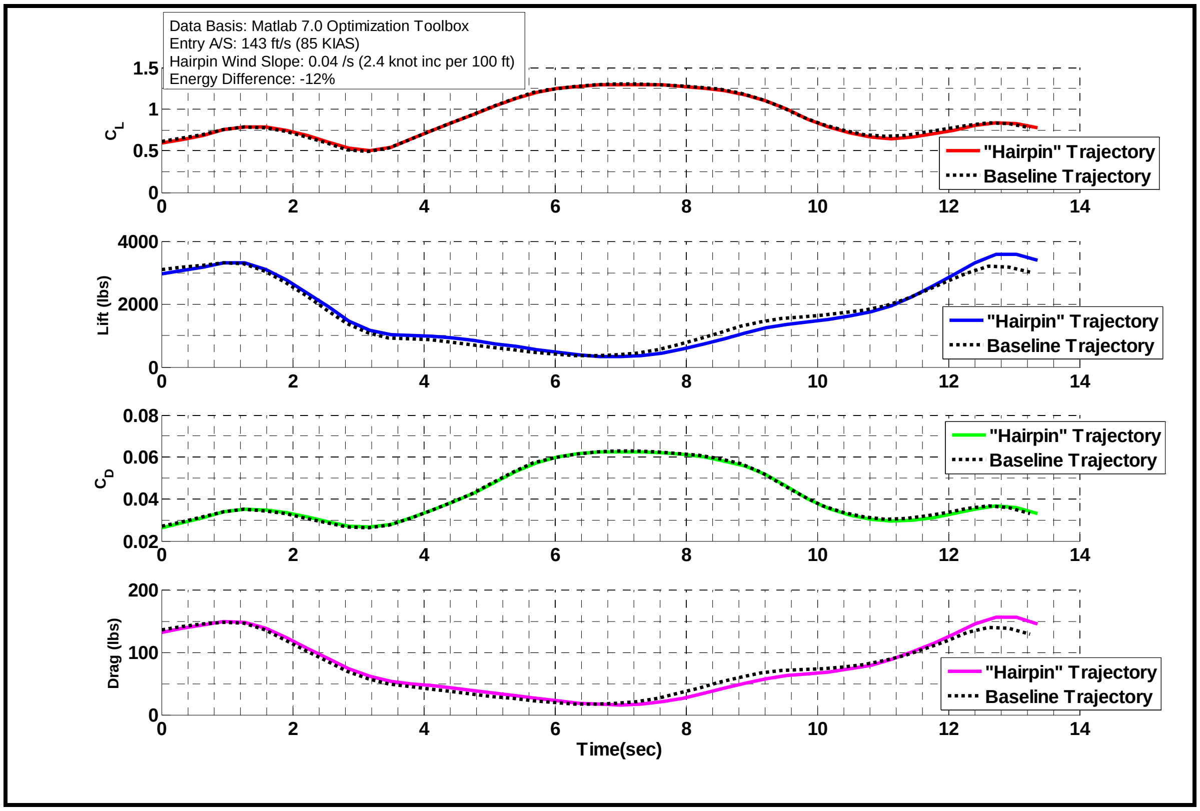

Figure 26. Aerodynamic Performance Comparison (0.04ft/s / ft Wind Shear)

Figure 26 illustrates that the sailplane aerodynamic performance in this profile was nearly identical to its performance in the baseline trajectory. Again, the over-*g* potential existed at the beginning and end of the profiles. While sailplane performance, thus far, was nearly identical to the baseline trajectory, the differences in energy state performance, as shown in Figure 27, were significant.

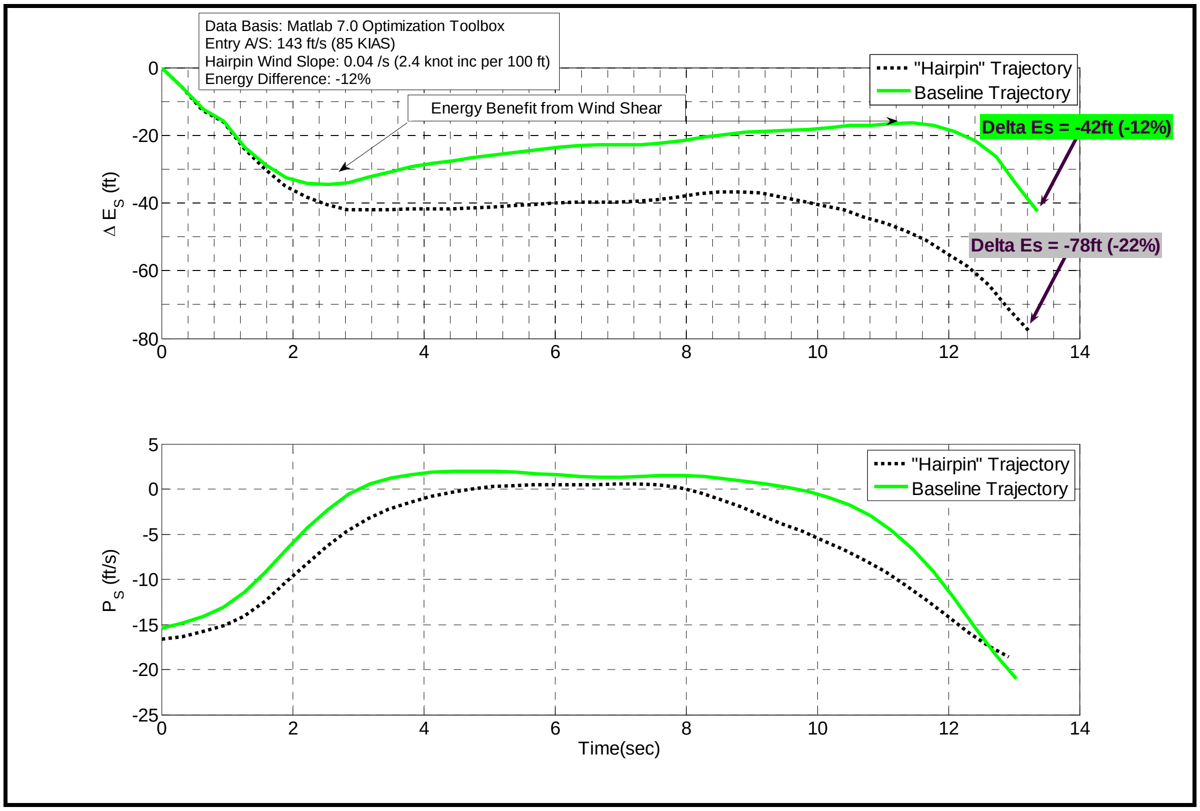

Figure 27. Hairpin Energy State Performance Comparison (0.04 ft/s / ft Wind Shear)

The top chart in Figure 27 illustrates the effects of flying a dynamic soaring hairpin profile in a wind shear. While the sailplane began its profile with the same E_s as the baseline trajectory, its final E_s was improved by 36 specific energy height feet as compared to the baseline trajectory. The reason for this increase is illustrated in the bottom chart of Figure 27. Here, the initial turn and climb into the headwind resulted in a P_s gain from the wind. At slightly over two seconds into the flight, this P_s gain from the wind was actually significant enough to offset the P_s loss due to drag. Beyond two seconds into the flight, the P_s became neutral to positive for approximately the next four seconds. This same process repeated itself as the sailplane reversed direction and performed a descending right hand turn back to the start altitude, bank, and heading. It was this P_s interplay between drag loss and wind shear gain that improved the final energy state of the sailplane over the baseline case.

In an attempt to further illustrate the wind shear effect on the energy state of the sailplane, the hairpin dynamic soaring maneuver described above was reversed such that the sailplane climbed into a tailwind and descended with a headwind. For this to occur, the sailplane initiated a climbing turn to the East as opposed to the West. The result was an anti-hairpin dynamic soaring maneuver. Since the baseline profile was flown in no wind shear conditions, there was no difference in energy state between a hairpin and anti-hairpin maneuver. However, with a wind shear present, the energy state penalty effect of anti-hairpin maneuvers became apparent. This is illustrated by the following set of figures. Figure 28 illustrates the differences in the orientations of the two maneuvers with respect to the prevailing wind shear.

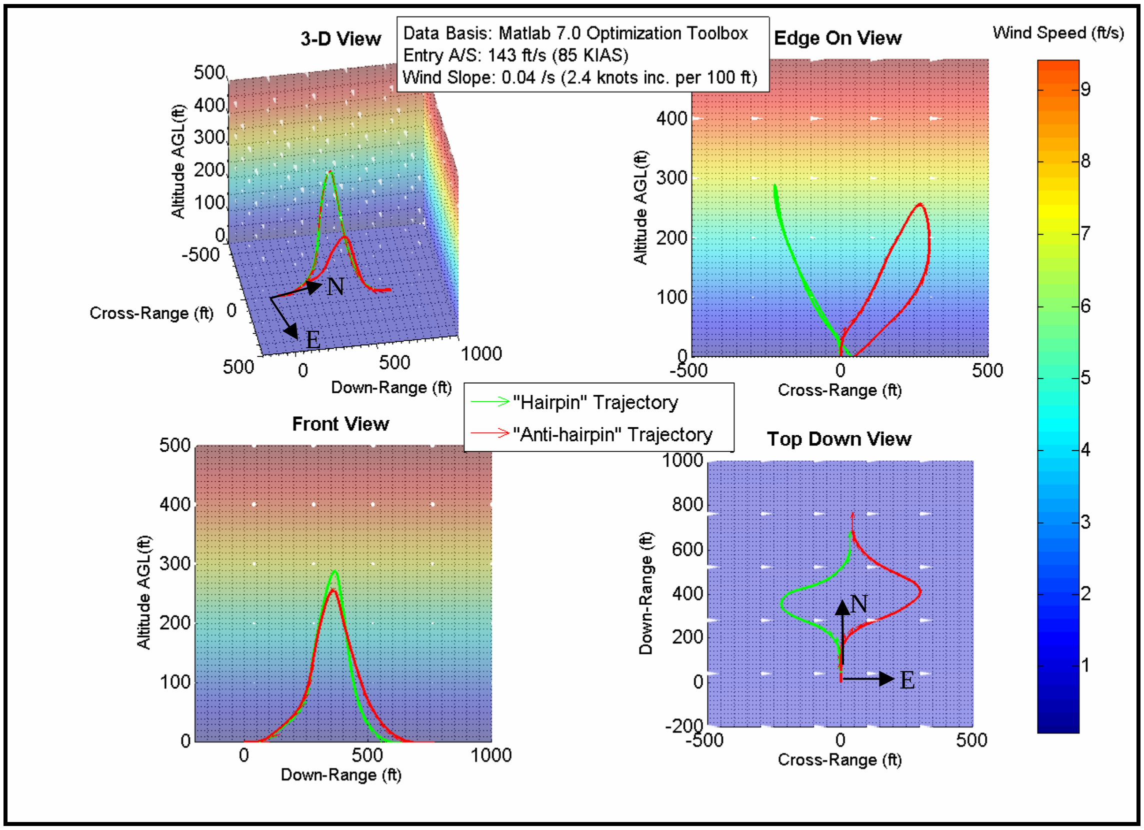

Figure 28. Hairpin vs. Anti-hairpin Trajectory 4-View Comparison (0.04ft/s / ft Wind Shear)

The hairpin, represented by the green line and arrows, and anti-hairpin, represented by the red line and arrows, were essentially mirror images of one another. The differences apparent in the edge on view *(top right)* and the top down view *(bottom right)* in Figure 28 were due exclusively to the wind effects on the shape of the profile. For example, in the anti-hairpin, the sailplane was blown downwind by the tailwind at the beginning of its profile when the sailplane had the greatest amount of airspeed. At the apex of the profile, when the sailplane was at its slowest point of the trajectory, the sailplane had to penetrate against the headwind in order to travel back upwind towards the start cross range position. As a result, the edge on view shape was somewhat distended and, due to the initial push of the tailwind, the final downrange distance shown in the top down view was approximately 70 feet greater than the hairpin maneuver.

However, because of the energy depleting nature of the anti-hairpin maneuver, the hairpin maneuver was able to achieve 25 feet more of altitude gain and finish the maneuver 5 KIAS faster. These differences are shown in greater detail in Figure 29.

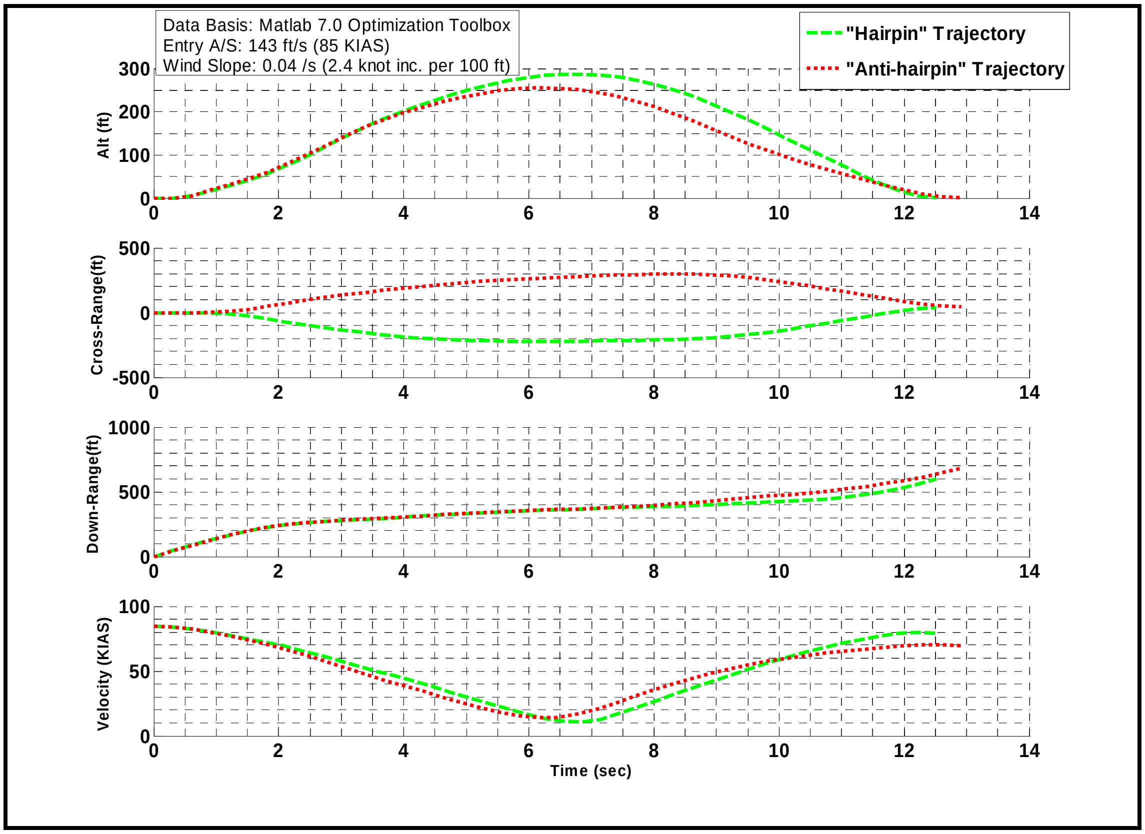

Figure 29. Hairpin vs. Anti-hairpin Trajectory Comparison (0.04ft/s / ft Wind Shear)

Here, the hairpin maneuver is represented by the green dashed line and the anti-hairpin maneuver is represented by the red dotted line.

Figure 30 demonstrates that, from a practical employment standpoint, the control inputs required to execute either maneuver were virtually identical to one another with the exception of the initial turn direction either into or away from the headwind.

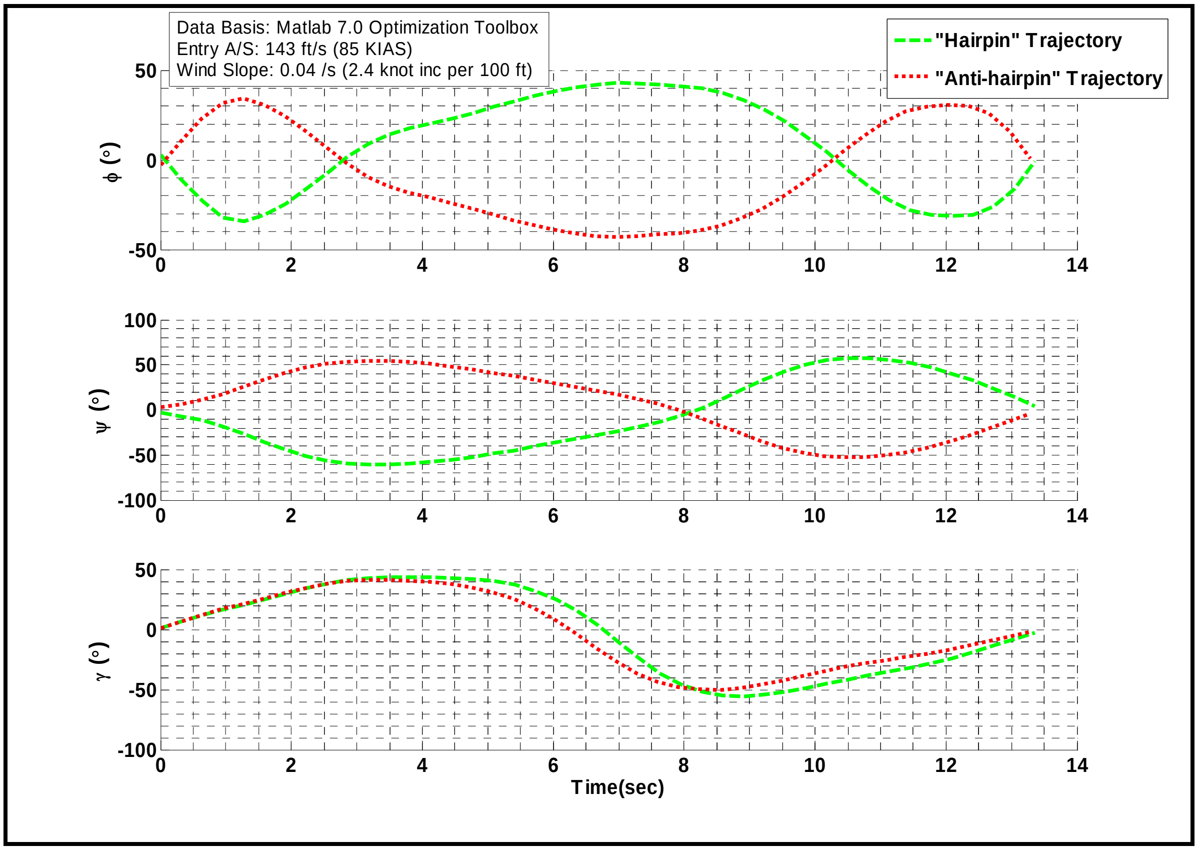

Figure 30. Hairpin vs. Anti-hairpin Euler Angle Comparison (0.04ft/s / ft Wind Shear)

Likewise, Figure 31 illustrates that the aerodynamic performance of the sailplane was similar in both maneuvers. The slight differences in lift and drag at the conclusion of the profiles were primarily due to the minor differences in control inputs caused by wind effects on the shape of the profile described earlier.

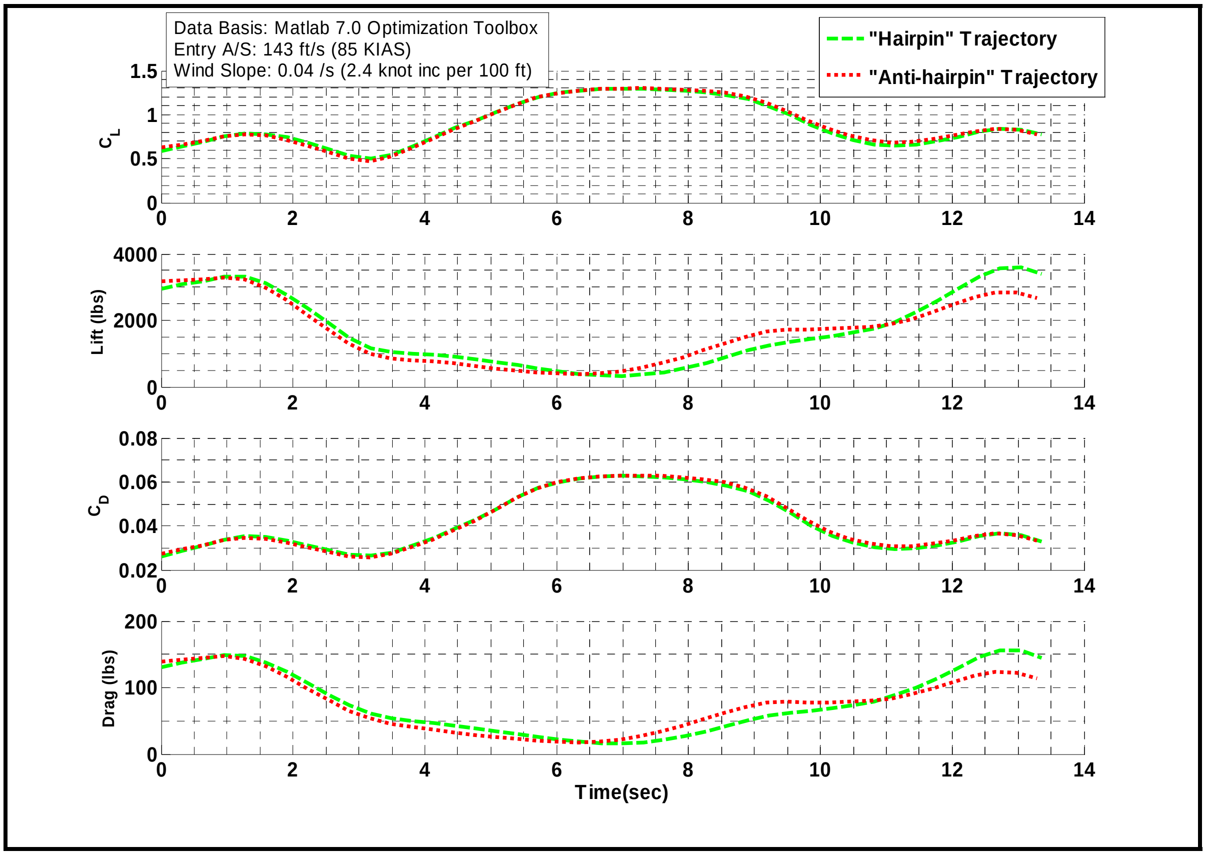

Figure 31. Hairpin vs. Anti-hairpin Aerodynamic Performance Comparison
(0.04ft/s / ft Wind Shear)

The primary difference between the hairpin and anti-hairpin maneuvers was in the energy state performance. This is illustrated in Figure 32.

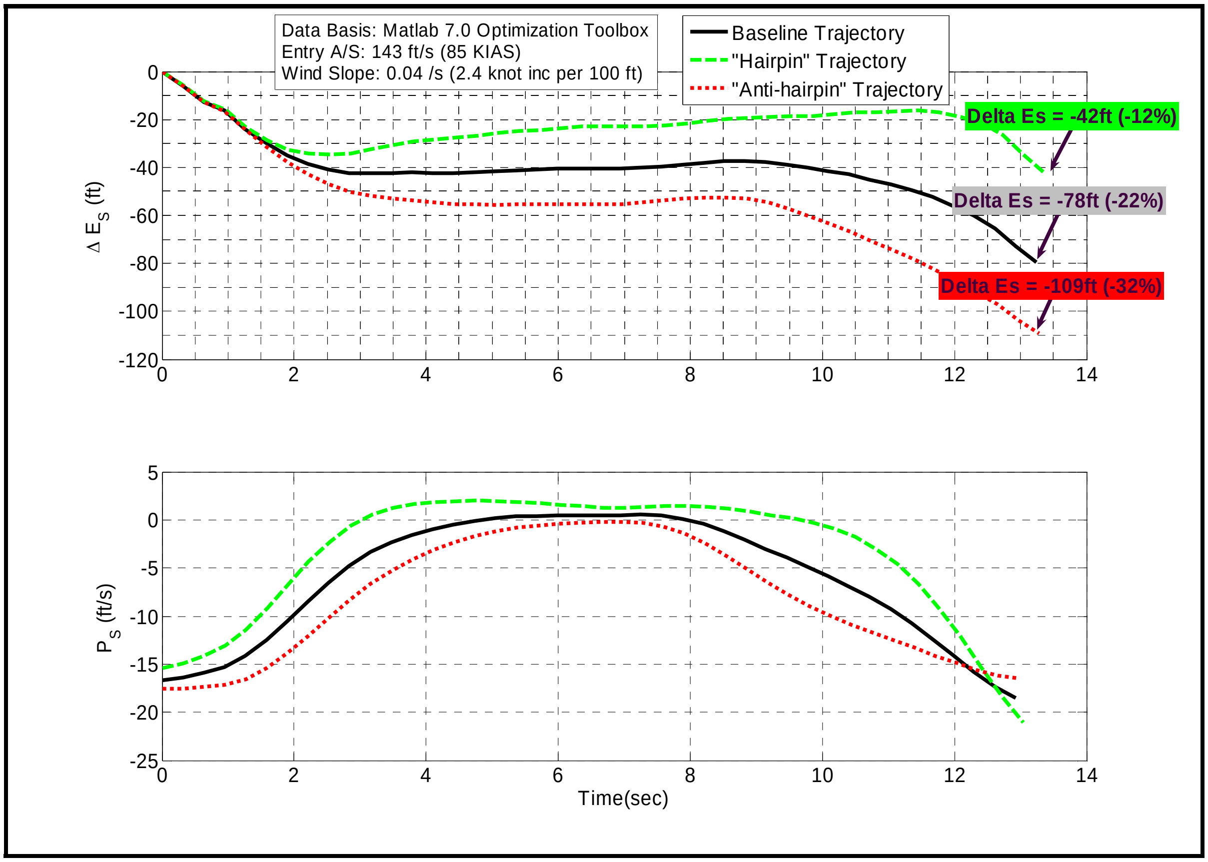

Figure 32. Hairpin/Baseline/Anti-hairpin Energy State Performance Comparison (0.04ft/s / ft Wind Shear)

The top chart in Figure 32 shows the energy benefit of the hairpin maneuver in wind shear when compared to the baseline trajectory in no wind shear and the anti-hairpin profile in wind shear. Based on these dynamic soaring conditions, the hairpin maneuver would have only lost approximately 42 specific energy ft, or -12% of its initial E_s, while the baseline trajectory in no wind shear would have lost 78 specific energy height feet, or 22% of its E_s. The anti-hairpin would have exhibited the worst energy performance of the three with a final E_s loss of 109 feet, fully 32% lower than its initial specific energy. This analysis leads to the importance of properly executed dynamic soaring maneuvers with respect to the direction of the wind shear. It also lends credibility to the flight test approach of executing both hairpin and anti-hairpin maneuvers in order to exacerbate the spread of specific energy data from the baseline trajectory results, thereby enhancing data analysis and conclusions.

To further investigate these effects, the wind shear was decreased to 0.02 ft/s / ft. Based on the compiled weather data from the NASA DFRC weather observatory, this strength of wind shear was very common across the Edwards AFB dry lakebed and would therefore represent the typical dynamic soaring conditions expected during flight test. This wind shear equated to an increase of 1.2 knots per 100 feet of altitude gain.

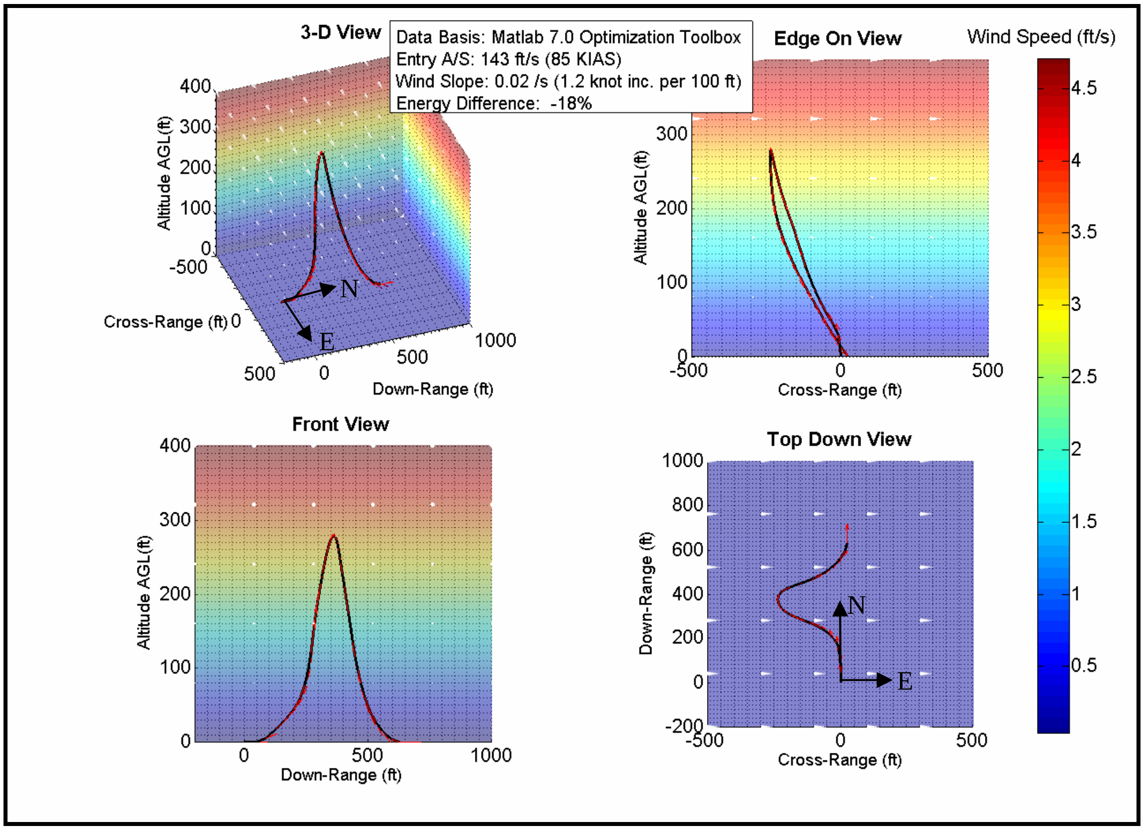
Data Basis: Matlab 7.0 Optimization Toolbox
Entry A/S: 143 ft/s (85 KIAS)
Wind Slope: 0.02 /s (1.2 knot inc. per 100 ft)
Energy Difference: -18%

Figure 33. Hairpin Trajectory 4-View (0.02 ft/s / ft Wind Shear)

With a reduced wind shear strength, the optimal profile was still nonetheless very similar to the baseline trajectory. Just as when the wind shear was at 0.04 ft/s / ft, the primary impact to the shape of the trajectory was a final cross-range position slightly displaced downwind from the start position. Figure 34 provides more information on this trajectory.

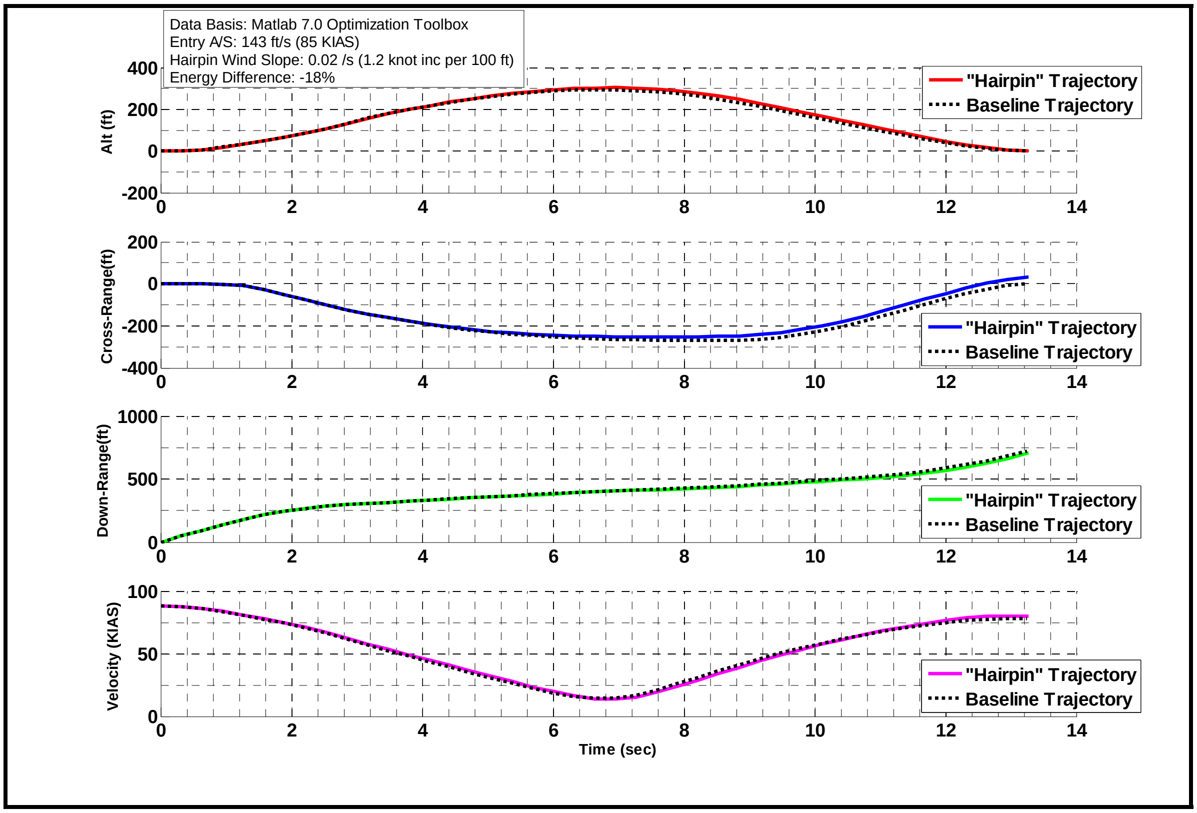

Figure 34. Trajectory Comparison (0.02 ft/s / ft Wind Shear)

Figure 34 illustrates that, next to the slightly displaced final cross-range position, the only significant change from the baseline trajectory was that the final sailplane velocity was 78 KIAS. This return airspeed, only 7 KIAS slower than the start airspeed, accounted for the improved energy state performance of the sailplane through this wind shear condition as opposed to the baseline trajectory in no wind shear.

Despite the improvement in energy performance, the shape of the trajectory remained relatively unchanged from the baseline trajectory as shown in Figure 35.

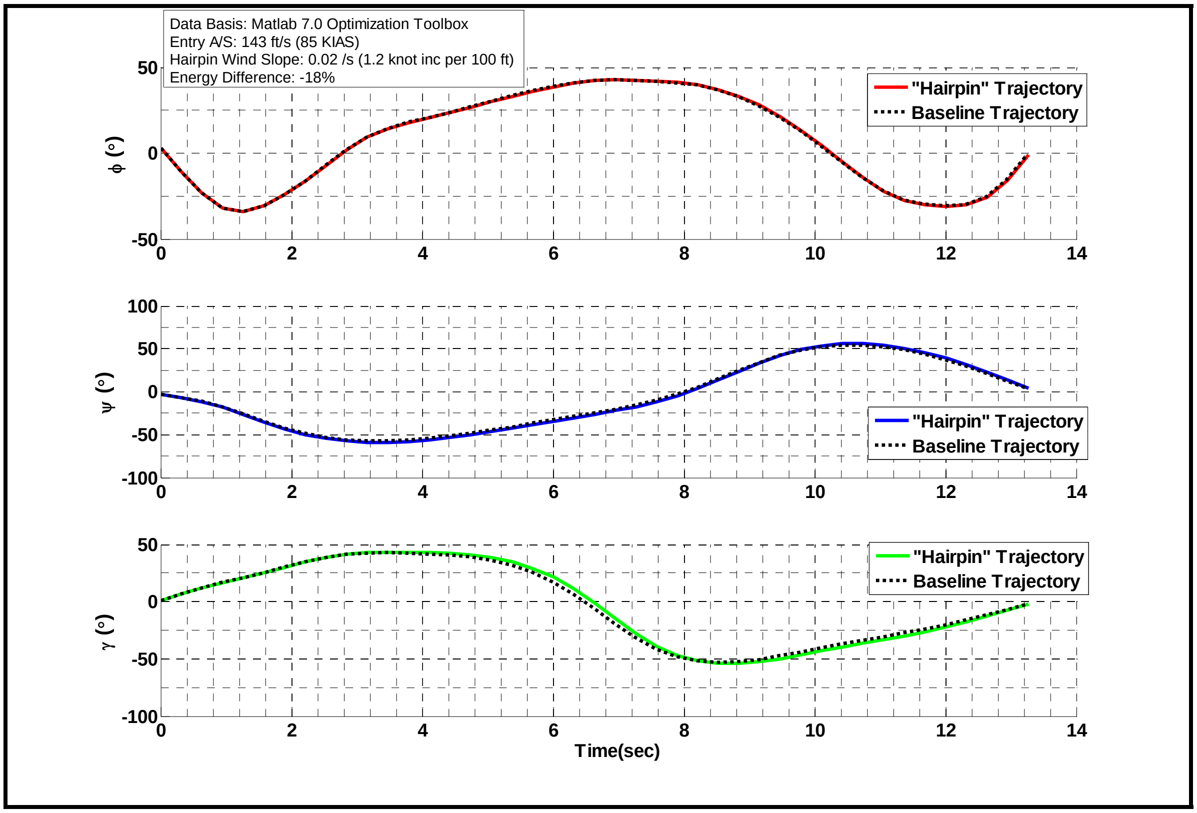

Figure 35. Euler Angle Comparison (0.02 ft/s / ft Wind Shear)

Figure 36 illustrates the aerodynamic performance of the sailplane while flying a hairpin dynamic soaring maneuver in 0.02 ft/s / ft wind shear conditions.

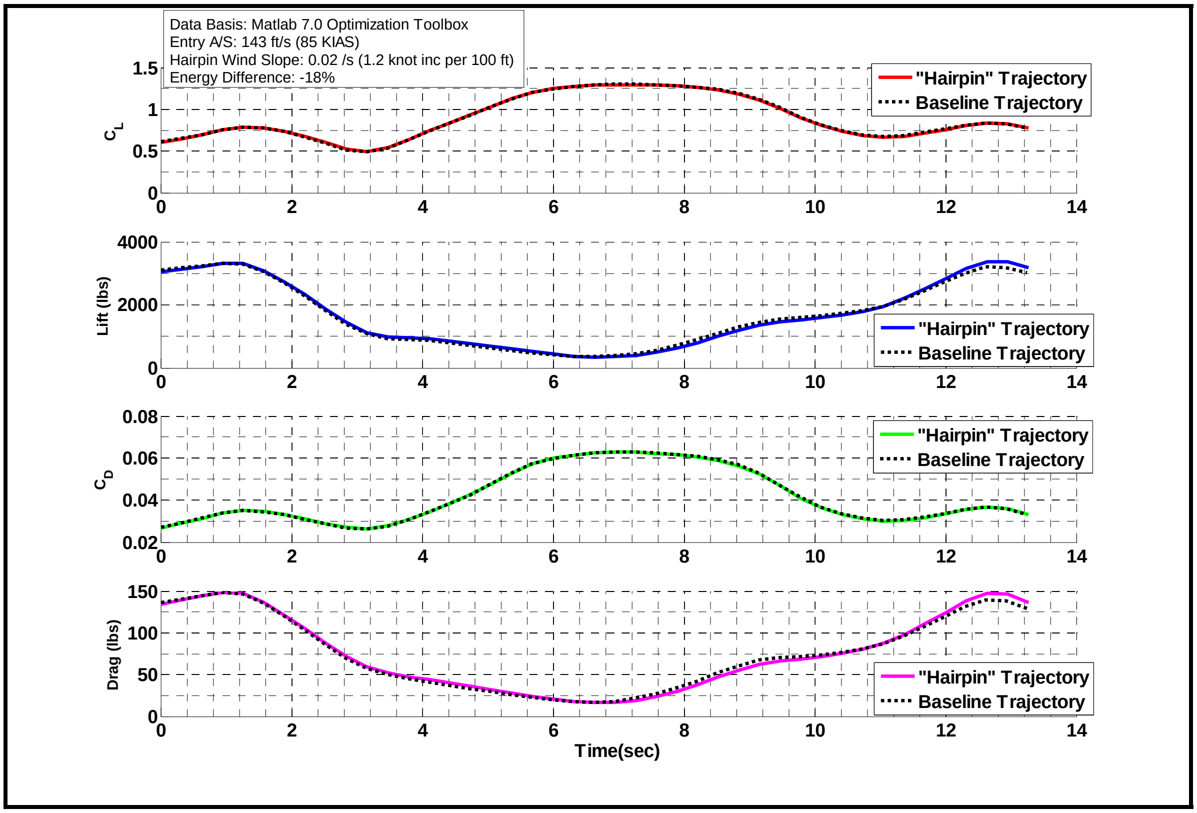

Figure 36. Aerodynamic Performance Comparison (0.02 ft/s / ft Wind Shear)

The $C_{L,}$ lift, C_D, and drag all remained nearly identical to the baseline data. Figure 37 summarizes the expected energy benefit of flying hairpins in both a 0.02 ft/s / ft and a 0.04 ft/s / ft wind shear as compared to the baseline.

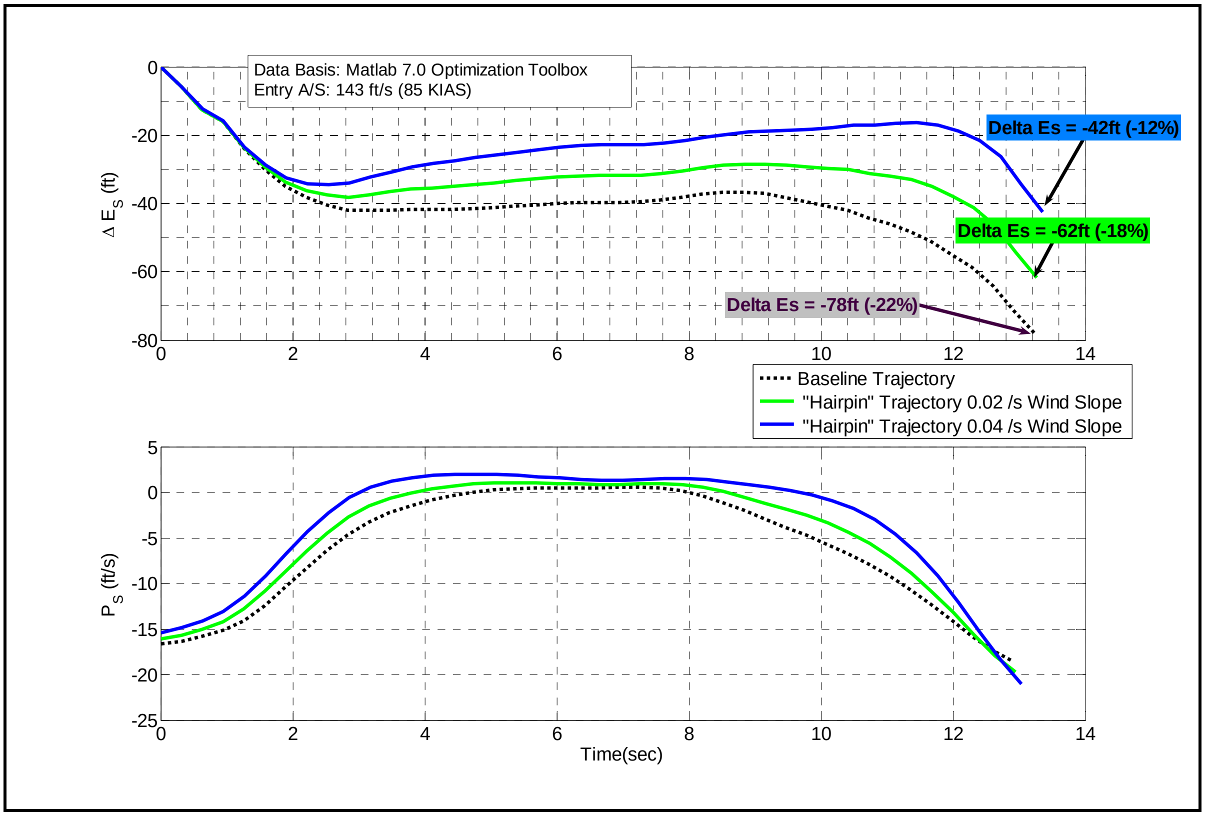

Figure 37. Summary Hairpin Energy State Performance Comparison

Flying a hairpin profile in a 0.02 ft/s / ft wind shear represented an E_s improvement of 16 ft from the baseline. However, a hairpin performed in a 0.02 ft/s /ft wind shear still resulted in a final E_s 20 ft worse than a hairpin performed in a 0.04 ft/s / ft. These trends were due to the P_s benefit from the wind shear described earlier. Even though the 0.02 ft/s / ft wind shear was fairly light, the effect was still strong enough to show the benefits of flying a hairpin maneuver in wind shear conditions. To illustrate this point further, the anti-hairpin maneuver was again modeled in order to build a comparison between the two profiles performed in the same wind shear conditions.

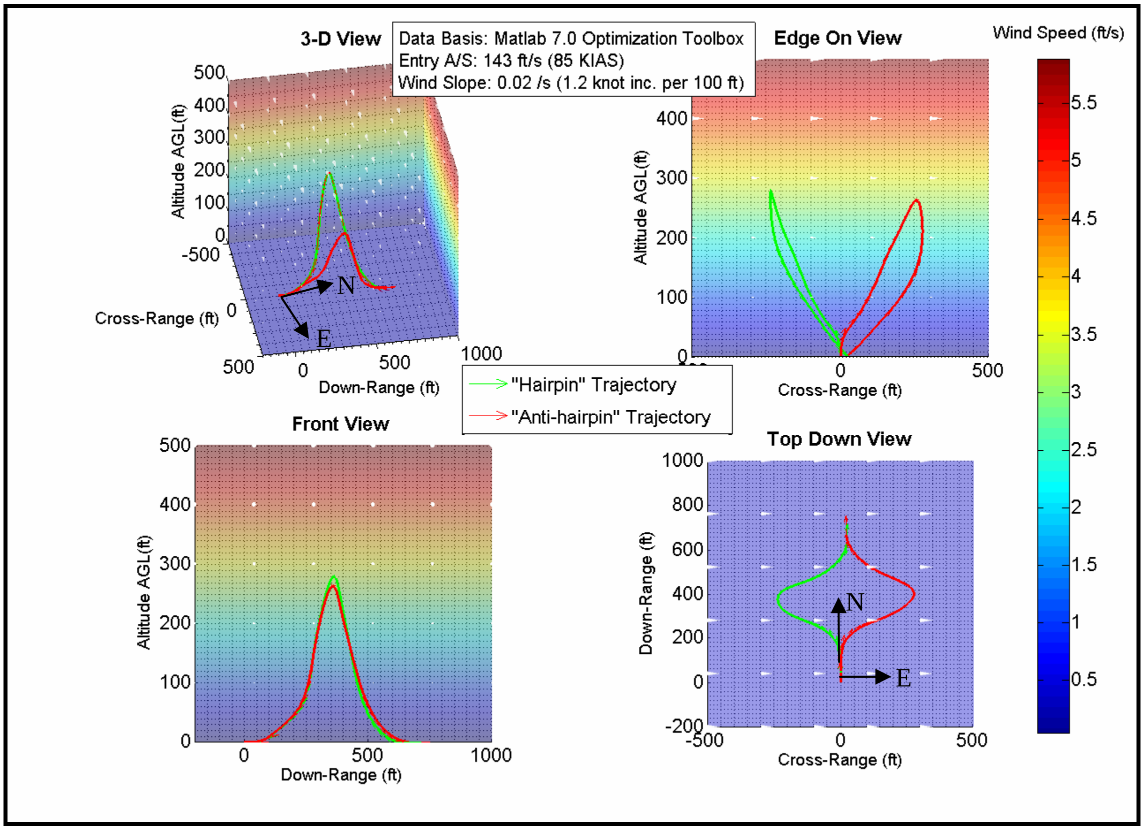

Figure 38. Hairpin vs. Anti-hairpin 4-View Trajectory Comparison (0.02 ft/s / ft Wind Shear)

Similar to the 0.04 ft/s / ft wind shear scenario, the hairpin and the anti-hairpin maneuvers were virtual mirror images of each other. The slight differences in shape were due to the wind effects on the profiles described earlier. However, since the wind shear in this case was weaker, these effects were not as pronounced. Figure 39 provides more detail on the shape of these profiles.

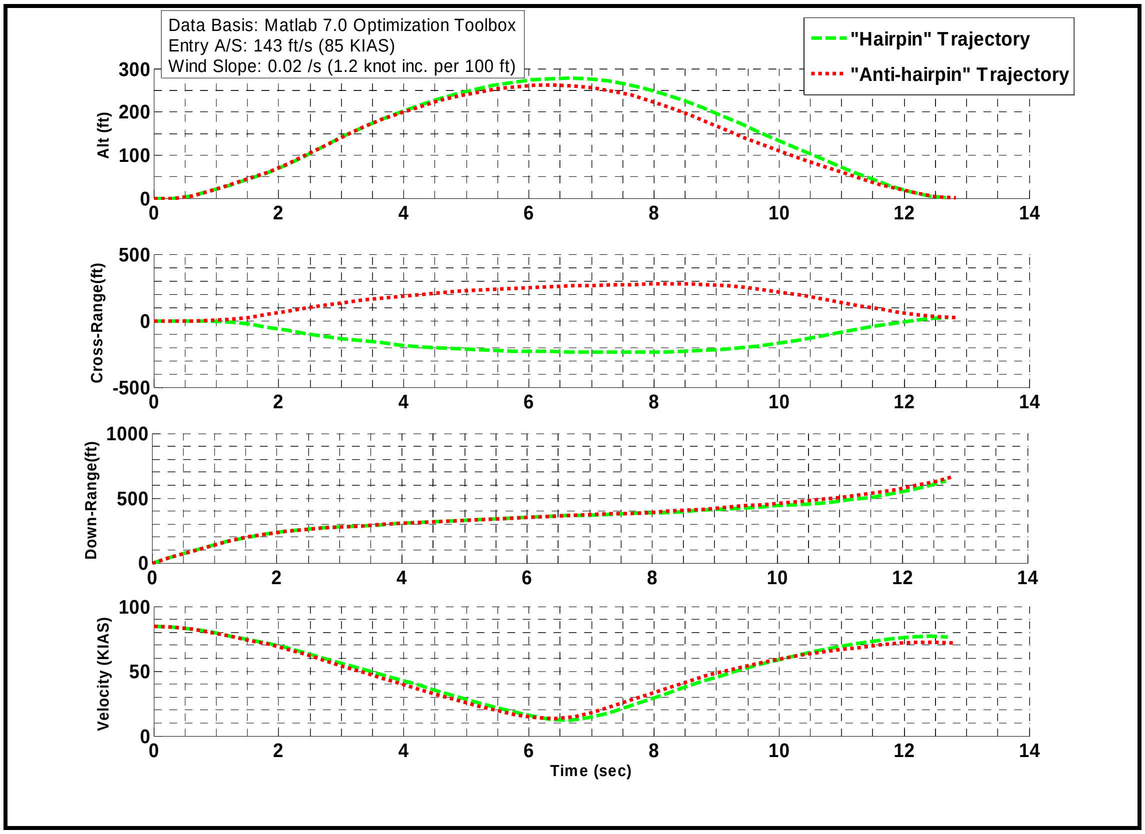

Figure 39. Hairpin vs. Anti-hairpin Trajectory Comparison (0.02 ft/s / ft Wind Shear)

The similarity in the trajectories of both the hairpin and anti-hairpin maneuvers is shown in Figure 39. Because of this similar performance, the control inputs required to perform either maneuver, with the exception of the turn direction, were also virtually identical. This is shown in Figure 40.

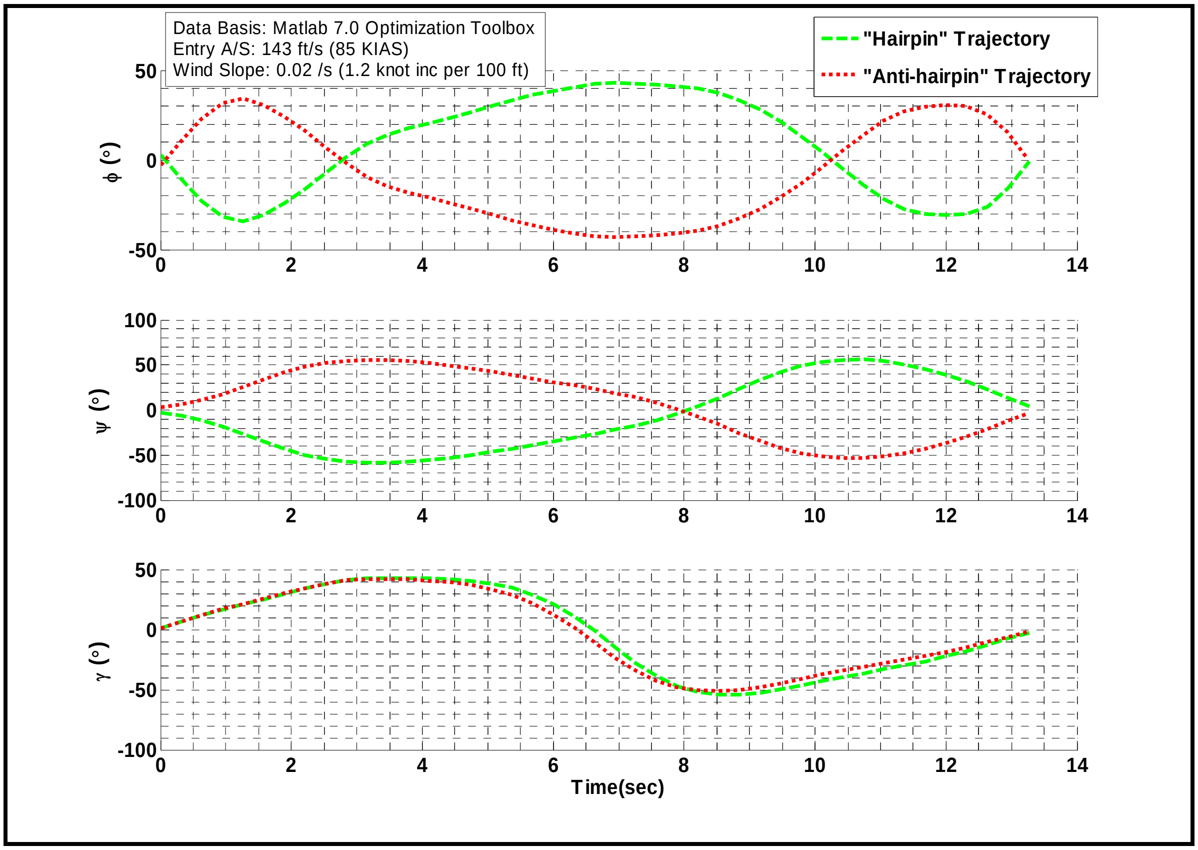

Figure 40. Hairpin vs. Anti-hairpin Euler Angle Comparison (0.02 ft/s / ft Wind Shear)

Because of the similarities in Euler angles and trajectories, the aerodynamic performance of the sailplane while performing a hairpin or anti-hairpin maneuver in this wind shear was also identical. This is shown in Figure 41.

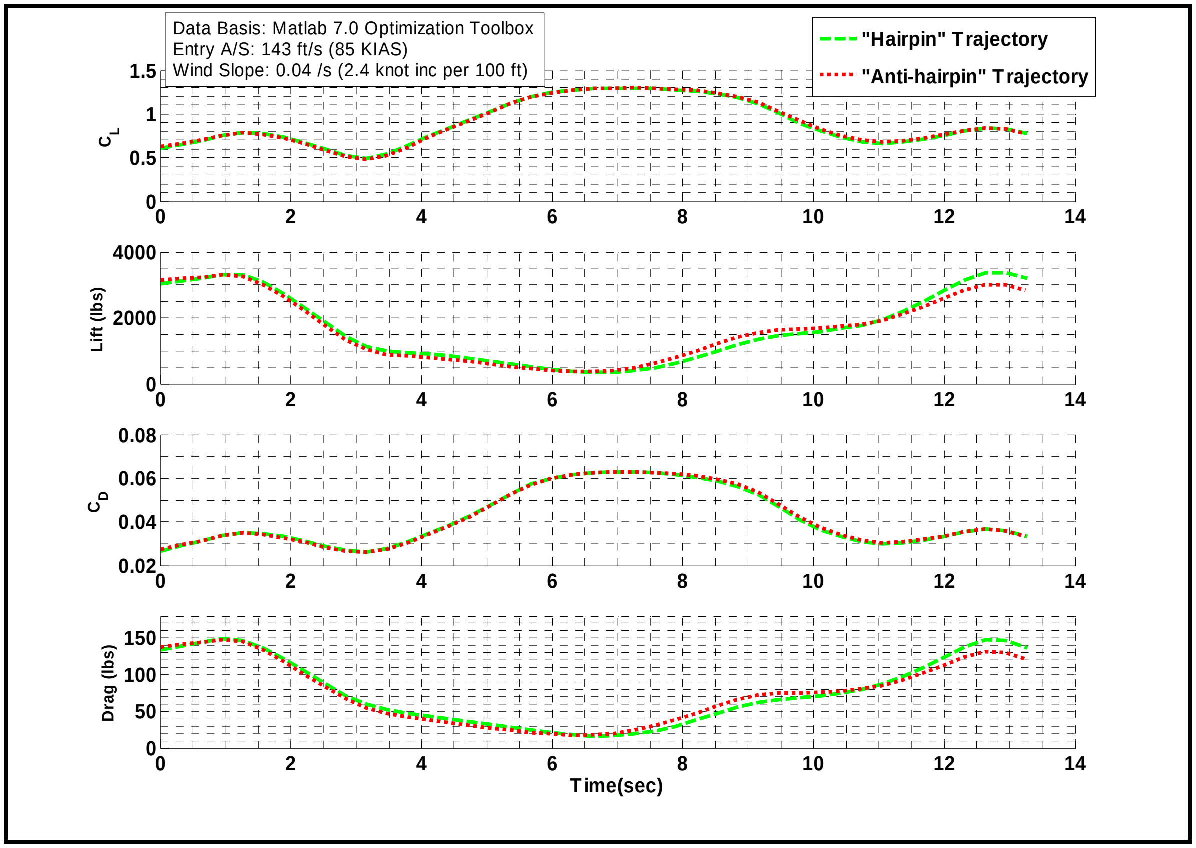

Figure 41. Hairpin vs. Anti-hairpin Aerodynamic Performance (0.02 ft/s / ft Wind Shear)

While the trajectories were similar, the energy state performance of the maneuvers were, again, very different from one another due to the wind shear effects. This is shown in Figure 42.

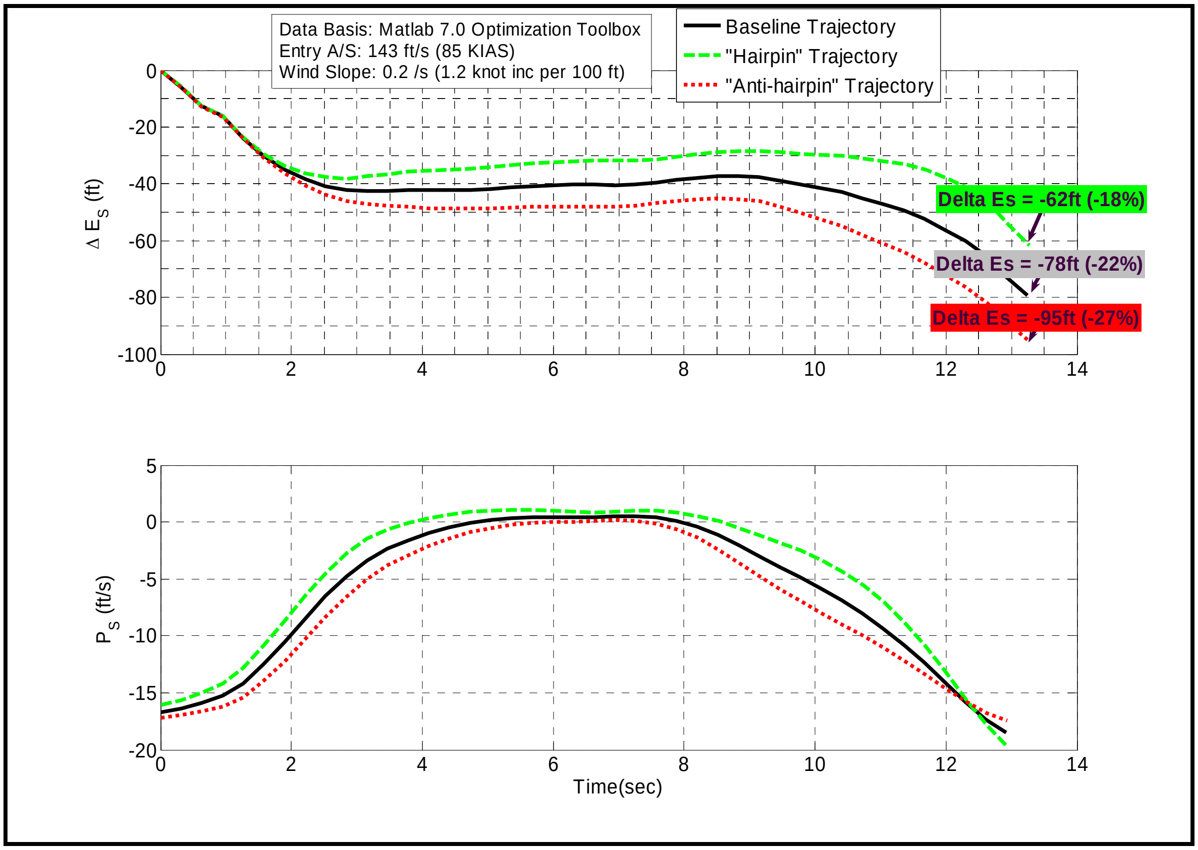

Figure 42. Hairpin/Baseline/Anti-hairpin Energy State Performance (0.02 ft/s / ft Wind Shear)

The anti-hairpin maneuver lost 95 specific energy height feet, or 27% of its E_s while the hairpin only lost 62 specific energy height feet, or only 18% of its initial energy height. Just as when the wind shear was 0.04 ft/s / ft, the hairpin maneuver in this wind shear condition outperformed the baseline trajectory in no wind shear and significantly outperformed the anti-hairpin maneuver.

Based on the analysis performed above, a summary of the energy penalty of anti-hairpin maneuvers when compared to the baseline trajectory was developed and is shown in Figure 43.

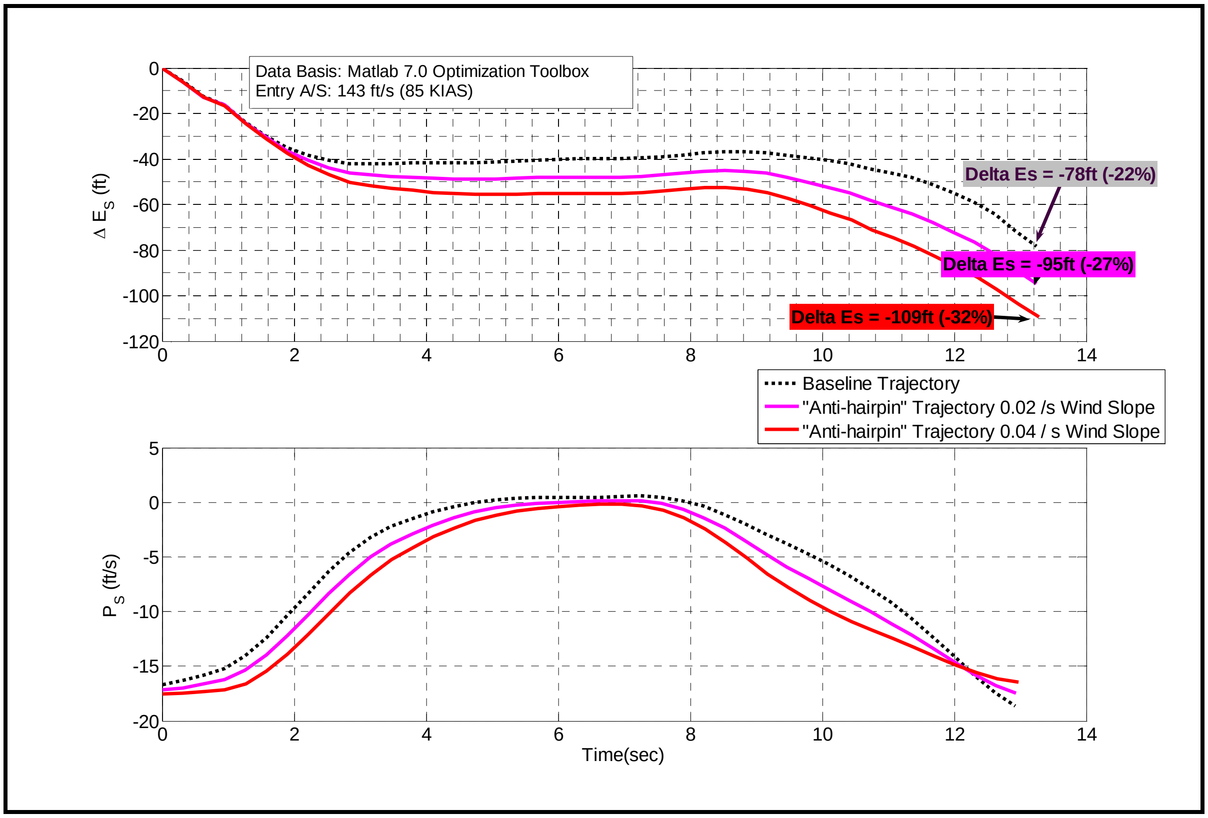

Figure 43. Summary Anti-hairpin Energy State Performance Comparison

Anti-hairpin maneuvers performed in stronger wind shears result in worse energy penalties just as hairpins performed in stronger wind shears result in increased energy benefit. This was expected and reasonable according to dynamic soaring theory.

Hence, a detailed analysis of these three wind shear profiles and the hairpin vs. anti-hairpin maneuvers revealed another important conclusion of dynamic soaring: So long as the entry speed into the maneuver was set beforehand, the control inputs and resulting shape of the optimal dynamic soaring profile were relatively unaffected by the strength of the wind shear. Furthermore, once the shape of the hairpin dynamic soaring profile was known, the anti-hairpin trajectory was its mirror image with respect to the prevailing wind shear direction. This is a very significant finding, especially for the dynamic soaring flight test portion of this research, since it meant that the maneuvers should be repeatable, predictable and therefore trainable to soaring pilots and programmable to NASA airborne robotic explorers given that an appropriate entry speed had been selected. In addition, once in the profile, the greatest exchange of energy with the wind shear occurred while the sailplane was climbing or descending through the wind shear layers. The energy exchanged by the turn reversal at the peak of the maneuver was negligible in comparison. Essentially, this rule instructs aircraft to reverse turn directions as smoothly and quickly as possible once the peak of the dynamic soaring maneuver is achieved.

Since the strength of the wind shear had a negligible effect on the optimal profile, a study was conducted on the effects of entry speed on dynamic soaring. Ultimately, the goal of this portion of the research was to discover the best entry speed to ensure the success of energy gain from dynamic soaring. The same objective function and the same wind shear of 0.02 ft/s / ft were used to ensure equal conditions for all dynamic optimization trials and to ensure the results were representative of typical wind shear conditions expected at Edwards AFB. The results are presented below and offer a new perspective on dynamic soaring flight.

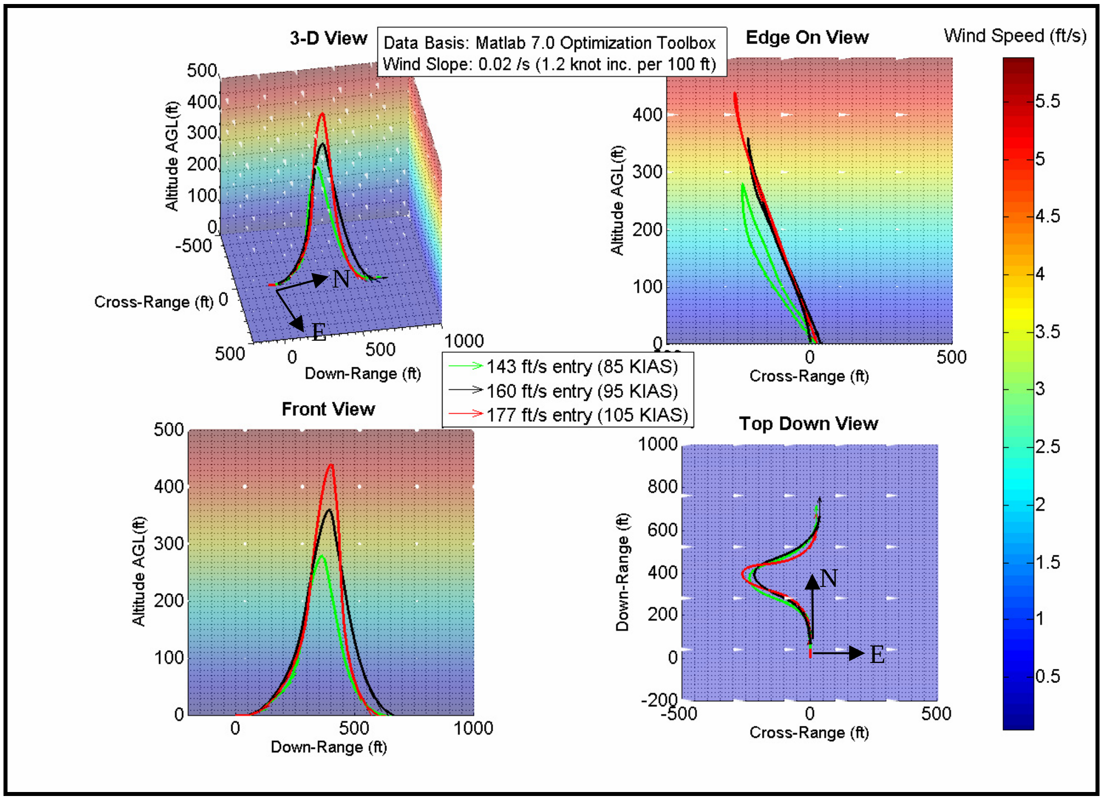

Figure 44. Entry Airspeed Hairpin Trajectory Comparison (0.02 ft/s / ft Wind Shear)

Figure 44 depicts three different optimal dynamic soaring profiles in 0.02ft/s/ft wind shear condition. These profiles differ only in the selected entry airspeed. The red curve represents the fastest entry speed of 177 ft/s or 105 KIAS. The black curve represents an entry speed of 160 ft/s, or 95 KIAS, and the green curve represents the slowest entry speed of 143 ft/s, or 85 KIAS.

These profiles show something that may be initially counter-intuitive: Faster entry speeds result in approximately the same downrange distance as slower entry speeds. This is due to the dynamic soaring conclusion described earlier which stated that the most energy is gained from the climb into the headwind or the descent away from the tailwind. A sailplane with more initial airspeed has the ability to climb higher into the wind shear than a sailplane with less initial airspeed. In essence, the sailplane is “reaching through the shear” in order to extract as much energy as possible. This climb and descent for energy, however, is at the expense of potential downrange distance. This is further illustrated in Figure 45.

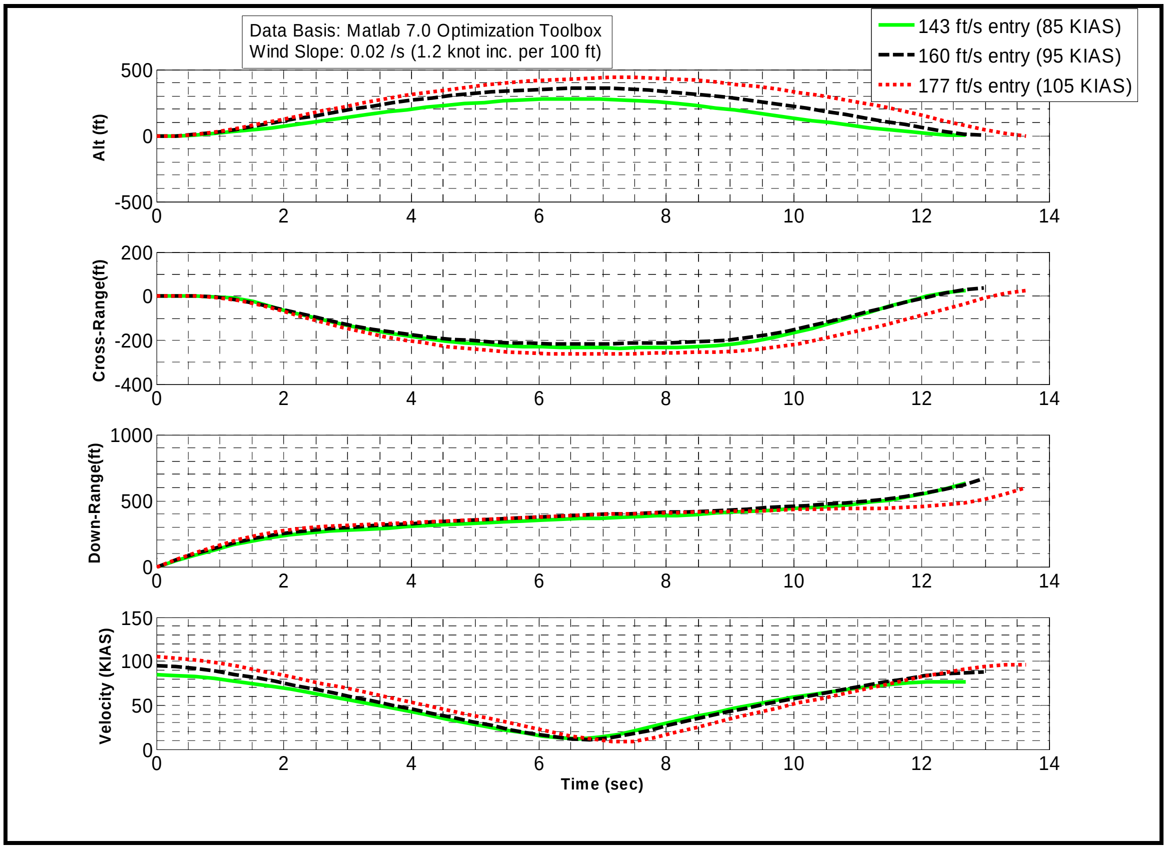

Figure 45. Entry Airspeed Trajectory Comparison (0.02 ft/s / ft Wind Shear)

As detailed in Figure 45, the only significant impact of higher entry speeds was increased altitude gain, and longer trajectory times. Euler angles during the maneuvers were also very similar to each other and are illustrated in Figure 46.

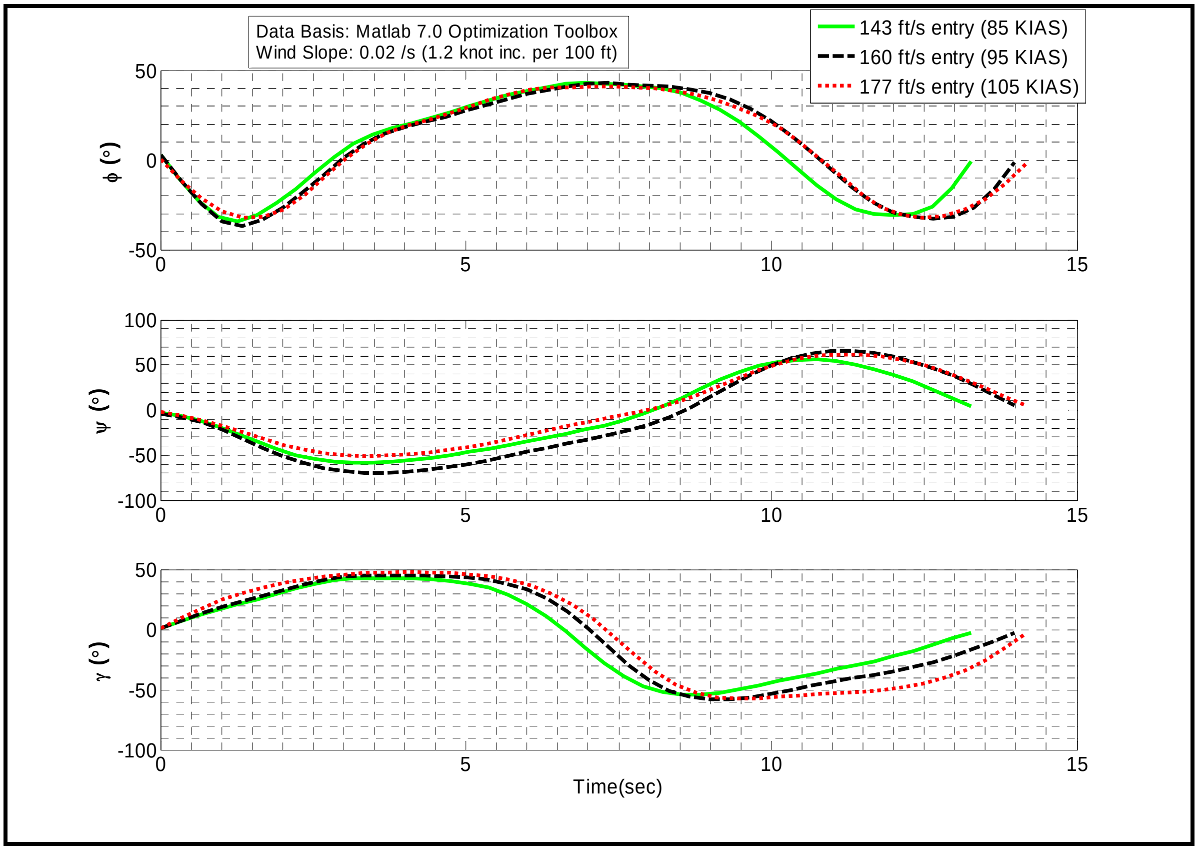

Figure 46. Entry Airspeed Euler Angle Comparison (0.02 ft/s / ft Wind Shear)

Figure 46 details the fact that the magnitudes of the sailplane's Euler angles remained virtually identical across the entry speeds, but the duration of those inputs varied in order to achieve their respective trajectory shapes. For instance, the 177 ft/s entry speed *(red dotted line)* was able to maintain a positive γ of 50° longer than the other entry speeds due to its higher initial entry energy conditions. This resulted in the 177 ft/s entry speed achieving the highest altitude gain through the wind shear of all the entry speeds. Figure 47 illustrates the aerodynamic performance of the sailplane across the various entry speeds.

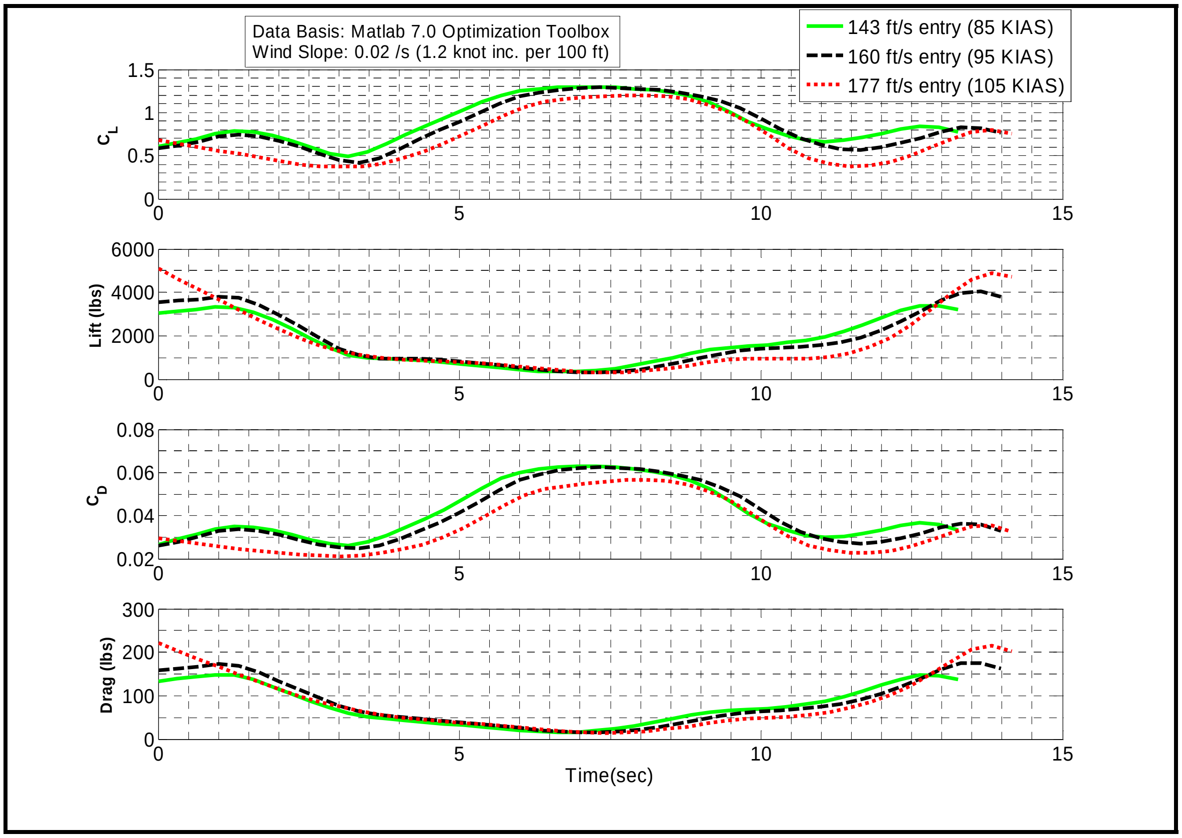

Figure 47. Entry Airspeed Aerodynamic Performance Comparison (0.02 ft/s / ft Wind Shear)

Figure 47 shows that the relative magnitude of lift and drag forces acting on the sailplane were nearly identical despite the differences in entry airspeed. This is primarily due to the interplay between the coefficients of lift and drag and dynamic pressure. For example, slower speeds commanded higher coefficients of drag and lift in order to execute the maneuver, but because of the lower dynamic pressure at these speeds, the resulting forces were very similar to the higher speeds. The higher entry speeds, however, did suffer from higher parasite drag on the sailplane at the beginning of the maneuver and higher induced drag generated during the dive recovery at the end of the maneuver. This higher drag had a negative impact on the sailplane's dynamic soaring performance since it mitigated much of the energy gained by transiting through the wind shear. Higher entry speeds also increased the risk of an over-*g* due to excessive maneuvering. Based on this information, an apparent tradeoff existed between using a higher entry speed to penetrate through the wind shear vice the penalty of increased drag and over-*g* potential. This is illustrated in Figure 48.

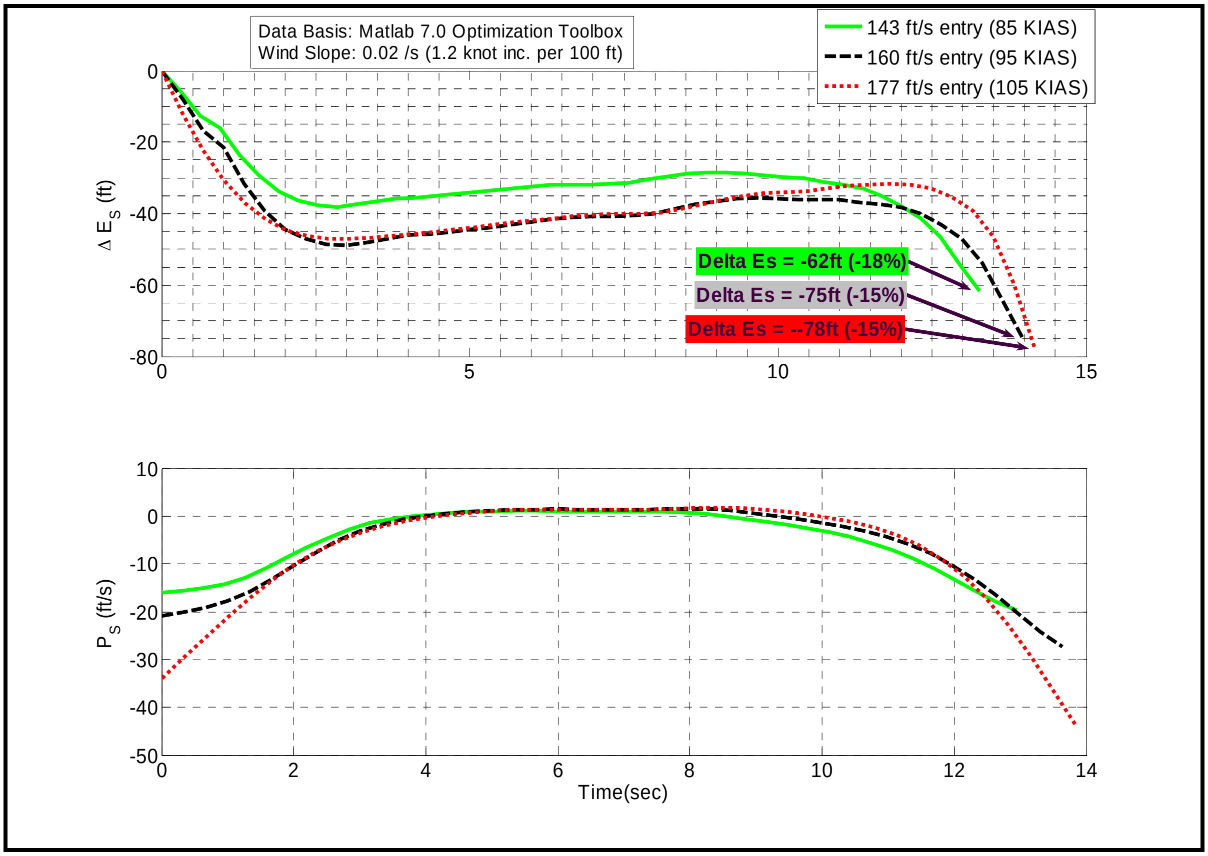

Figure 48. Entry Airspeed Energy State Performance Comparison (0.02 ft/s / ft Wind Shear)

The most significant finding of Figure 48 was that neither entry speed performed significantly better than the others with respect to the percentage of energy lost. This demonstrated the interplay between using higher entry speeds to penetrate higher into the wind shear at the potential expense of losing too much of that energy to the higher drag incurred because of high speeds. For example, even though the 177 ft/s entry speed extracted the most energy from the wind, it also lost much of that energy to parasite drag in the beginning of the profile and induced drag during the dive recovery at the end of the maneuver. The result was the same final energy state as the slower speeds with respect to the percentage of energy lost.

This entry speed analysis revealed two more useful conclusions about dynamic soaring. Higher speeds increase the potential energy gaining performance of the sailplane from the wind shear, but at the expense of increased parasite and induced drag, the increased risk of an over-*g*, and at the expense of downrange distance. Additionally, for the L-23 Super Blanik, entering the dynamic soaring profile at approximately 95 KIAS represents a good compromise between net energy benefit, operational limitations of the aircraft, and downrange distance achieved. One final study needed to be conducted in order to understand the relationship between entry speed and the strength of the wind shear. Figure 49 in this analysis depicts the minimum wind shear required in order to fly an energy neutral dynamic soaring profile.

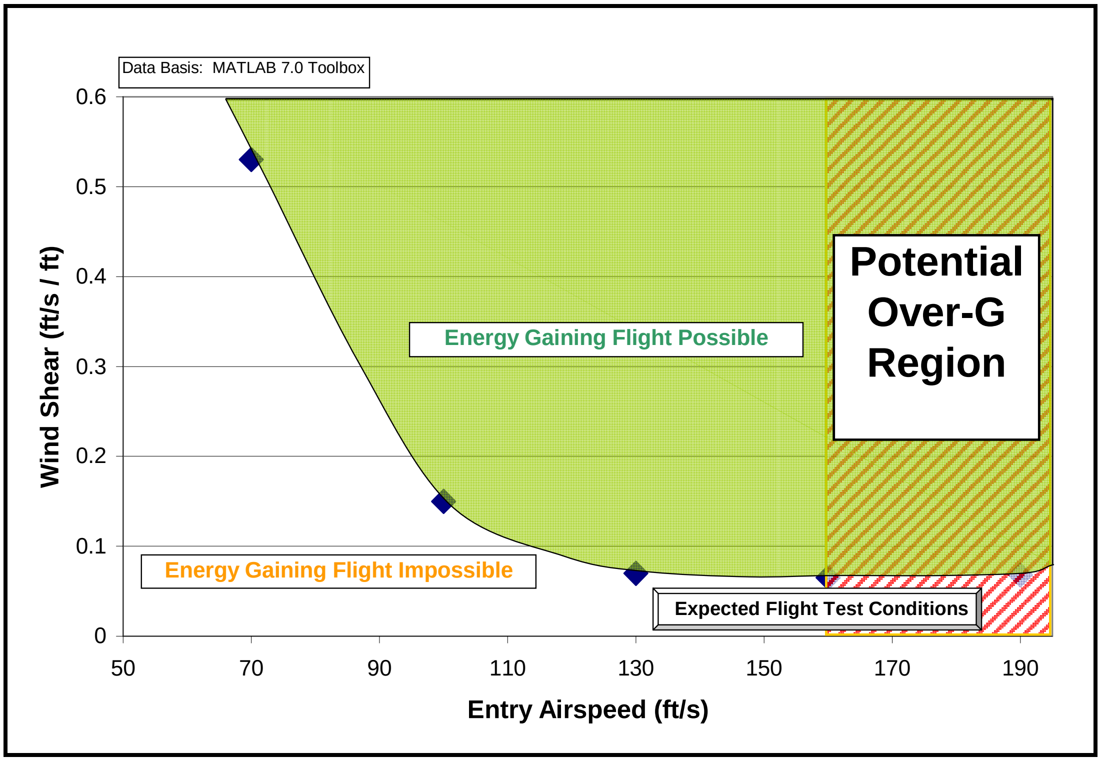

Figure 49. Minimum Wind Shear for Energy Neutral Profiles

If wind shears were above the plotted data, an energy gaining profile could be flown, while if wind shears were below the data, only an energy losing profile could be flown. The airspeed band spans the range of the sailplane capability from stall through the never exceed speed of the aircraft and the airspeed data point were selected to be spaced at 30 ft/s intervals in order to provide sufficient data for analysis. The data points for Figure 49 were generated by using the same optimization problem formulation described earlier, with the exception of a new objective function equation shown below.

$$\mu_f(N) = \left[h(N) + \frac{V_t(N)^2}{2g} \right] - \left[h(1) + \frac{V_t(1)^2}{2g} \right] \tag{38}$$

This objective function was designed to minimize the difference between the beginning E_s and the final *Es*. The strength of the wind shear was manually varied until an optimal solution converged.

Figure 49 also shows a dynamic soaring valley existed above 120 ft/s, in which the wind shear required for an energy neutral profile varied little with airspeed. At this speed and above, wind shears on the order of 0.06 ft/s / ft to 0.08 ft/s / ft were required for energy neutral flights. Even though these wind shears are considered fairly strong, these wind shears are capable of occasionally being reproduced in nature by unusually strong temperature inversions, boundary layer effects in strong winds, or orthographic effects on the leeward side of mountain ridges. As the entry speed decreases below 120 ft/s / ft, increasingly unrealistic wind shears were required for the same energy neutral flights. For instance, an entry speed of 70 ft/s required a wind shear of 0.53 ft/s / ft. This is an increase of 53 ft/s, or 31 knots, per 100 ft gain in altitude. This wind shear is equivalent to winds experienced in a Category I hurricane. However, at very high airspeeds above 160 ft/s, the sailplane is required to over-*g* the airframe in order to fly the optimal profile. Modifications to the flight profile would have to be made in order to avoid over stressing the airframe through aggressive maneuvering. This final analysis led to another important dynamic soaring conclusion: On the scale of full sized sailplanes, dynamic soaring requires strong wind shears and is best achieved by using moderate to fast entry airspeeds with smooth control inputs to avoid an over-*g*.

III. Pilot-in-the-Loop Simulator Trials

Aircraft Equations of Motion Development

By observing the results of the point mass analysis, great precision would be required in order to fly the dynamic soaring maneuver correctly. Heading, airspeed, altitude, and bank angles all changed rapidly over the course of only several seconds. Without a means with which to practice the maneuver in a benign environment, precious time, data, and program funds could be potentially wasted in actual flight test. Commercially available sailplane simulators were woefully inadequate for this task due to their lack of engineering quality data output and a faithful aeronautical model representation of an L-23 Super Blanik sailplane. Furthermore, due to the relatively unexplored practice of dynamic soaring with full sized sailplanes, all commercially available software was specifically designed to only simulate static soaring environments, not dynamic soaring conditions. This realization prompted the next step of this research project: The development of a high fidelity L-23 Super Blanik simulator. This simulator would be capable of allowing the flight crew to study various dynamic soaring maneuvers, to develop the dynamic soaring flight test techniques (DS FTT) / crew coordination procedures, and to evaluate custom built dynamic soaring electronic avionics displays. This process was broken down into three distinct build up phases. The first phase involved developing and verifying high fidelity aircraft equation of motion using MATLAB® simulations. Phase two involved building a prototype flight simulator in the Air Force Research Laboratory’s Aerospace Vehicles Technology Assessment and Simulation Branch (AFRL/VACD) Large Amplitude Multi-Mode Aerospace Research Simulator (LAMARS) facility located at Wright

Patterson AFB, OH. LAMARS would be used to evaluate the ease and feasibility of implementing these equations of motion for dynamic soaring research using advanced flight simulators developed specifically for dynamic soaring.

The lessons learned from phase two would then be used to develop a full capability research flight simulator at the NASA Dryden Flight Research facility at Edwards AFB California. This NASA simulator would be designed to meet all the objectives of the flight simulator portion of this research.

Phase one began by developing the appropriate aircraft equations of motion. Point mass equations of motion may have been sufficient for trajectory development, but by their very nature, lacked any information on moments of inertia, aerodynamic moments, control surface deflections, stability coefficients, and angular rates. This made them inappropriate for a high fidelity aircraft simulator. A set of equations was needed that described an aircraft’s motion in 6-DOF. This could only be accomplished by using the set of twelve aircraft equations of motion. For the highest fidelity, these equations must be subject to non-linear forces and moments, and also must include the effects of wind shears. The performance of these equations would be governed in large part by the effects of stability coefficients and moments of inertia. This required a valid aeronautical model of the L-23 Super Blanik sailplane.

Since this aeronautical model did not exist at the start of this research, another Test Management Project was initiated by the USAF TPS during the fall of 2005. Using the same L-23 sailplane the SENIOR IDS (Borror, 2004) test team used in 2004 to research the lift and drag characteristics of the aircraft, the HAVE BLADDER (Aviv, 2005) test team conducted a test program in order to produce accurate moment of inertia data and stability coefficient information for the test L-23. These results are summarized in the tables shown below.

Table 1. Longitudinal Stability Coefficients

Pitch Moment		lift Force		drag Force	
Coefficient	Value	Coefficient	Value	Coefficient	Value
C_{M_α}	-0.014	$C_{l_{\delta e}}$	0.342	C_{D_0}	0.0007
C_{M_Q}	-25	C_{l_α}	9.16	C_{D_α}	1.145
$C_{M_{\dot\alpha}}$	-5.2	C_{l_0}	0.5	$C_{D_{\delta E}}$	0.0
C_{M_0}	-0.0171α+0.0986				
$C_{M_{\delta E}}$	-0.025				

Where:

C_{M_α} = Pitch Moment [M] Coefficient due to Angle of Attack (/rad)
C_{M_Q} = Pitch Moment Coefficient due to Body Fixed Pitch Rate [Q] (/rad)
$C_{M_{\dot\alpha}}$ = Pitch Moment Coefficient due to Angle of Attack Rate [$\dot\alpha$] (/rad)
C_{M_0} = Pitch Moment Coefficient at Zero Angle of Attack (/rad)
$C_{M_{\delta E}}$ = Pitch Moment Coefficient due to Elevator Deflection [δ_E] (/rad)
$C_{l_{\delta e}}$ = lift [l] Coefficient due to Elevator Deflection (/rad)
C_{l_α} = lift Coefficient due to Angle of Attack (/rad)
C_{l_0} = lift Coefficient at Zero Angle of Attack (/rad)
C_{D_0} = drag Coefficient at Zero Angle of Attack (/rad)
C_{D_α} = drag Coefficient due to Angle of Attack (/rad)
$C_{D_{\delta E}}$ = drag Coefficient due to Elevator Deflection (/rad)

Table 2. Lateral Directional Stability Coefficients

Side Force		Roll Moment		Yaw Moment	
Coefficient	Value	Coefficient	Value	Coefficient	Value
C_{Y_β}	-0.006	C_{L_β}	-0.001	C_{N_β}	0.001
$C_{Y_{\delta A}}$	0.001	C_{L_P}	-0.7	C_{N_P}	-0.0157α -0.0689
$C_{Y_{\delta R}}$	0.0028	C_{L_R}	0.0265α+0.1667	C_{N_R}	-0.04
C_{Y_0}	0.0	$C_{L_{\delta A}}$	0.006	$C_{N_{\delta A}}$	0.0
		$C_{L_{\delta R}}$	0.0003	$C_{N_{\delta R}}$	-0.009
		C_{L_0}	0.0	C_{N_0}	0.0005

Where:

C_{Y_β} = Side Force [*Y*] Coefficient due to Sideslip [β] (/rad)
$C_{Y_{\delta A}}$ = Side Force Coefficient due to Aileron Deflection [δ_A] (/rad)
$C_{Y_{\delta R}}$ = Side Force Coefficient due to Rudder Deflection [δ_R] (/rad)
C_{Y_0} = Side Force Coefficient at Zero Angle of Attack (/rad)
C_{L_β} = Roll Moment Coefficient [*L*] due to Sideslip (/rad)
C_{L_P} = Roll Moment Coefficient due to Roll Rate [*P*] (/rad)
C_{L_R} = Roll Moment Coefficient due to Yaw Rate [*R*] (/rad)
$C_{L_{\delta A}}$ = Roll Moment Coefficient due to Aileron Deflection (/rad)
$C_{L_{\delta R}}$ = Roll Moment Coefficient due to Rudder Deflection (/rad)
C_{L_0} = Roll Moment Coefficient at Zero Angle of Attack (/rad)

Continued from Table 2

C_{N_β} = Yaw Moment [*N*] Coefficient due to Sideslip (/rad)
C_{N_P} = Yaw Moment Coefficient due to Roll Rate (/rad)
C_{N_R} = Yaw Moment Coefficient due to Yaw Rate [*R*] (/rad)
$C_{N_{\delta A}}$ = Yaw Moment Coefficient due to Aileron Deflection (/rad)
$C_{N_{\delta R}}$ = Yaw Moment Coefficient due to Rudder Deflection (/rad)
C_{N_0} = Yaw Moment Coefficient at Zero Angle of Attack (/rad)

Table 3. Moments of Inertia

(1124 lbs Gross Weight)	
Moment of Inertia	**Value (slug-ft^2)**
I_x	**2080**
I_y	**1010**
I_z	**2700**
I_{xz}	**190**

Table 4. Control Surface Deflection Limits

Control Surface	Limit (°)
Elevator	**32° up** **25° down**
Aileron	**34° up** **13° down**
Rudder	**±30°**

With this aero model data, the construction of non-linear, rigid body, constant mass, aircraft equations of motion could begin. The first step was to determine how winds would affect these equations. The following figures are provided to show the development of the relationships within and between reference frames used in the subsequent aircraft equations of motion.

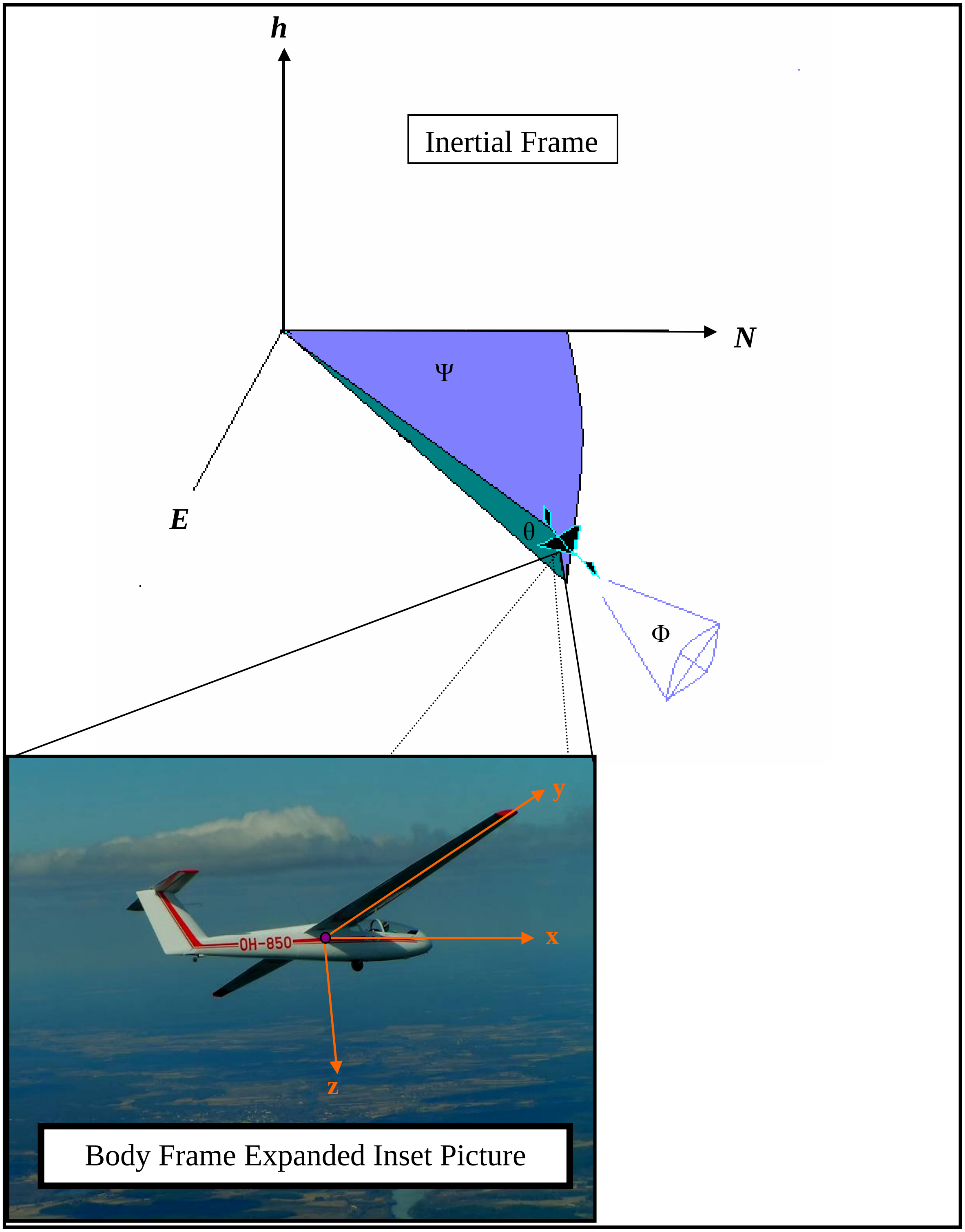

Figure 50. Reference Frame Relationships

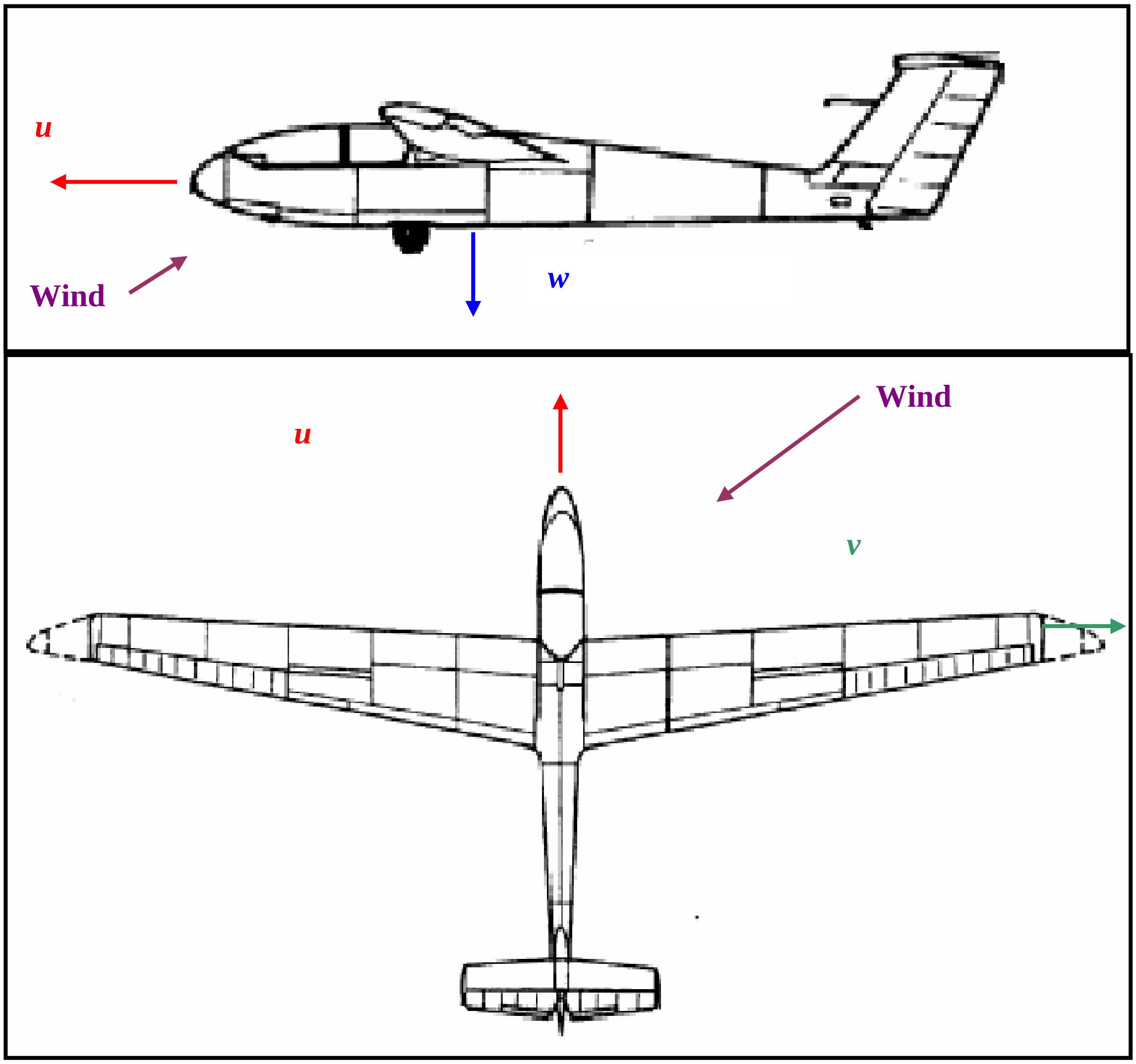

Figure 51. Winds in the Body Fixed Reference Frame

Winds had the ability to influence only the effective angle of attack, sideslip angle, and the true airspeed experienced by the aircraft. For instance, if the sailplane flew 50 knots into a 50 knot headwind, the effective true airspeed experienced by the aircraft would be the same as if the sailplane were flying at 100 knots in zero wind conditions. Furthermore, if the aircraft experienced an updraft, the effective angle of attack of the sailplane would increase.

A front quartering headwind from the right, as shown in Figure 51, would make the aircraft behave as if it were experiencing a positive sideslip. These relationships are illustrated in the equations shown below.

$$\alpha = ATAN\left(\frac{w + w_{WIND}}{u + u_{WIND}}\right) \tag{39}$$

$$\beta = ASIN\left(\frac{v + v_{WIND}}{V_t}\right) \tag{40}$$

$$V_t = \sqrt{(u + u_{WIND})^2 + (v + v_{WIND})^2 + (w + w_{WIND})^2} \tag{41}$$

Where:

u = Component of aircraft velocity along the body fixed x-axis (ft/s)
u_{WIND} = Component of wind velocity along body fixed x-axis (ft/s)
v = Component of aircraft velocity along the body fixed y-axis (ft/s)
v_{WIND} = Component of wind velocity along body fixed y-axis (ft/s)
w = Component of aircraft velocity along the body fixed z-axis (ft/s)
w_{WIND} = Component of wind velocity along body fixed z-axis (ft/s)
V_t = True airspeed of aircraft (ft/s)

These angle and true airspeed relationships required that inertial frame winds were accurately modeled in a body fixed frame. This was accomplished by the following conversion matrix.

$$\begin{bmatrix} u_{WIND} \\ v_{WIND} \\ w_{WIND} \end{bmatrix} = \begin{bmatrix} C(\theta)C(\psi) & C(\theta)S(\psi) & -S(\theta) \\ -C(\phi)S(\psi) + S(\phi)S(\theta)C(\psi) & C(\phi)C(\psi) + S(\phi)S(\theta)S(\psi) & S(\phi)C(\theta) \\ S(\phi)S(\psi) + C(\phi)S(\theta)C(\psi) & -S(\phi)C(\psi) + C(\phi)S(\theta)S(\psi) & C(\phi)C(\theta) \end{bmatrix} \begin{bmatrix} -Wind_E \\ -Wind_N \\ Wind_h \end{bmatrix} \tag{42}$$

Where:

C = Cosine
S = Sine
$Wind_E$ = Component of wind along *E*-axis inertial frame (ft/s)
$Wind_N$ = Component of wind along *N*-axis inertial frame (ft/s)
$Wind_h$ = Component of wind along *h*-axis inertial frame (ft/s)

Unlike in the point mass model, all body fixed velocities became significant when using the full 6-DOF aircraft equations of motion set. This set of equations is defined below.

$$\dot{u} = Rv - Qw - g\sin(\theta) + \frac{F_X}{m} \tag{43}$$

$$\dot{v} = -Ru + Pw + g\sin(\phi)\cos(\theta) + \frac{F_Y}{m} \tag{44}$$

$$\dot{w} = Qu - Pv + g\cos(\phi)\cos(\theta) + \frac{F_Z}{m} \tag{45}$$

Where:

F_x	=	Sum of forces in body fixed x-axis direction (lb_f)
F_y	=	Sum of forces in body fixed y-axis direction (lb_f)
F_z	=	Sum of forces in body fixed z-axis direction (lb_f)
θ	=	Euler Pitch Angle (deg)

The forces in the above equations were determined by the following set of equations.

$$F_X = -D\cos(\alpha)\cos(\beta) - Y\cos(\alpha)\sin(\beta) + L\sin(\alpha) \tag{46}$$

$$F_Y = -D\sin(\beta) + Y\cos(\beta) \tag{47}$$

$$F_Z = -D\sin(\alpha)\cos(\beta) - Y\sin(\alpha)\sin(\beta) - L\cos(\alpha) \tag{48}$$

Where:

Y = Side Force (lb_f)

Lift and drag were determined by equation (7) and (8) respectively mentioned earlier in this Thesis. However, a new term, known as side force, was determined via the equation shown below.

$$Y = \frac{1}{2} \rho V_t^2 s C_Y \tag{49}$$

Where:

Y = Side Force (lb_f)

C_Y = Coefficient of Side Force

The coefficients of lift, drag, and side force in the above equations were determined by the following equations.

$$C_L = C_{L_\alpha} \alpha + C_{L_{\delta E}} Elev \tag{50}$$

$$C_D = (.0027 * C_l^2 + .017) + C_{D_{\delta E}} \, Elev \tag{51}$$

$$C_Y = C_{Y_\beta} \beta + C_{Y_{\delta R}} Rdr \tag{52}$$

Where:

$Elev$ = Elevator Deflection (rad)

Rdr = Rudder Deflection (rad)

The body fixed roll, yaw, and pitch angular rates were determined by the equations shown below.

$$\dot{P} = \frac{I_{XZ}[I_X - I_Y + I_Z]PQ - [I_Z(I_Z - I_Y) + I_{XZ}^2]QR + I_Z\bar{L} + I_{XZ}\bar{N}}{I_X I_Z - I_{XZ}^2} \tag{53}$$

$$\dot{Q} = \frac{(I_Z - I_X)PR - I_{XZ}(P^2 - R^2) + m}{I_Y(I_X I_Z - I_{XZ}^2)} \tag{54}$$

$$\dot{R} = \frac{[(I_X - I_Y)I_X + I_{XZ}^2]PQ - I_{XZ}[I_X - I_Y + I_Z]QR + I_{XZ}\bar{L} + I_X\bar{N}}{I_X I_Z - I_{XZ}^2} \tag{55}$$

The pitch, roll, and yaw moments were determined by equations (56) through (58).

$$\bar{L} = {}^{1}\!/_{2}\,\rho V_t^2 sbC_l \tag{56}$$

$$M = {}^{1}\!/_{2}\,\rho V_t^2 scC_M \tag{57}$$

$$\bar{N} = {}^{1}\!/_{2}\,\rho V_t^2 sbC_N \tag{58}$$

Where:

b = Wing Span (ft)
c = Wing Chord (ft)
C_l = Roll Moment Coefficient
C_M = Pitch Moment Coefficient
C_N = Yaw Moment Coefficient

The moment coefficients shown in the preceding equations were determined by using the equations below.

$$C_l = C_{L_\beta}\beta + C_{L_{\delta A}}Ail + C_{L_{\delta R}}Rdr + \frac{b}{2V_t}[C_{L_P}P + C_{L_R}R] \tag{59}$$

$$C_M = C_{M_\alpha}\alpha + C_{M_{\delta E}}Elev + \frac{\bar{c}}{2V_t}[C_{M_Q}Q + C_{M_{\dot{\alpha}}}\dot{\alpha}] \tag{60}$$

$$C_N = C_{N_\beta}\beta + C_{N_{\delta R}}Rdr + C_{N_{\delta A}}Ail + \frac{b}{2V_t}[C_{N_P}P + C_{N_{\delta R}}Rdr] \tag{61}$$

Where:

Ail = Aileron Deflection (rad)

Euler angles were computed by using equations (62) though (64) shown below.

$$\dot{\theta} = Q\cos(\phi) - R\sin(\phi) \tag{62}$$

$$\dot{\phi} = P + \tan(\theta)Q\sin(\phi) + R\cos(\phi) \tag{63}$$

$$\dot{\psi} = \frac{Q\sin(\phi) + R\cos(\phi)}{\cos(\theta)} \tag{64}$$

The final set of equations concern the translational distances covered across the inertial reference frame. This was found via a conversion matrix between the body and inertial frames as shown below in equation (65).

$$\begin{bmatrix} \dot{E} \\ \dot{N} \\ \dot{h} \end{bmatrix} = \begin{bmatrix} C(\theta)C(\psi) & S(\phi)S(\theta)C(\psi)-C(\phi)S(\psi) & C(\phi)S(\theta)C(\psi)+S(\phi)S(\psi) \\ C(\theta)S(\psi) & S(\phi)S(\theta)S(\psi)+C(\phi)C(\psi) & C(\phi)S(\theta)S(\psi)-S(\phi)C(\psi) \\ -S(\theta) & S(\phi)C(\theta) & C(\phi)C(\theta) \end{bmatrix} \begin{bmatrix} \dot{u} \\ \dot{v} \\ \dot{w} \end{bmatrix}$$

(65)

Where:

E = Position along the inertial frame E-axis (ft)
N = Position along the inertial frame N-axis (ft)
h = Position along the inertial frame h-axis (ft)

These equations of motion formed a new state and control matrix. The state vector was a 12x1 vector that described all of the sailplane's body fixed velocities, angular velocities, Euler angles, and translational position in inertial space. This state vector was subject to the conventional controls of the sailplane, namely aileron, rudder, and elevator deflections, which formed a 3x1 control vector. These vectors are shown below.

$$S = \begin{bmatrix} u \\ v \\ w \\ \phi \\ \theta \\ \psi \\ P \\ Q \\ R \\ E \\ N \\ h \end{bmatrix} \tag{66}$$

$$U = \begin{bmatrix} Ail \\ Elev \\ Rdr \end{bmatrix} \tag{65}$$

LAMARS Simulator Development

Equations (39) through (65) were first constructed and then verified using MATLAB® simulations. Once the state equations propagated appropriately based on control surface deflections and environmental conditions, the MATLAB® code was then translated into C++ code for use with the Air Force Research Laboratory's VACD LAMARS facility located at Wright Patterson AFB, OH. This prototype dynamic soaring flight simulator was the second phase of the flight simulator build up.

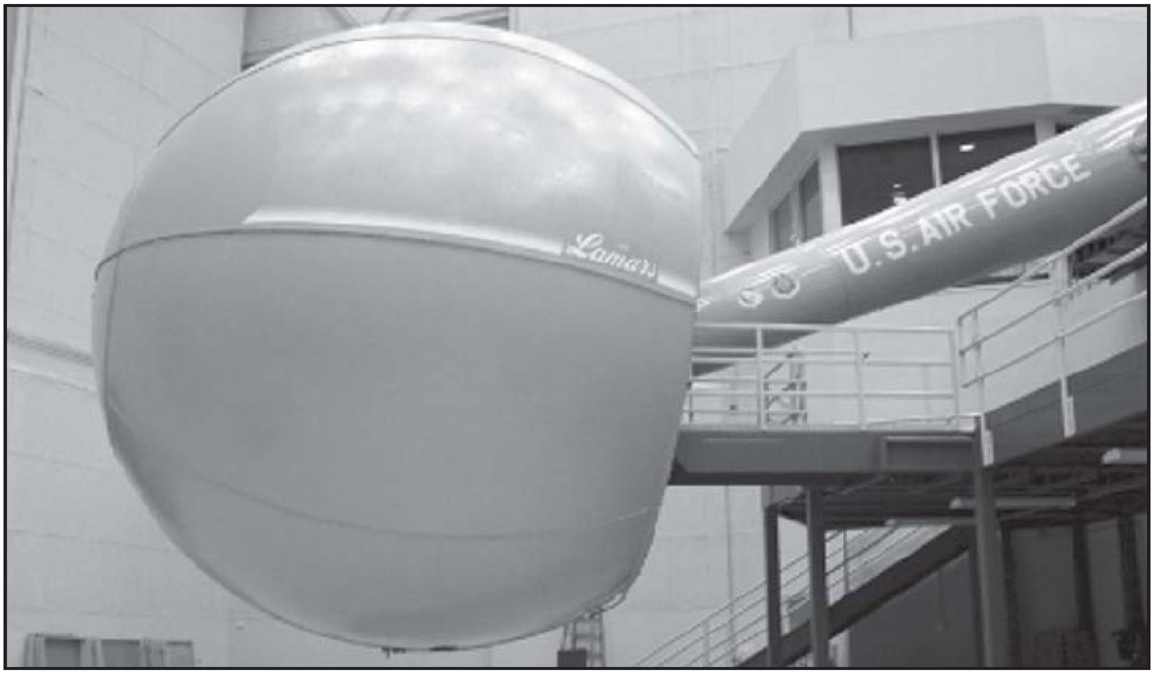

Figure 52. LAMARS Facility

LAMARS was chosen as a build up to the final flight simulator because of its successful 30 year history of simulating various aircraft for a wide variety of Air Force research programs. From a risk reduction standpoint, the simulator's pilot-to-vehicle interface was well validated and the software engineers that programmed and maintained LAMARS were highly experienced. Furthermore, the LAMARS simulator featured a wide angle 120° field of view and a heads up display (HUD). All of these features made easier the task of evaluating the implementation of the dynamic soaring aircraft equations of motion in a flight simulator. As a final note, any parameter of the dynamic soaring profile could be output in a matrix format compatible with MATLAB® input protocols. This allowed for near real-time analysis of any simulated dynamic soaring flight. An example screen shot from the pilot’s cockpit is shown in Figure 53.

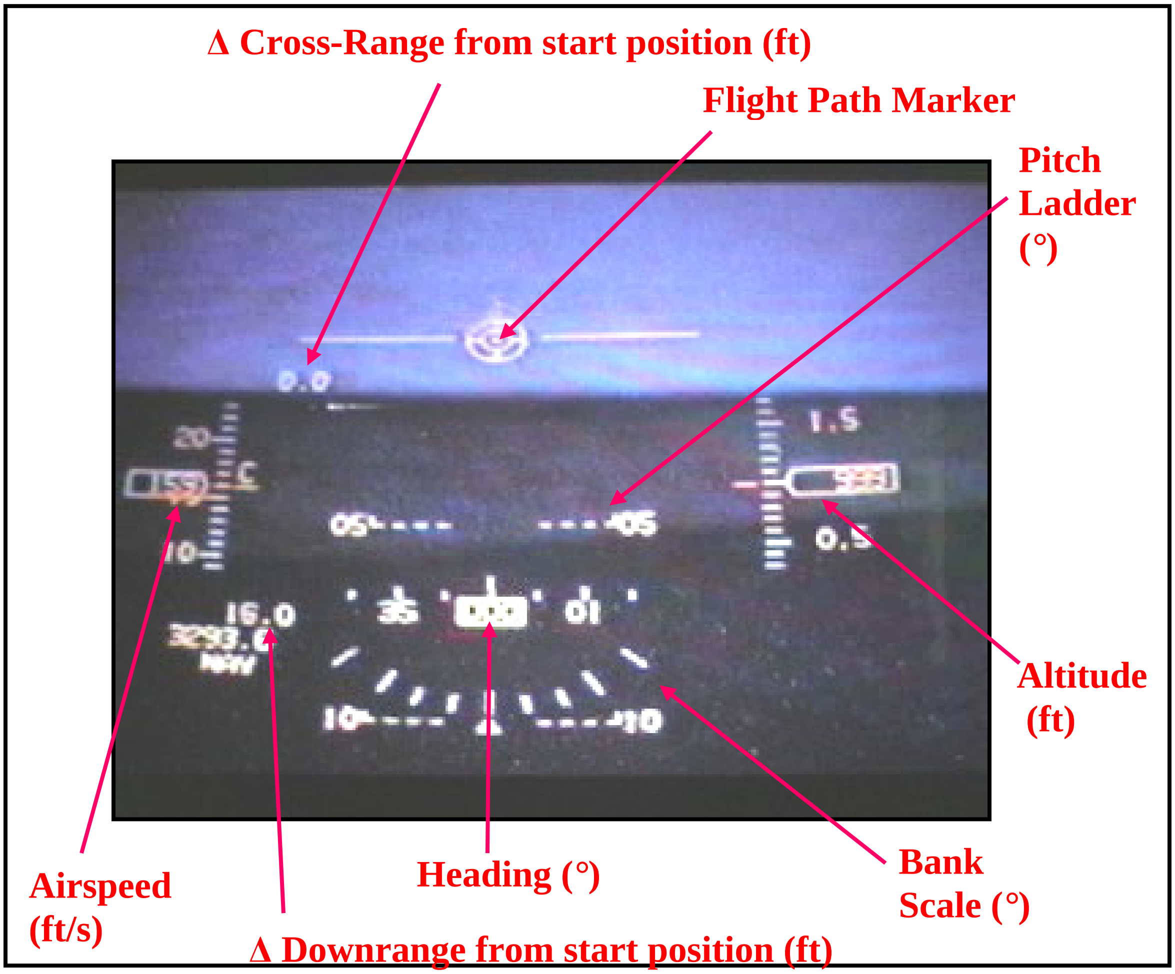

Figure 53. LAMARS Sailplane Heads Up Display

Using the experience gained from the LAMARS prototype flight simulator, the final stage of the dynamic soaring flight simulator build up process could begin. Again, because of the ground breaking nature of this research, no dynamic soaring instrumentation, displays, or procedures existed. These would all have to be developed specifically for this research and refined in a flight simulator in order to improve flight test efficiency and data results.

APEX Simulator Development

The prototype LAMARS flight simulator was primarily used to evaluate the implementation of the dynamic soaring aircraft equations of motion and to build an initial experience base on simulator development and ease of flying the hairpin and anti-hairpin maneuvers. Hence, the final stage of the flight simulator development was used to develop the electronic avionics displays, to refine the dynamic soaring maneuvers, and to collect flight simulator data predictions for actual flight test. The NASA Dryden flight simulator facility was chosen for this task due to their extensive experience with developing advanced flight research simulators. NASA Dryden's APEX flight simulator, shown in Figure 54, was originally developed in 1992 to simulate sailplane flight for a project using a modified glider developed by NASA (NASA Dryden). As such, it was already capable of accepting the L-23 Super Blanik aerodynamic model and the dynamic soaring aircraft equations of motion developed and refined with MATLAB® and the prototype flight simulator used at the LAMARS facility.

Figure 54. NASA Dryden APEX Flight Simulator Facility with DynaSoar 3.0 Display

In addition, the NASA Dryden Flight Research Center instrumentation office was chosen as the agency to develop the dynamic soaring flight displays. The proximity of NASA Dryden to the USAF Test Pilot School also greatly facilitated the concurrent development and coordination efforts required to integrate the research simulator with the electronic avionics display.

Experience with the prototype LAMARS simulator in phase two emphasized the need for the flight crew to be able to precisely track pitch, yaw, and roll real-time in order to ensure maneuver precision and repeatability across various flight crews. The prototype also demonstrated the need to automatically calculate and display specific energy and specific excess power for the dynamic soaring maneuvers to the flight crew. The position and strength of wind shears would also have to be known real-time so that flight crews could orient the hairpin and anti-hairpin accurately. Lastly, flight crews would also need to be able to precisely track the trajectory of their maneuvers for in flight real time analysis and post flight reconstruction. The final software package developed for this research, known as DynaSoar Version 3.0, was installed on a Motion Computer Tablet PC unit and mounted in both cockpits in the actual sailplane and also in the simulator (reference Figure 54). Because the hardware interface in both the APEX simulator and the actual L-23 sailplane were identical, this integration allowed the test aircrew to build sufficient experience with the electronic avionics display in anticipation of flight test. In addition, the output data files from both the simulator and the aircraft were exactly the same. This allowed for data reduction and analysis protocols to be verified and validated before the beginning of flight test. An example of the DynaSoar 3.0 electronic display is shown in Figure 55

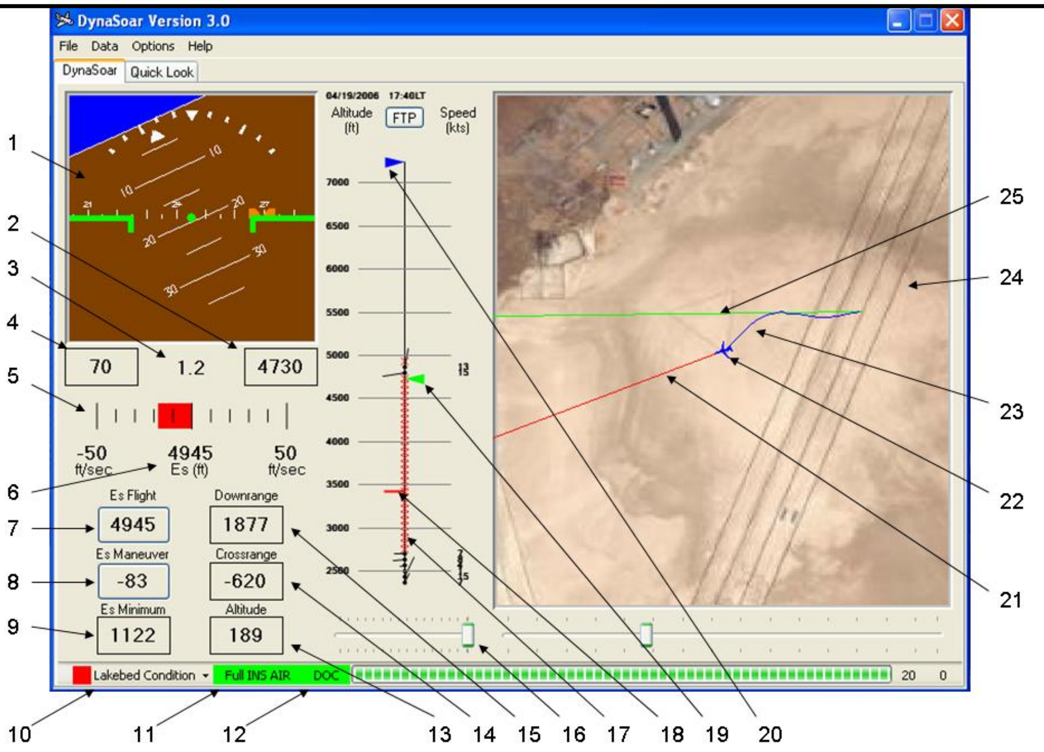

1	Attitude ball with embedded heading scale and heading bug (bug was set at start of maneuver when the HOS controller was pressed)	14	Cross range distance from start of maneuver (ft)
2	Pressure altitude (ft)	15	Downrange distance from start of maneuver (ft)
3	Normal load factor	16	Wind data zoom control
4	Airspeed (KIAS)	17	Wind data (altitude, direction, speed)
5	Energy rate Ps gauge (ft/sec) (Negative rate displays a red bar, Positive rate displays a green bar)	18	Energy height bingo (ft MSL)
6	Energy height (ft MSL)	19	Pressure altitude (ft)
7	Energy height (ft AGL): Prior to takeoff this button was pressed to zero the energy height. (Below bingo energy the block turns red)	20	Energy height (ft MSL) (Energy height shown is not representative of an actual flight because the picture shown was not captured in flight.)
8	Energy difference from start of maneuver (ft)	21	Current heading reference line (red)
9	Energy height bingo (ft AGL)	22	Own ship icon
10	Lakebed status toggle (red/green)	23	Ground track history (blue)
11	EGI/GPS status display	24	Moving map display with zoom control
12	DAS status display (Green indicates data is recording)	25	Start of maneuver heading reference line (green)
13	Altitude from start of maneuver (ft)		

Figure 55. Dynamic Soaring DynaSoar 3.0 Avionics Display

Using this electronics display coupled to the concurrently developed NASA Dryden APEX dynamic soaring flight simulator, refinement of the dynamic soaring flight maneuvers and procedures used for actual flight test could begin.

The DS FTT developed for this project, shown in Figure 56, was selected to optimize energy extraction from horizontal wind shear, while at the same time ensuring repeatability, simplifying data analysis, and abiding by flight safety restrictions (Gordon, 2006:6). This modified profile was necessarily less aggressive than the point mass optimal trajectory due to the fact that the point mass model was not restricted by moments of inertia, pilot capabilities, or low altitude safety maneuvering restrictions, whereas the 6-DOF flight simulator and actual aircraft were. The result was an elongated profile with downrange distances on the order of 2000-3000 feet and trajectory times between 20 to 25 seconds. The energy state impact of this modified profile in comparison to the optimal profile is detailed at the end of this chapter in Table 5 and Table 6.

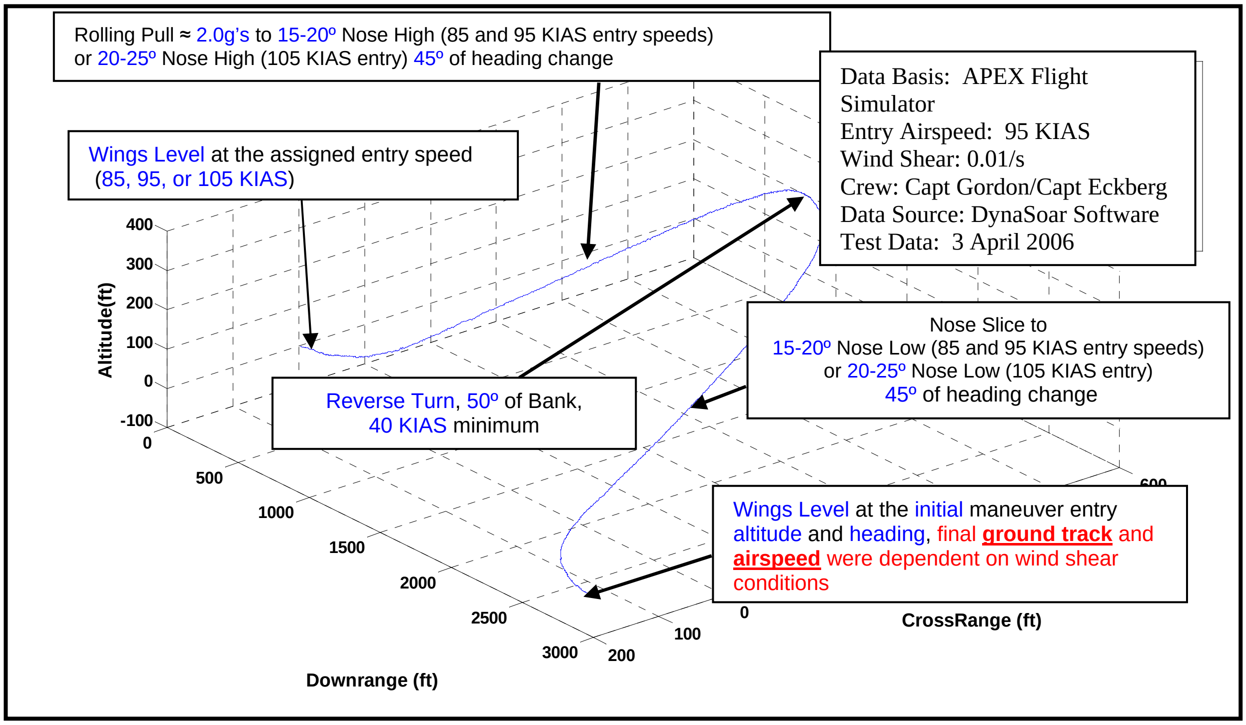

Rolling Pull ≈ 2.0g's to 15-20º Nose High (85 and 95 KIAS entry speeds) or 20-25º Nose High (105 KIAS entry) 45º of heading change

Wings Level at the assigned entry speed (85, 95, or 105 KIAS)

Data Basis: APEX Flight Simulator
Entry Airspeed: 95 KIAS
Wind Shear: 0.01/s
Crew: Capt Gordon/Capt Eckberg
Data Source: DynaSoar Software
Test Data: 3 April 2006

Reverse Turn, 50º of Bank, 40 KIAS minimum

Nose Slice to 15-20º Nose Low (85 and 95 KIAS entry speeds) or 20-25º Nose Low (105 KIAS entry) 45º of heading change

Wings Level at the initial maneuver entry altitude and heading, final **ground track** and **airspeed** were dependent on wind shear conditions

Figure 56. Dynamic Soaring Flight Test Technique

Three airspeeds, 85, 95, and 105 KIAS were used to enter the maneuver based on the dynamic optimization described earlier in this Thesis. The DS FTT was initiated from wings level flight at the target entry airspeed, perpendicular to the wind, and at the bottom of the wind shear gradient. The pilot smoothly rolled and pulled to execute a 45º heading change simultaneous with a 15º to 25º pitch up. For an entry airspeed of 85 KIAS the pitch up was 15-20º, and for a 95 or 105 KIAS entry the pitch up was 20-25º. As airspeed decreased in the climb the pilot reversed the turn and rolled the aircraft to approximately 50º of bank across the apex of the maneuver. At the apex of the maneuver the nose was near the horizon and the sailplane was back on the maneuver entry heading. Minimum airspeed over the top was 40 KIAS, and the apex altitude was 200-400 feet above the entry altitude depending on the entry airspeed. As the sailplane was turned back towards the original ground track the nose was allowed to drop to 15 to 25º nose low *(amount of nose low attitude matched the amount of nose high attitude on the* *first leg of the maneuver)*. As the sailplane descended, the pilot again reversed the roll and pulled to fly back to the initial heading and altitude. The maneuver ended with the sailplane on the entry heading and altitude with the wings level. Just as described in the MATLAB® analysis, a hairpin maneuver was defined by flying the DS FTT with a climb into a headwind and a descent with a tailwind. An anti-hairpin maneuver was defined by flying the DS FTT with a climb into a tailwind and a descent with a headwind.

Aircrew coordination procedures were refined in the APEX simulator such that the pilot in the front cockpit of the sailplane was primarily responsible for flying the maneuver and had overall responsibility for safety of flight. The rear cockpit crewmember, a flight test engineer (FTE) or flight test navigator (FTN), would be primarily responsible for providing clearance to the pilot to continue to fly the profile based on established criteria for data and maneuver tolerances. The rear cockpit crew member would also provide altitude pacing calls to the pilot to ensure maneuvers ended at the altitude where the maneuvers started. With this modified profile maneuver defined and avionics display completed, flight test simulations could begin.

As in the point mass model, the simulator was initialized with the sailplane pointed North and centered at the origin of a North-East-Down inertial frame. Winds were initialized to blow directly from the West with a linear wind shear profile based on historic wind shear conditions at Edwards AFB as provided by the NASA DFRC weather observatory. The sailplane was initialized approximately 1000 ft above the start of the shear layer in order for aircrews to gain experience judging the amount of altitude required to dive to the bottom of the shear layer and arrive at the appropriate entry airspeed conditions. Experience with this setup for the initial conditions would later help aircrews during flight test to best position the tow aircraft to release the sailplane in an optimal position to exploit the wind shear. Due to the identical DynaSoar 3.0

hardware/software used in the simulator and the sailplane, the output data protocols and data reduction/analysis for both flight test and simulator trials were exactly the same. The data reduction methodology was designed to mirror the point mass analysis techniques to the greatest extent possible in order to simplify data reduction and comparisons. Ultimately, over 100 dynamic soaring sorties were performed in the flight simulator across a range of entry airspeed and wind shear conditions. Examples of the resulting data plots from the DynaSoar 3.0 package for a single dynamic soaring hairpin maneuver are provided below.

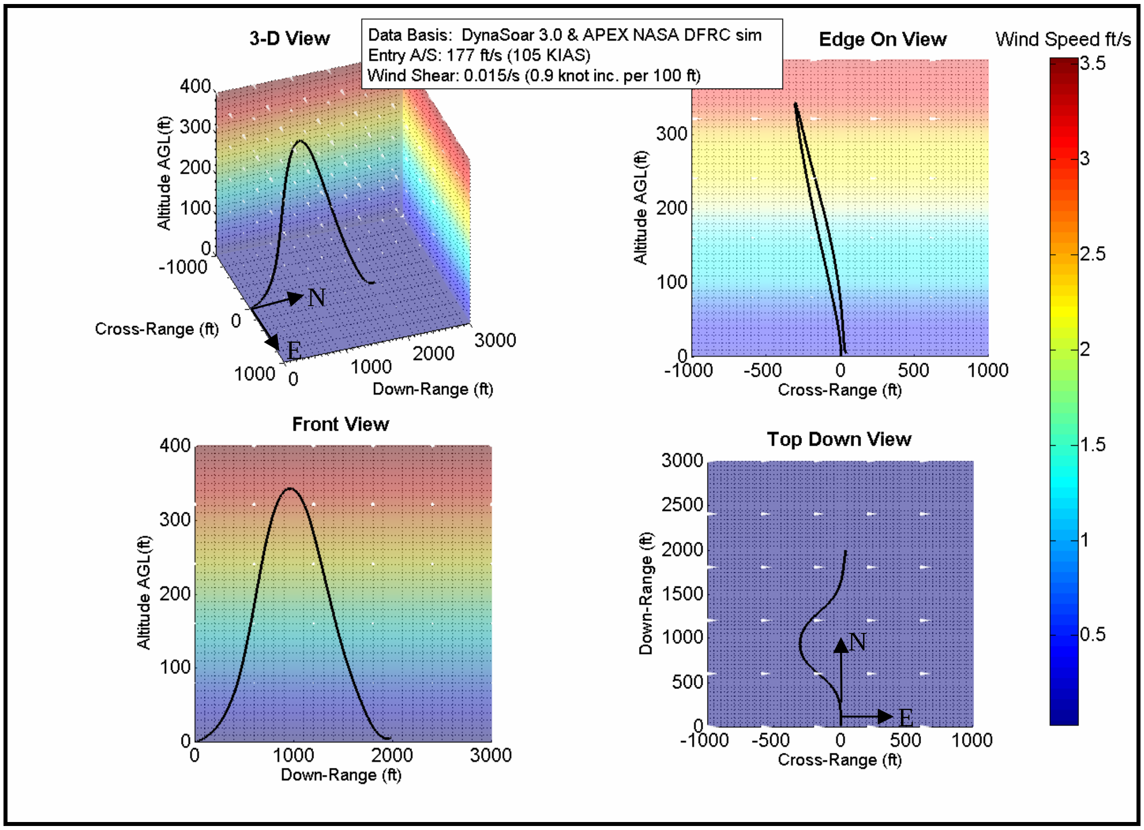

Figure 57. APEX Simulator Hairpin Trajectory (0.016 ft/s / ft Wind Shear)

For this example, a wind shear strength of 0.015 ft/s / ft was used since this represented an average Edwards AFB wind shear. In this simulation with a 105 KIAS entry airspeed, the sailplane traveled North approximately 2000 ft and achieved a maximum altitude gain of approximately 320 feet. Total time for the trajectory was 17 seconds. These details are illustrated in greater detail in Figure 58.

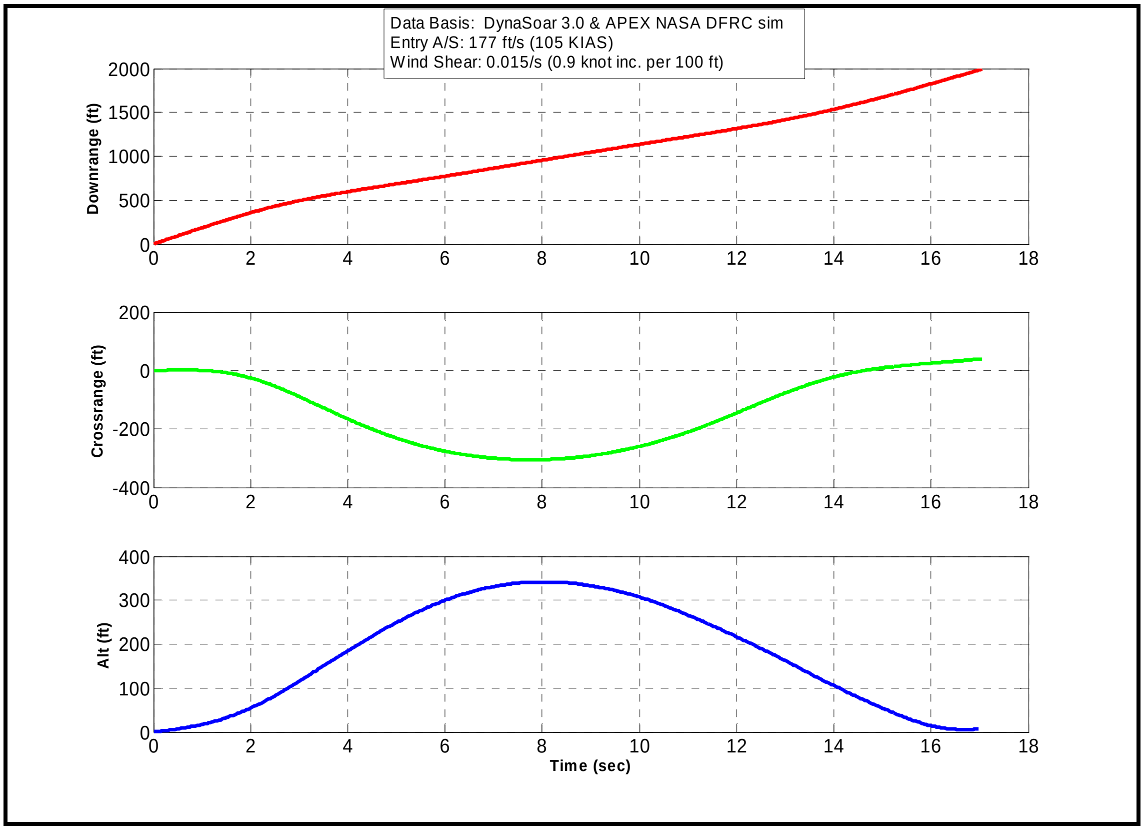

Figure 58. APEX Simulator Trajectory Data (0.015 ft/s / ft Wind Shear)

Using the modified profile, the sailplane traveled approximately 1300 feet further downrange and 150 feet further cross range than the optimal profile with the same 105 KIAS entry speed. The resulting inertial velocities from this elongated profile are shown in Figure 59.

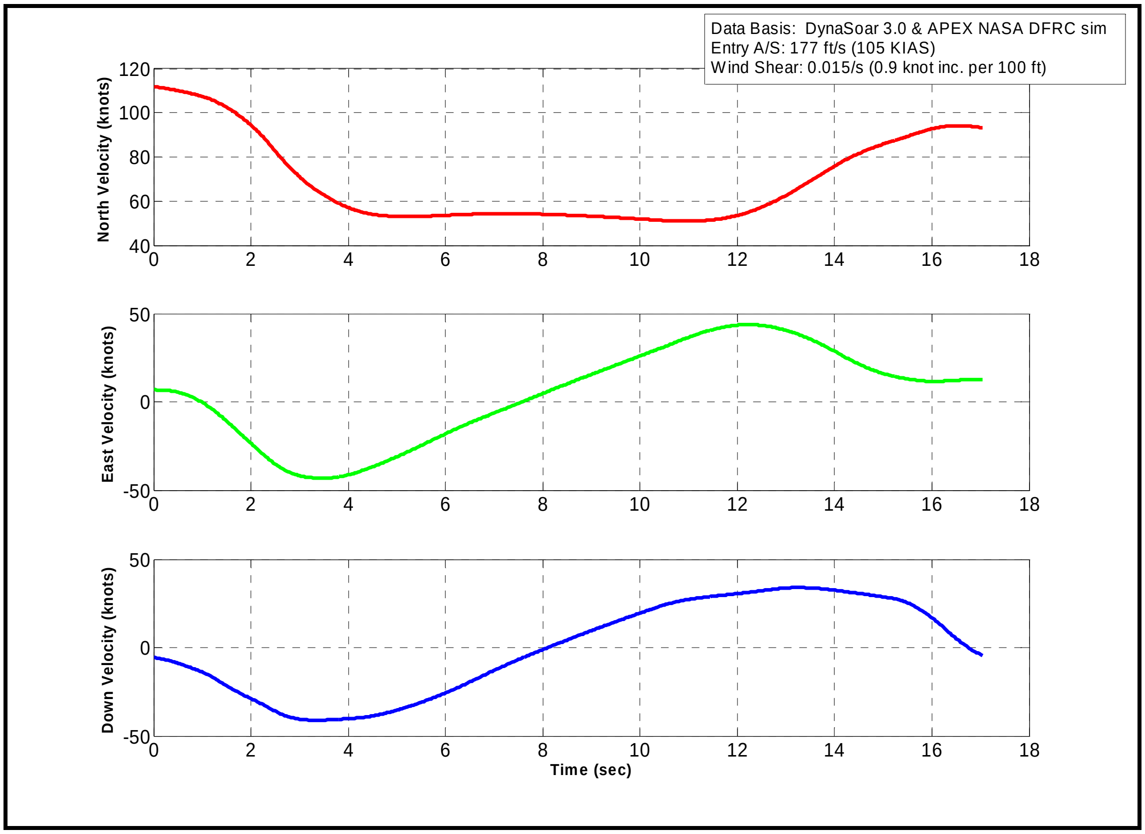

Figure 59. APEX Simulator Inertial Velocities (0.015 ft/s / ft Wind Shear)

Figure 59 illustrates an aircraft that began its profile oriented North, entered a decelerating climbing turn to the West followed by an accelerating descending turn to the East, and finally completed its profile traveling North again. When these inertial velocities were converted using the inverse of the matrix shown in equation (65), the resulting body fixed velocities became as shown in Figure 60.

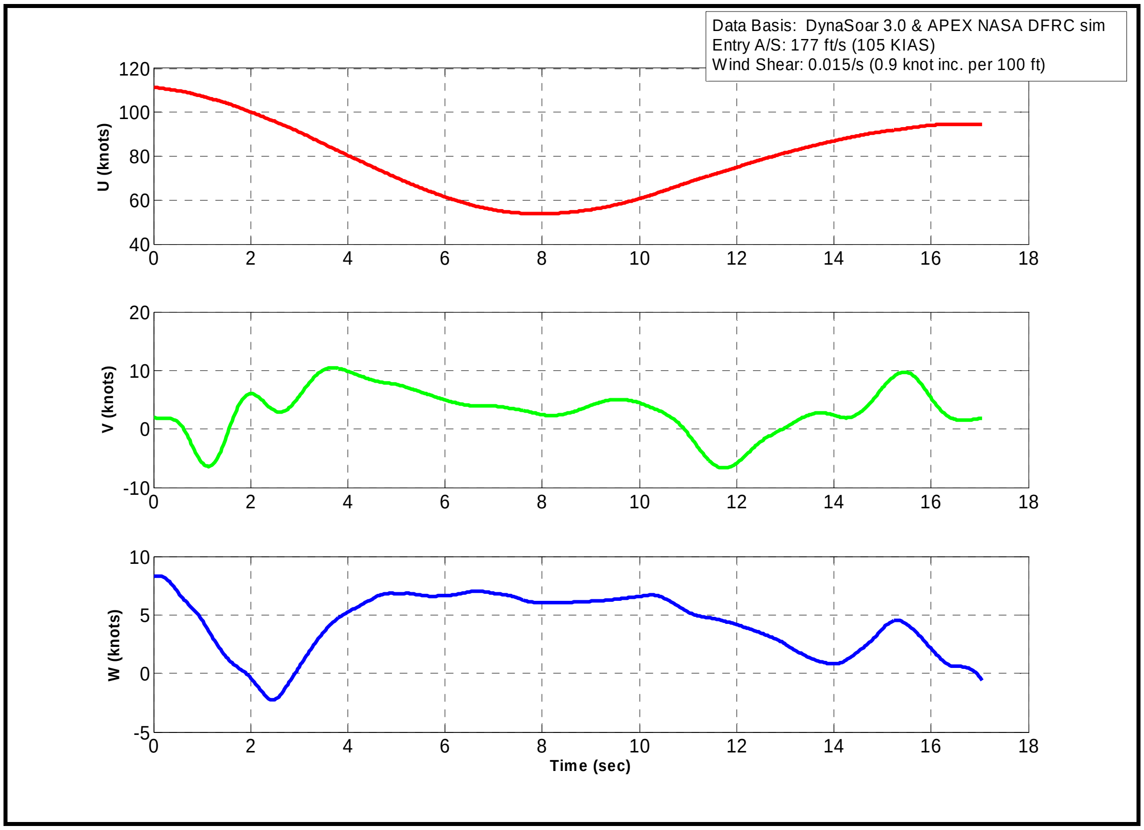

Figure 60. APEX Simulator Body Fixed Velocities (0.015 ft/s / ft Wind Shear)

The most significant velocity change from the optimal profile can be seen by studying the top plot in Figure 60. Since the modified profile was designed partly with safety and pilot repeatability considerations in mind, airspeed changes, particularly at the apex of the maneuver, were less dramatic than the optimal profile. Whereas the optimal profile commanded the sailplane to decrease its velocity to approximately 25 KIAS at the apex, the modified profile only decayed to approximately 55 KIAS. This was designed to ensure that the aircraft never decelerated past 40 KIAS, an airspeed chosen to provide sufficient safety margin above the stall speed of 35 KIAS. This change in the airspeed profile was responsible for the elongated shape of the modified profile as compared to the optimal profile. Euler angle information about the simulator flight is shown in Figure 61.

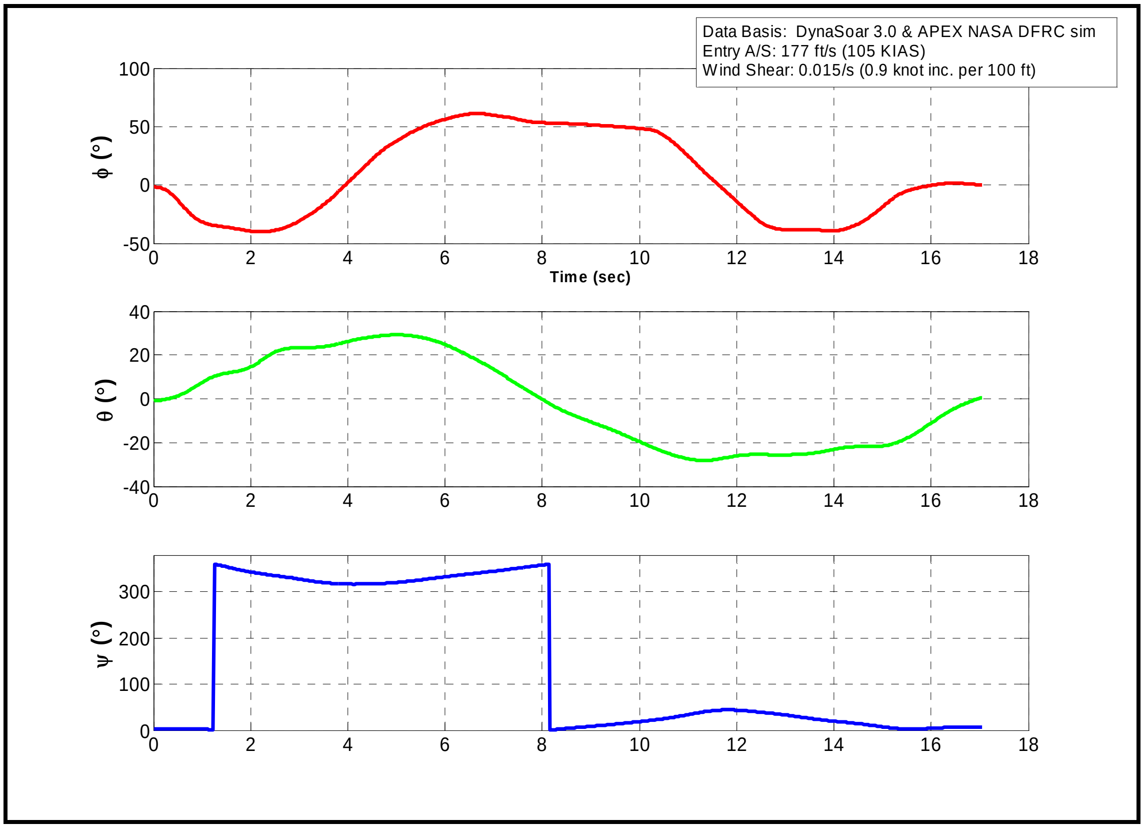

Figure 61. APEX Simulator Euler Angles (0.015 ft/s / ft Wind Shear)

Figure 61 describes an aircraft that smoothly blended pitch, bank, and roll angles to transcribe an inclined sinusoidal like path across the sky. Unlike the optimal profile, the maximum nose high and nose low pitch angles in this example were only approximately ±25º as opposed to upwards of ±55º. This was performed so as to keep the modified profile’s minimum airspeed above the 40 KIAS limit described earlier. Body fixed angular rates encountered during this maneuver are illustrated in Figure 62.

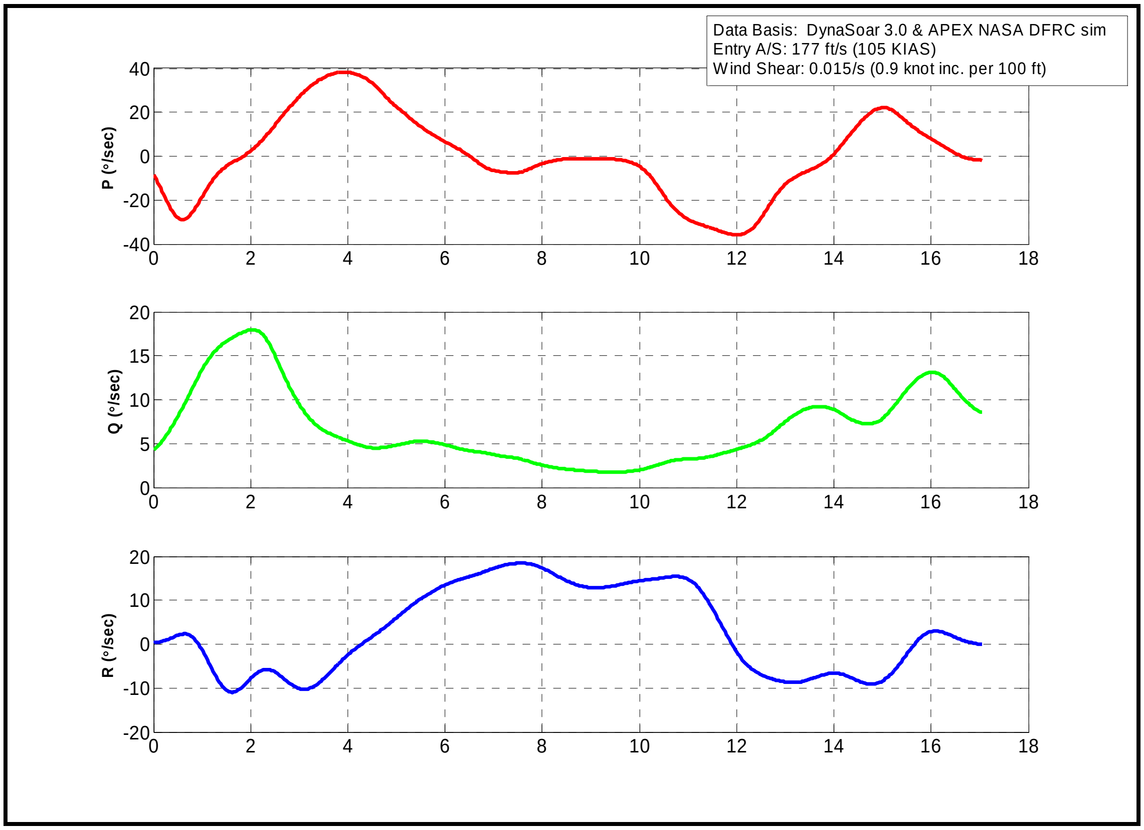

Figure 62. APEX Simulator Angular Rates (0.015 ft/s / ft Wind Shear)

Of interest in Figure 62 is the increase in yaw rate, *R*, during the middle of the profile. Yaw rates remained relatively low until the aircraft reached the peak of the trajectory, at which point the yaw rate increased to approximately 20 deg/s as the nose sliced down and to the right during the turn reversal back to the East. The simulator runs indicated that this yaw rate, while moderately high, was normal for an aircraft in a near stall turn reversal, did not laterally overstress the aircraft, and should not disorient the pilot during its execution so long as it is performed in clear visual meteorological conditions. The profile detailed in the previous simulator figures ultimately produced the energy state of the sailplane as shown in Figure 63.

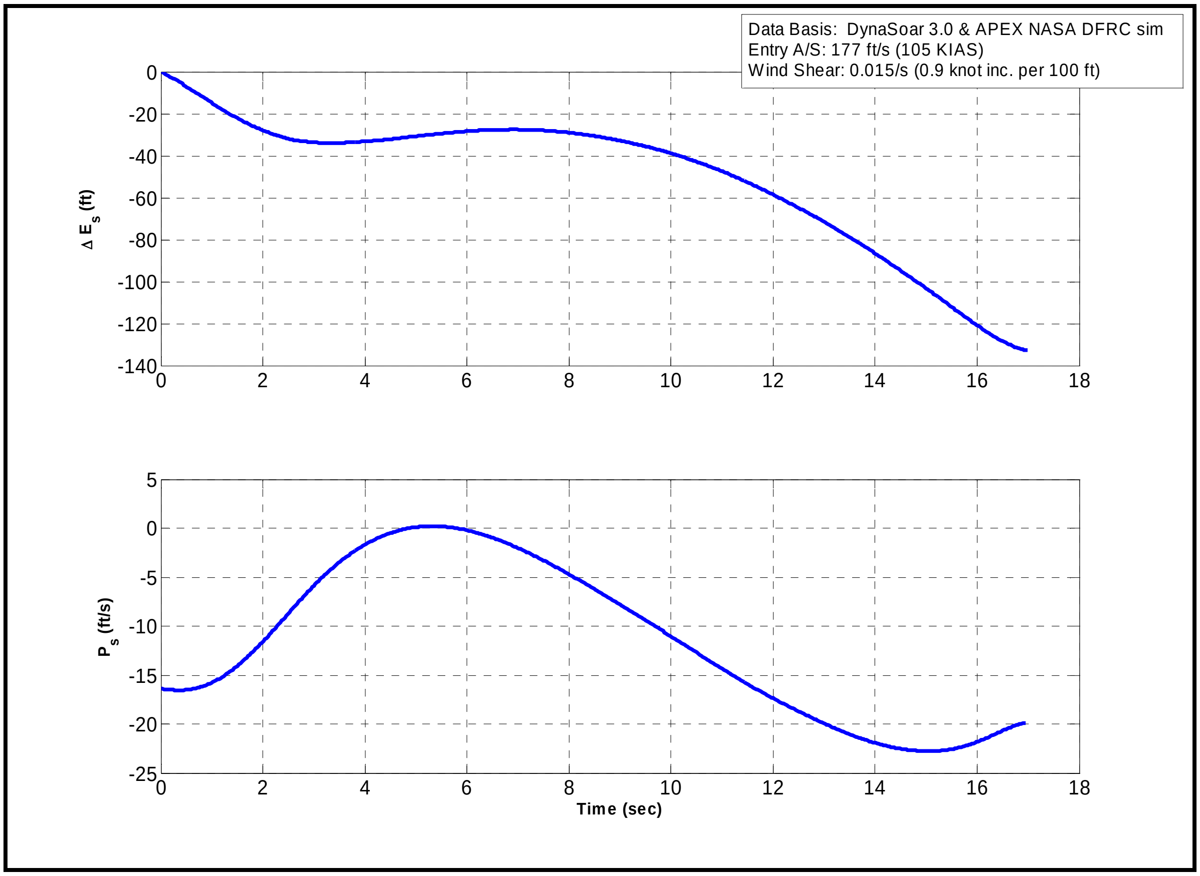

Figure 63. APEX Simulator Energy State Performance (0.015 ft/s / ft Wind Shear)

Energy states for both the flight simulator and the actual test aircraft were derived using Pitot-static theory. Pitot-static derived energy data were calculated using the sailplane's Pitot static instruments for airspeed and altitude sources, and then applying standard Pitot static corrections as appropriate before calculating energy states.

Pitot static energy states were governed by the following equation:

$$Es_{Pitot-static} = H_{corrected} + \frac{V_t^2}{2g} \tag{66}$$

In equation (66), true airspeed, or V_t, and the corrected altitude, or $H_{corrected}$, were determined by recording the indicated airspeed, indicated outside air temperature, indicated dynamic pressure, and indicated static pressure and applying the following corrections as determined by trailing cone Pitot-static calibration flights in preparation for flight test.

$$Pstatic_{CORRECTED} = Pstatic_{INDICATED} - (C_P) * q_{INDICATED} \tag{67}$$

$$q_{INDICATED} = 0.5*\rho_{SL}*V_i^2 \tag{68}$$

$$q_{CORRECTED} = (1 + C_P)* q_{INDICATED} \tag{69}$$

$$\rho = \frac{P_{STATIC_{CORRECTED}}}{R*OAT} \tag{70}$$

$$V_t = \sqrt{2*\frac{q_{CORRECTED}}{\rho}} \tag{71}$$

Where:

C_P = Test Pitot-static nose boom pressure correction coefficient (0.095 from flight test)
V_i = Indicated airspeed (ft/s)
V_t = True airspeed (ft/s)
ρ_{SL} = Density at Sea Level (0.002377 slug/ft^3)
$q_{INDICATED}$ = Indicated dynamic pressure (lbs/ft^2)
$q_{CORRECTED}$ = Corrected dynamic pressure (lbs/ft^2)
$P_{static\ INDICATED}$ = Indicated static pressure (lbs/ft^2)
$P_{static\ CORRECTED}$ = Corrected static pressure (lbs/ft^2)
OAT = Outside air temperature (ºR)
R = Atmospheric gas constant (1716 ft lbf / (slug ºR))

Since, during actual flight test, dynamic soaring maneuvers could be initiated at any altitude depending on the vertical location of the prevailing wind shear, the initial energy state at the start of the maneuver was set as a reference energy state, and then the change in energy state was tracked from this initial value. This technique was the same as that applied to energy state measurements performed earlier in the Thesis. In the example in Figure 63, the shape of the E_s and P_s profiles was identical to those predicted by dynamic optimization. The final ΔE_s value was nearly twice the energy loss predicted in dynamic optimization from flying the much more aggressive optimal profile, but nearly identical to the mathematically predicted energy loss from flying the modified profile. This fact lended credence to the viability of the mathematical analysis performed in anticipation of flight test.

Ultimately, the experience gained from the flight simulator was invaluable in preparing for flight test. It represented the bridge between dynamic optimization and practical application. The final results of this modeling and simulation effort, both from dynamic optimization and the flight simulator research, are presented in Table 5 and Table 6. Results are presented for both the hairpin and anti-hairpin maneuvers.

Table 5. Summary of Dynamic Soaring Hairpin Modeling and Simulation

Entry Airspeed	*No Wind Shear (BASELINE) ΔE_s (ft)*			*0.02 ft/s / ft Wind Shear ΔE_s (ft)*			*0.04 ft/s / ft Wind Shear ΔE_s (ft)*		
	Optimal Profile MATLAB®	Modified Profile MATLAB®	Flight Simulator (APEX)	Optimal Profile MATLAB®	Modified Profile MATLAB®	Flight Simulator (APEX)	Optimal Profile MATLAB®	Modified Profile MATLAB®	Flight Simulator (APEX)
143 ft/s (85 KIAS)	**-75**	**-103**	**-117**	**-58**	**-96**	**-105**	**-40**	**-88**	**-92**
160 ft/s (95 KIAS)	**-83**	**-146**	**-136**	**-77**	**-136**	**-122**	**-60**	**-116**	**-98**
177 ft/s (105 KIAS)	**-97**	**-185**	**-180**	**-80**	**-165**	**-163**	**-57**	**-128**	**-138**

Direction of Increasing *Energy Benefit* →

Table 6. Summary of Dynamic Soaring Anti-hairpin Modeling and Simulation

Entry Airspeed	*0.04 ft/s / ft Wind Shear ΔE_s (ft)*			*0.02 ft/s / ft Wind Shear ΔE_s (ft)*			*No Wind Shear (BASELINE) ΔE_s (ft)*		
	Optimal Profile MATLAB®	Modified Profile MATLAB®	Flight Simulator (APEX)	Optimal Profile MATLAB®	Modified Profile MATLAB®	Flight Simulator (APEX)	Optimal Profile MATLAB®	Modified Profile MATLAB®	Flight Simulator (APEX)
143 ft/s (85 KIAS)	**-106**	**-118**	**-140**	**-95**	**-111**	**-131**	**-75**	**-103**	**-117**
160 ft/s (95 KIAS)	**-102**	**-171**	**-167**	**-89**	**-160**	**-150**	**-83**	**-146**	**-136**
177 ft/s (105 KIAS)	**-132**	**-221**	**-223**	**-114**	**-205**	**-200**	**-97**	**-185**	**-180**

← ***Direction of Increasing*** *Energy Penalty*

As would be expected, the optimal profile performed the best from an energy state perspective. When the optimal profile was shifted to the modified profile, the results from the MATLAB® dynamic optimization and flight simulator matched very closely. The small differences in results were due to slight variations in pilot technique and the inability of flight crews to fly the profile exactly as the MATLAB® analysis commanded. With modeling and simulation complete, dynamic soaring flight test could finally begin.

IV. Flight Test

Flight Test Overview

Flight Test, shown in Figure 64, were conducted over the northern portion of the Rogers dry lakebed at Edwards AFB California. Dynamic soaring test flights were conducted under the program title SENIOR ShWOOPIN (**Sh**ear **W**ind **O**bserved **O**ptimized **P**ath **I**nvestigation for **N**ASA). SENIOR ShWOOPIN (Gordon, 2006) was the world's first investigation into full size sailplane dynamic soaring and represented the culmination of the mathematical analysis and simulation conducted for this research.

Figure 64. L-23 and Tow plane Launch on a Test Sortie

By the conclusion of the SENIOR ShWOOPIN flight test program, one hundred thirty-eight sorties in the L-23 (88 test sorties and 50 training/avionics validation flights) were performed. The test window for this project was 15 March to 18 May 2006. A total of 27 hours of flight test were accomplished.

The core test team consisted of three flight test pilots, two FTEs, and one FTN. This test team was supported by two NASA weather specialists, two NASA avionics and instrumentation technicians, two NASA simulator technicians, two soaring operations advisors, and three tow plane pilots. Members of this test team are shown in Figure 65.

Figure 65. SENIOR ShWOOPIN Test Team

The overall flight test objectives were four-fold:

1. Compare the energy gained or lost during the hairpin and anti-hairpin maneuvers, both in a wind shear and without wind shear (baseline energy loss case).
2. Determine if full size sailplanes could extract energy from horizontal wind shears.
3. Evaluate the L-23 sailplane modeling and simulation data in comparison to flight test data.
4. Qualitatively evaluate the utility of dynamic soaring as a practical maneuver for full size sailplanes.

These objectives were based on the mathematical analysis and simulations already accomplished for this research and were designed to support the overall objective of this project to prove or disprove the viability of dynamic soaring for full size sailplanes. All test objectives were met.

Since this was the first project of its kind, the L-23 sailplane used by the SENIOR IDS and HAVE BLADDER test teams needed to be modified into a specialized dynamic soaring research aircraft. This aircraft featured unique avionics and instrumentation specifically developed for this project. A complete description of this test aircraft is provided below in order to illustrate its unique characteristics with respect to a stock model L-23 Super Blanik sailplane.

Test Aircraft Description

The L-23, shown in Figure 66, was designed and manufactured by LET Aeronautics Works in the Czech Republic and was marketed in the United States by Blanik America, Wenatchee, WA (LET, 1993). The two-place, tandem cockpit L-23 was owned by the USAF TPS and made of an all metal structure. The rudder, elevator, and ailerons were fabric covered (LET, 1993). The T-tail was fitted with a conventional elevator and pitch trim tab for pitch control. The main landing gear on the test aircraft was pinned down and the cockpit gear handle had been removed (Gordon, 2006:1). The L-23 glide ratio was 24:1 at approximately 48 KIAS with the speed brake retracted and the landing gear extended (LET, 1993). The conventional three axis flight control system was non-powered and fully reversible. Both cockpits were equipped with a center mounted control stick and rudder pedals that actuated control surfaces with a combination of control push rods and cables. The speed brakes were controlled by levers from either cockpit. The never exceed airspeed was 133 KIAS. Load factor limits were -2.5 to +5.33 *g* at full gross weight *(1124 pounds with two occupants)* (LET, 1993).

Figure 66. L-23 Super Blanik Test Aircraft with Mobile Operations Center

The aircraft was modified with a data acquisition system (DAS) consisting of a five-hole Pitot-static probe, an inertial measurement unit (IMU), two tablet PCs displaying real time attitude, load factor, flight altitude, and E_s information through the DynaSoar 3.0 software, a digital readout of energy height from the total energy variometer probe (rear cockpit), and a digital cockpit camera (Gordon, 2006:2). The total energy variometer was used as a backup to measure the sailplane's energy height. Although this instrument displayed correctly in the cockpit, it was unable to output a correct data stream to the onboard DAS. As a result, it was not used for data analysis. For background theory regarding the total energy variometer reference Appendix D. Total Energy Probe Theory.

Figure 67. Front *(left)* and Rear *(right)* Cockpit Displays Panels

The total weight of modification equipment was 22 pounds allowing for a maximum combined weight of 396 pounds for crewmembers (Gordon, 2006:2). The DAS was completely independent of the production Pitot-static system. The boom mounted five-hole Pitot-static probe had a hemispherical tip, and measured total and differential pressure, provided airspeed, altitude, angle of attack (α), and angle of sideslip (β) signals (Gordon, 2006:2). The digital camera was mounted behind the pilot station to record over the shoulder video. The software on the tablet PC also provided the capability to playback recorded data post flight. The IMU was installed in the baggage compartment behind the rear cockpit. The unit was a battery-powered GS-111m produced by Athena Technologies, Inc, Warrenton, VA (Gordon, 2006:3). It incorporated the sensor suite necessary to provide a full attitude, navigation, and air data solution for use in vehicle flight-state measurement.

The GS-111m was equipped with accelerometers, angular rate sensors, and magnetometers in all three axes, an internal GPS receiver, and air data sensors. A real-time, multi-state Kalman filter was used to integrate the different sensors (Gordon, 2006:3). The aircraft also had a VHF radio to communicate with other aircraft and ground stations. Refer to

Appendix A Instrumentation and Display Sensors for more detailed information about aircraft test instrumentation.

For the sake of dynamic soaring analysis, the performance of the L-23 under test was considered production representative. Because of the unique nature of this research, and the ambitious test objectives, new test operational procedures needed to be developed and executed in a disciplined manner in order to collect the fidelity of dynamic soaring data required for this thesis.

Test Procedures and Execution

Each test period started with an initial crew briefing, lakebed inspection, weather balloon launch, operations setup, and instrumentation check (Gordon, 2006:7). Forecast wind soundings were briefed to the crews to give a general idea as to where the strongest wind shear layer was predicted. Wind shear data were collected periodically with weather balloons. Sonic Detection and Ranging (SODAR) equipment was used to monitor thermal activity (Gordon, 2006:7). This equipment is depicted in Figure 68.

The weather balloon sent raw data including wind direction, wind speed, geopotential altitude, and temperature to a mobile ground station. Two weather technicians downloaded this data and processed it to provide plots of pressure altitude against wind direction and speed. The air temperature was required to determine if an inversion was present—typically a good indication of a shear layer. Weather information was updated at least every 60 minutes, or more frequently based on observed changes in atmospheric conditions.

Figure 68. SODAR Equipment and Weather Balloon

Target altitudes based on wind shear conditions, were briefed to the crew immediately prior to launch, or radioed to a crew already on tow. To ensure rapid communication of the appropriate initial conditions for each DS FTT maneuver, a standardized format for transmitting the initial conditions was developed and reported in the form of a “4-Line” brief. The 4-Line consisted of 1) initial run in heading, 2) altitude targeted, 3) airspeed required, and 4) the wind direction (Gordon, 2006:7).

While the weather information was being collected, the mobile operations center *(see background of Figure 66)* was driven out to the lakebed and the glider and tow plane were prepared for launch. During the glider rollout, the IMU, instrumentation suite, and the avionics suite were powered on and aligned. Normal alignment took approximately 10 minutes. Ground power from the mobile operations center was connected to the glider to extend battery life of the avionics displays. Air traffic control facilities were notified that glider operations were commencing. This activated the range operations area shown in Figure 69**,** restricting other aircraft traffic from interfering with sailplane operations in the test area.

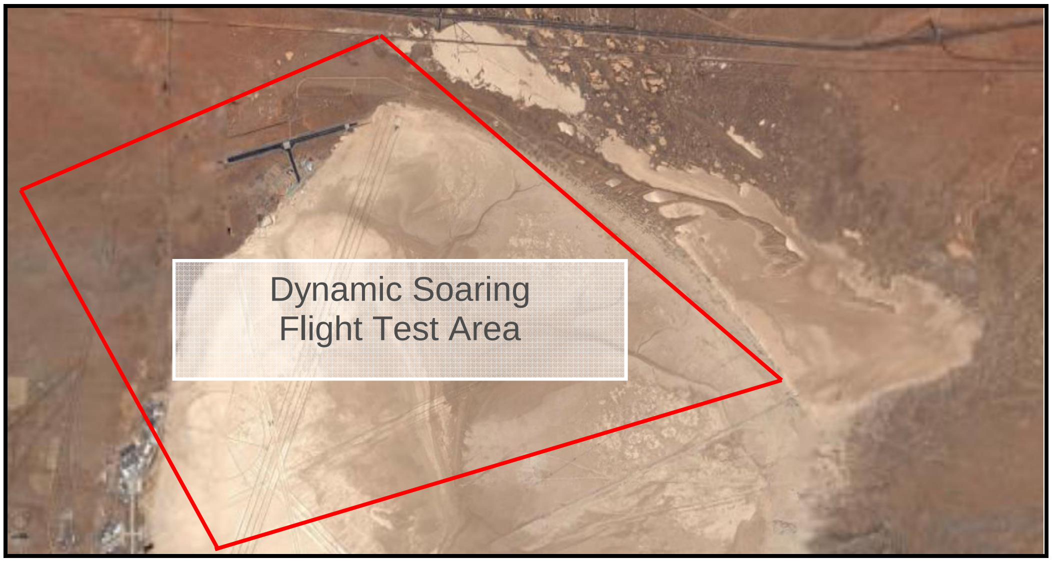

Figure 69. Sailplane Operating Area (North Rogers dry lake)

A modified glider aircrew checklist was run by each crew flying the L-23 prior to each tow. The checklist included standard glider checklist items as well as programming the DynaSoar 3.0 displays. When these checks were complete, the glider aircrew signaled for launch, and the glider was subsequently towed to an altitude approximately 1,000 feet above the wind shear target altitude. This provided time for the aircrew to initiate a dive to stabilize at the target airspeed, and, at aircrew discretion, practice the DS FTT prior to execution.

After each required test point was accomplished, the glider was recovered to the lakebed, as shown in Figure 70, and the crew was either re-launched, or switched out. Qualitative comments were captured immediately upon landing to provide insight into what indications were present upon shear boundary entry and techniques to improve DS FTT execution.

Figure 70. L-23 on Final Approach after a Successful Test Mission

Results and Analysis

Test point selection and data analysis were accomplished through the use of design of experiments (DOE) (Gordon, 2006:9). The test points were selected to vary the controllable factors of crew (pilot + engineer), initial entry airspeed, and hairpin or anti-hairpin maneuver. Clearly, a variable not controlled by the test team was the wind shear. At the end of the project 135 data points were collected. A general linear model analysis was performed using DOE. The critical factors identified in the calculated energy height were maneuver type (hairpin versus anti-hairpin), wind shear magnitude, and entry airspeed. For more information on the DOE employed in the course of this thesis see Appendix C. Design of Experiments Analysis.

Energy State Comparison

The energy gained or lost during the hairpin and anti-hairpin maneuvers were compared using the no wind shear baseline energy loss condition as a reference. This objective required the tracking of sailplane energy height during hairpin and anti-hairpin maneuver execution.

Tracking energy height was accomplished using the Pitot-static method described earlier. Data were compiled from MATLAB® plots generated and analyzed for each flight.

The trajectory data obtained from each flight test generally matched the results obtained from the modified profile modeled in MATLAB® and flown in the APEX simulator. Due to the volume of data and similarity to trajectory figures already described in detail in chapter III, a sample of the complete set of data plots from a flight test sortie is shown in Appendix B. Sample Flight Test Dynamic Soaring Results. Additional flight test data can be found in the SENIOR ShWOOPIN report (Gordon, 2006).

According to dynamic soaring theory, executing a hairpin maneuver in a wind shear should result in a final energy state higher than executing the baseline profile in no wind shear or anti-hairpin maneuver in wind shear. Figure 71 illustrates common trends noted in the energy height performance during flight test across the various dynamic soaring profiles.

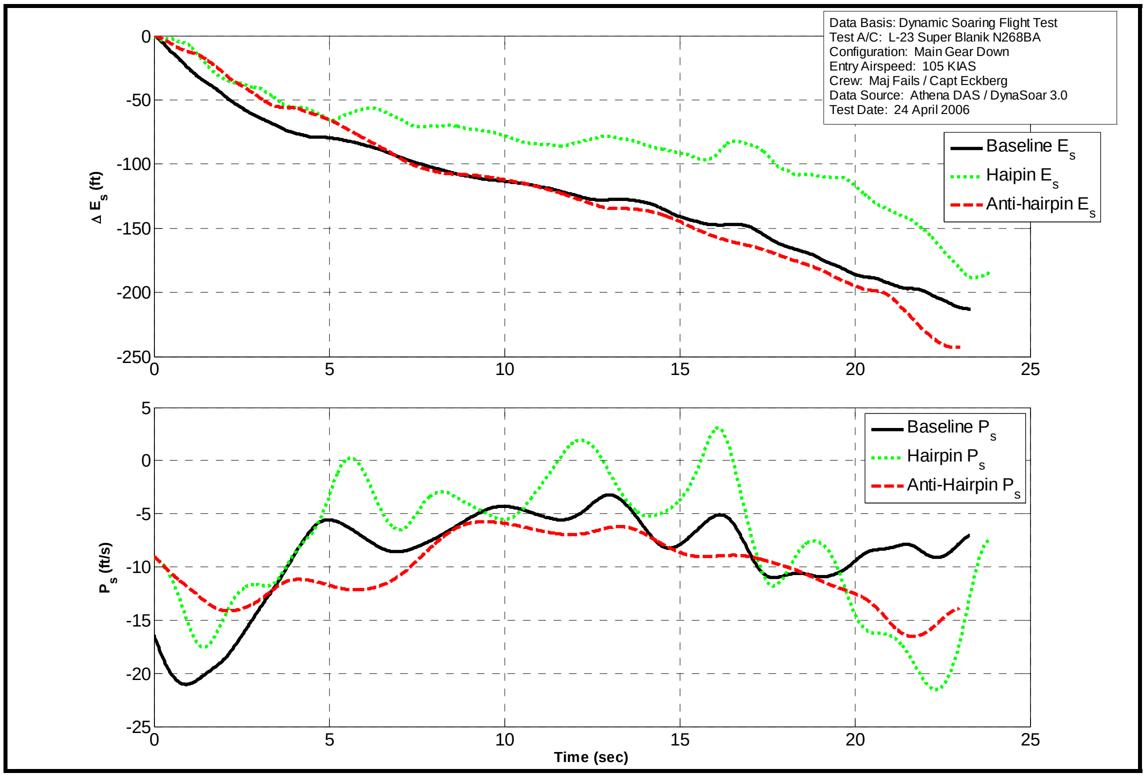

Figure 71. Example Flight Test Energy Height Performance (0.27 ft/s / ft Wind Shear)

Figure 71 illustrates that during the baseline DS FTT performed in no wind shear, the Pitot-static E_s and P_s performance trends were better than those experienced than anti-hairpin maneuvers, but worse than those from hairpin maneuvers. As expected, the baseline performance was in between the hairpin and anti-hairpin. During the hairpin maneuver in wind shear, the Pitot-static energy height was characterized by a shallow decrease or increase in energy height until the aircraft reached the apex of the maneuver. The Pitot-static energy height then decreased sharply as the aircraft accelerated in the descent with the tailwind back to the entry altitude and heading. The P_s trended to be either slightly above or slightly below zero for the majority of the profile, reflecting the energy benefit realized by exploiting the horizontal wind shear. During an anti-hairpin maneuver, the Pitot-static energy height decreased steadily throughout the maneuver and final energy state was significantly lower than the hairpin. P_s

trended negative throughout the entire maneuver due to the energy penalty of anti-hairpin maneuvers from the wind shear.

Flight test data analysis involved averaging results across the test team. Maneuvers were considered to have been conducted in a shear when the change in wind speed was greater than 1.5 ft/s / 100 ft (0.015 /second) [~0.9 knot/100 feet]. Any wind shear measured below 1 ft/s / ft (0.01 /second) [~0.5 knot/100 feet] was considered a no wind shear condition. The maximum wind shear noted throughout the test program was a shear of 0.04 /second [~2.5 knots/100 feet]. The data points collected during the test window are detailed in Appendix E. Flight Test Results. Data points that were discarded from the averaging analysis method are described in Appendix F. Rational for Discarded Data Figure 72 details the overall results obtained from flight test.

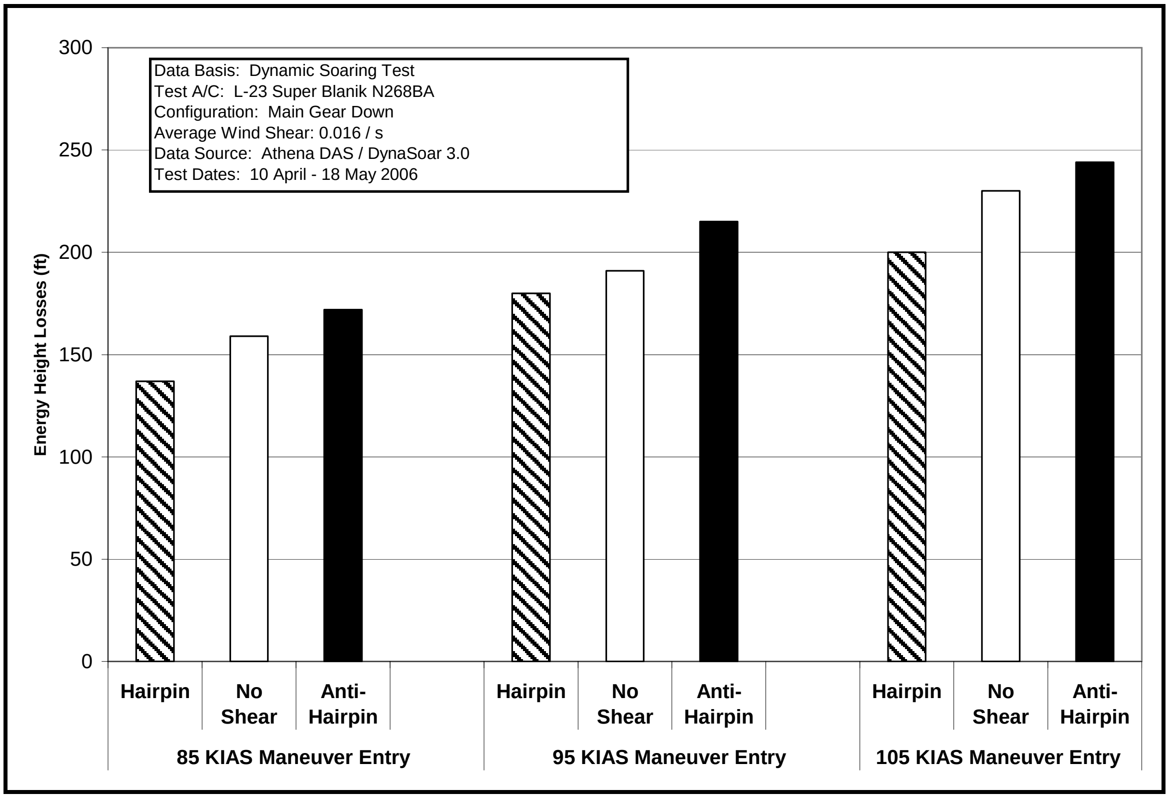

Figure 72. Summary of Flight Test Results

Overall, the flight test results were in accordance with dynamic soaring theory. The energy loss when executing a hairpin maneuver was less than executing the DS FTT baseline maneuver in a no shear condition, on the order of 5-15%. When executing an anti-hairpin maneuver in a wind shear, energy losses were generally 15-20% more than the energy losses from flying the hairpin maneuver in a wind shear.

The Existence of Dynamic Soaring for Full Size Sailplanes

The results presented above revealed that performing the hairpin maneuver in wind shear resulted in less energy loss than performing the anti-hairpin maneuver in wind shear or the DS FTT (baseline) in no shear. The differences in the final total energy states were directly related to the presence of horizontal wind shear. This provided proof of concept that dynamic soaring did exist for full size sailplanes.

Using design of experiments, analysis determined that the Pitot-static specific energy loss was highly dependent on three variables, namely wind shear, entry airspeed, and aircrew flying the maneuver. The flight test program was designed such that it had 99.9 % power to detect any specific energy height differences greater than 10 feet. Analysis determined that there was a linear dependence of energy loss on the wind shear or, stated more simply, that the sailplane extracted energy from the wind shear. The DOE analysis showed greater than 99.9 % confidence that energy changes in the hairpin, baseline, and anti-hairpin maneuvers were related to wind shear. For further DOE explanation see Appendix C. Design of Experiments Analysis.

Notable Case of Dynamic Soaring

Although not included in the formal data analysis due to a lack of precise weather balloon data during the time of flight (reference Appendix F. Rational for Discarded Data **)**, the SENIOR ShWOOPIN test team did execute a dynamic soaring hairpin profile in what was believed to be an abnormally strong wind shear. The flight test crew reported strong turbulence caused by localized wind shears. This wind shear turbulence, much greater than any experienced during the flight test window, was generated by a fast moving cold weather front that passed over Edwards AFB. Although an equipment malfunction prevented the launch of a weather balloon at the time of flight, weather data taken from the NASA SODAR equipment, time stamped approximately one hour after the flight occurred, indicated current wind shear conditions exceeding 0.1 ft/s / ft. This wind shear was more than six times the average wind shear encountered during the test program. Unfortunately, the strong winds generated by the cold front engulfed the test area directly above the Rogers dry lakebed. This cold front generated a large dust storm and made conditions unsafe for continued test flights after this sortie had landed. The energy height data from this flight is shown in Figure 73.

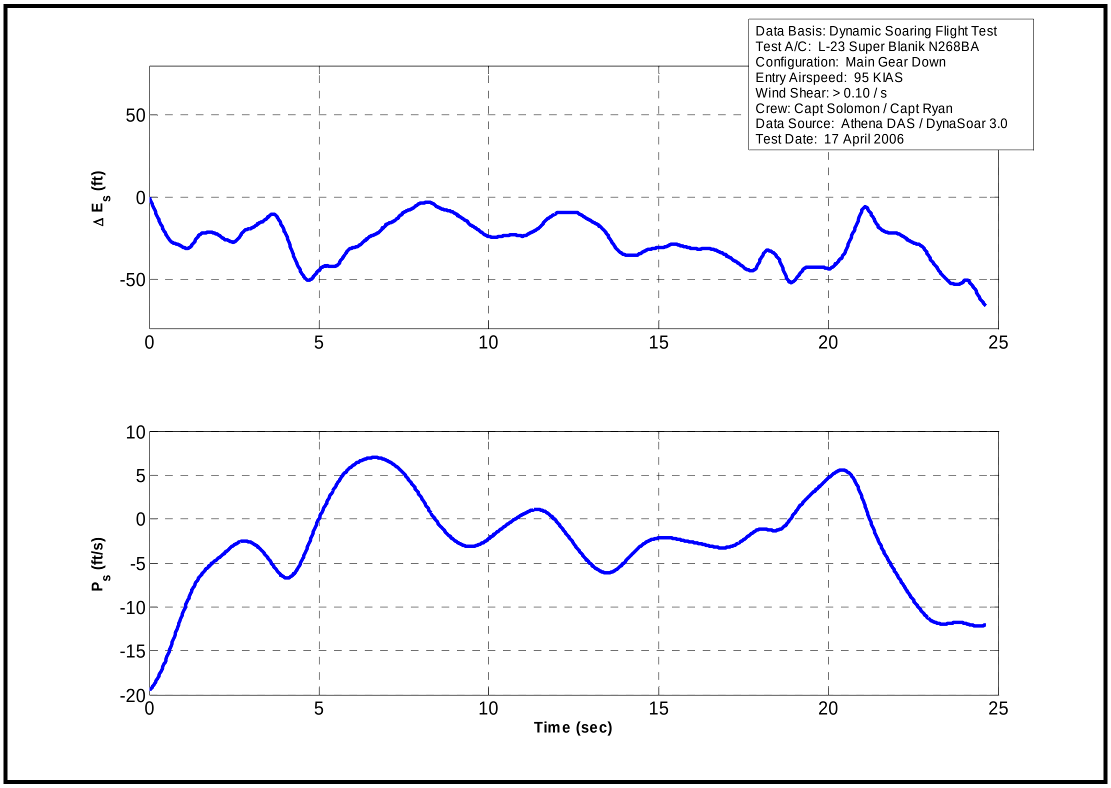

Figure 73. Special Case of Dynamic Soaring

This profile was very unique amongst all the other data flights since it resulted in a loss of only 60 energy height feet. For the majority of the profile, the sailplane actually maintained a neutral to positive energy state. This is extraordinary considering the lack of thermals or orthographic lift. Similar results were obtained when this flight was recreated in the APEX flight simulator with the estimated wind shear. This is shown in Figure 74.

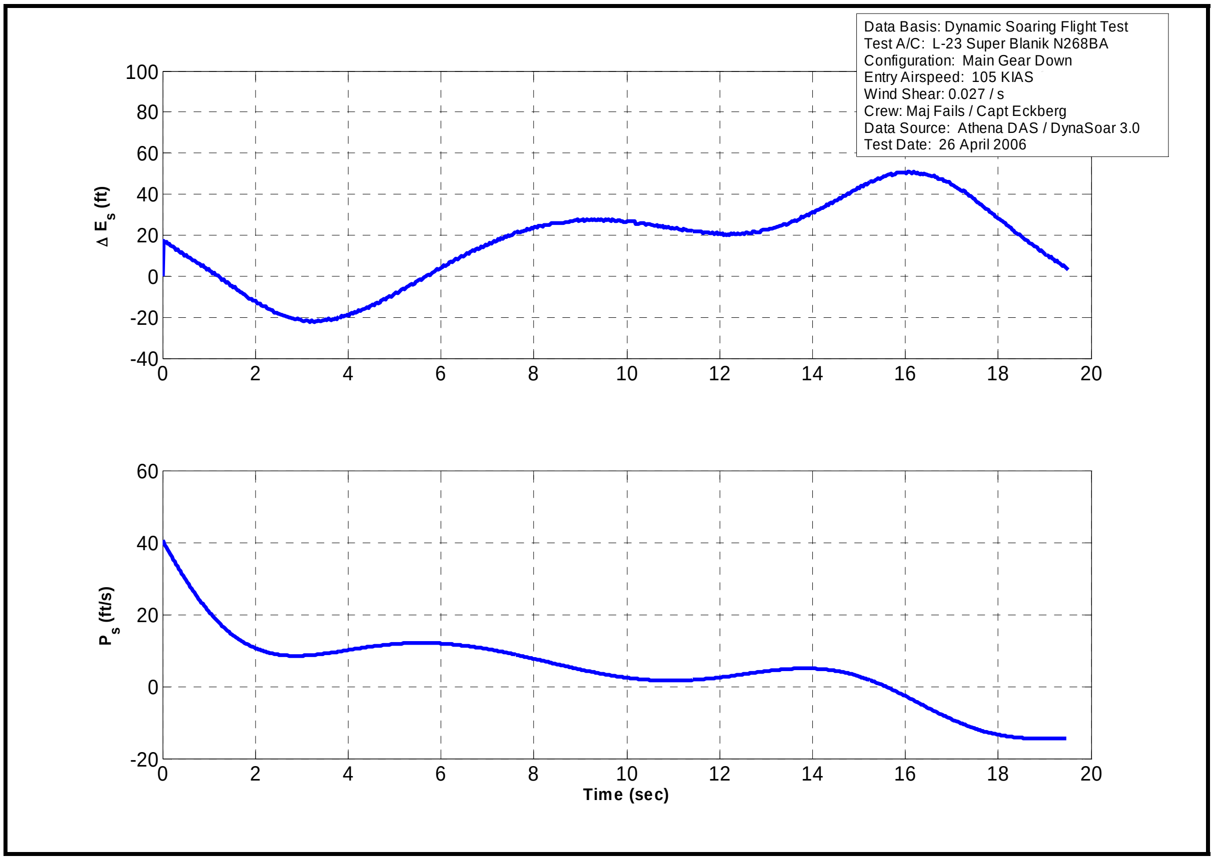

Figure 74. APEX Simulator Recreation of Strong Wind Shear Hairpin

This flight lends further evidence to the existence of dynamic soaring flight for full size sailplanes. It also indicated the need for precise wind data and added credence to the extreme strength of the wind shear required in order to experience near energy neutral profiles in this particular sailplane. This was predicted by dynamic optimization shown in Figure 49.

Comparison of Modeling and Simulation Data Predictions with Flight Test Results

The MATLAB® modified profile and the APEX flight simulator were flown using a wind shear of 0.015 ft/s / ft. This wind shear was chosen since it represented the average wind shear experienced during actual flight test. This provided a realistic basis with which to compare modeling and simulation data against actual flight test. To ensure a sufficient data set, a total of 100 APEX flight simulator runs were documented across the airspeed band using both the hairpin and anti-hairpin maneuvers. The Pitot-static energy height flight test data was averaged across the test team results and compared to MATLAB and APEX simulator predictions. Overall, the MATLAB® dynamic optimization and the APEX flight simulator provided very reasonable predictions of actual flight test energy height data and served as excellent dynamic soaring research tools.

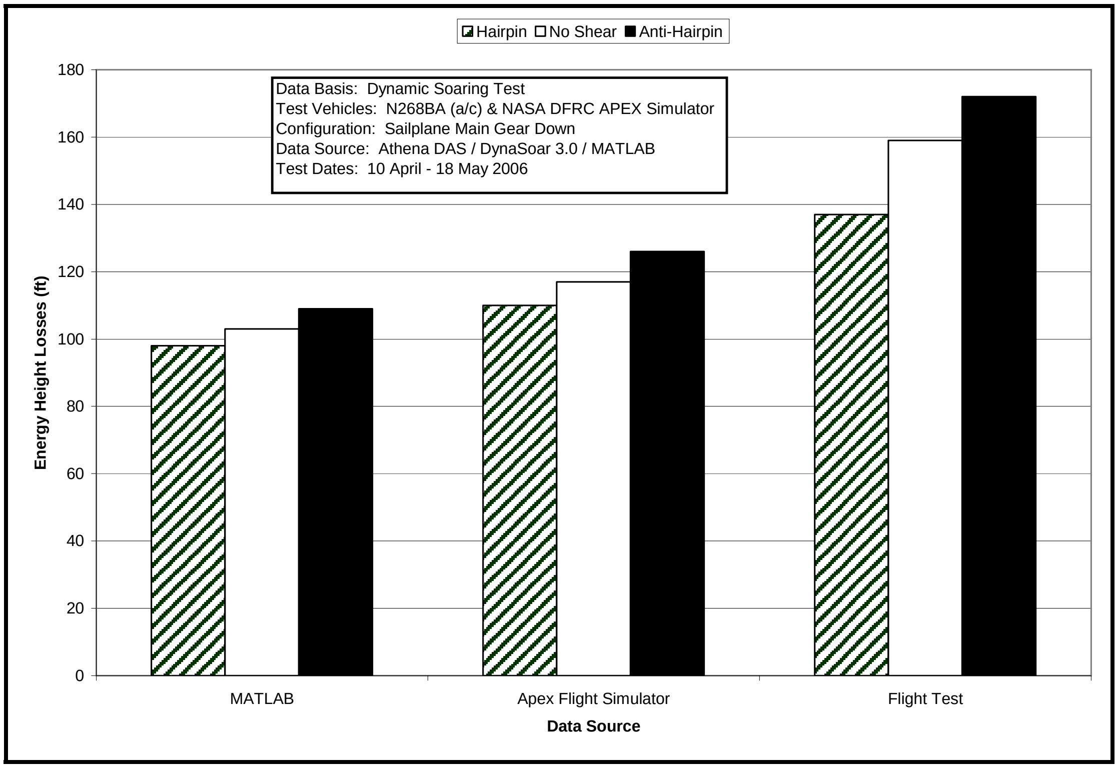

Figure 75. 85 Knot Entry MATLAB / APEX simulator / flight test comparison

For the 85 KIAS maneuvers, as shown in Figure 75, the MATLAB® model and APEX simulator were in close agreement with each other. However, both tools predicted less energy loss, on the order of 30-40 specific energy height feet, than was actually experienced. This was most likely due to the fact that the L-23 drag model was acquired using static techniques *(i.e. without the presence of large control surface deflections, sideslips, or otherwise aggressive maneuvers).* This model would, by definition, produce less drag than what could be expected during an actual dynamic soaring maneuver. Nonetheless, the flight test data indicated that the hairpin lost less energy as opposed to the anti hairpin as predicted by MATLAB® and the APEX flight simulator. Figure 76 shows very similar trends as those described for Figure 75.

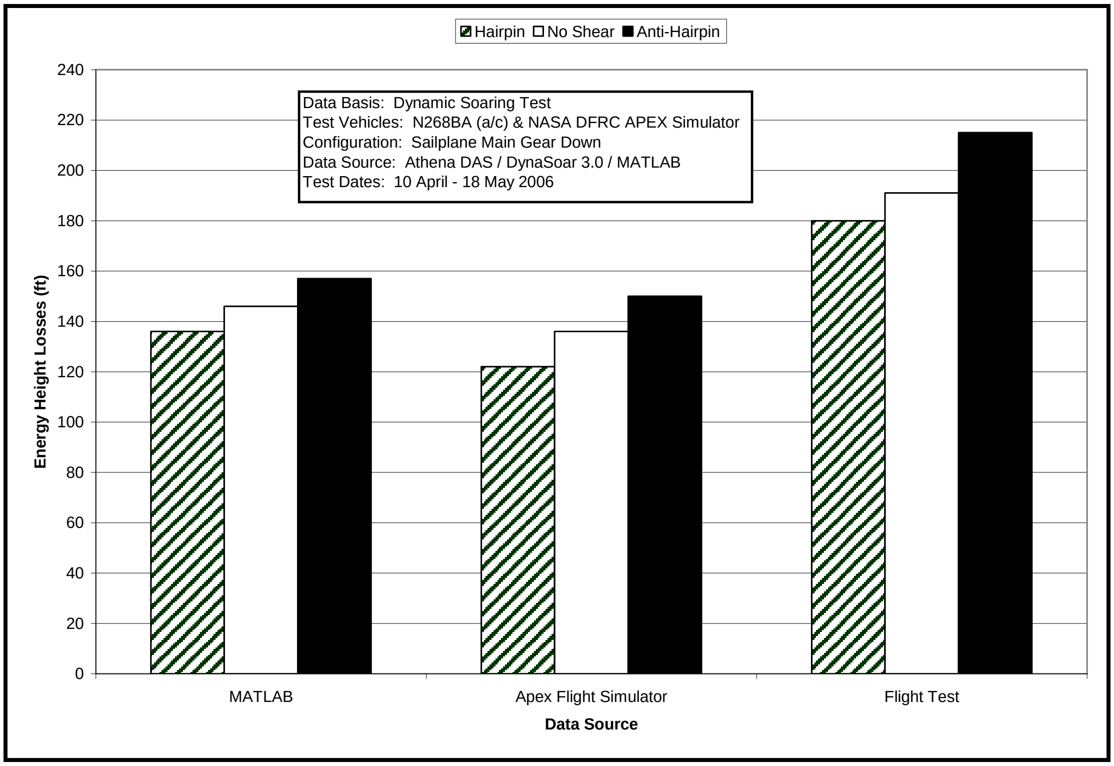

Figure 76. 95 knot entry speed MATLAB / APEX simulator / flight test comparison

Again, the predictions showed the correct trend between the hairpin and anti-hairpin as what was experienced in actual flight test. Once again, the predicted magnitude of the energy heights was less than flight test. These trends are further emphasized by studying Figure 77.

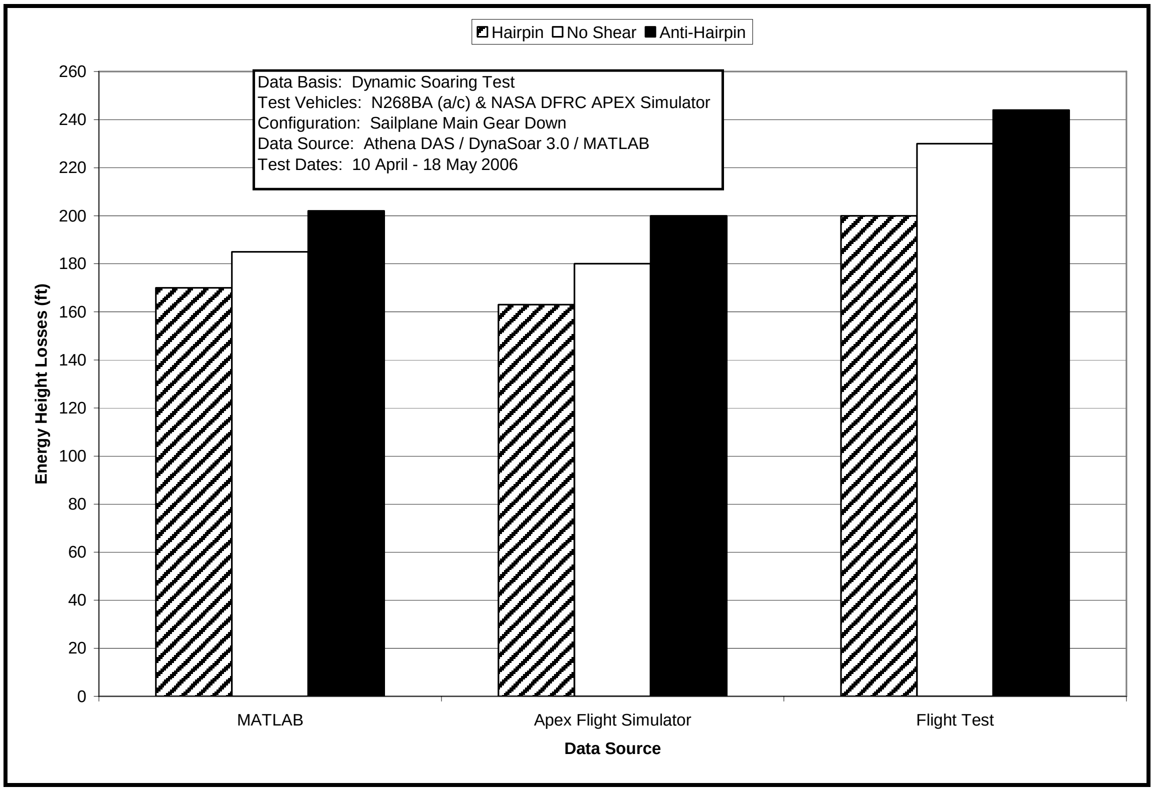

Figure 77. 105 Knot MATLAB / APEX simulator / flight test comparison

Overall, the APEX simulator and MATLAB® model were invaluable in studying dynamic soaring. The model used for both MATLAB® and the APEX simulator assumed a more optimistic drag polar than what the sailplane actually produced. This fact accounted for the consistently smaller predicted energy height losses. The drag polar produced by the SENIOR IDS flight test data were collected for trimmed flight conditions with negligible aileron and rudder deflections. However, during the DS FTT maneuver, the ailerons and rudder were continuously deflected and sideslips were encountered leading to more drag than in the trimmed flight condition. Additionally, the wind shear used in MATLAB® and the APEX simulator was linear with respect to altitude and was known exactly. However, the wind shear in the real world was not always linear, and was not known with the same accuracy. These two factors accounted for most of the differences between the flight test data and modeling and simulation data.

Employment by Soaring Pilots

The dynamic soaring maneuver was evaluated from both a handling qualities and practical employment standpoint. Overall from a handling qualities perspective, the maneuver was relatively easy to fly compared to standard glider maneuvers, *(i.e. steep turns, slow flight, etc)* that a typical soaring pilot would execute. On average, a 2.0 g pull was used to initiate the DS FTT maneuvers at the 95 and 105 KIAS points and 1.5-1.8 g on the 85 KIAS points. The stick and rudder forces and deflections during the maneuver were not objectionable. At no time during the test flights was safe aircraft control in question.

Normal altitude gained during the maneuver ranged from 300-400 feet during the 105 KIAS points to 150-200 feet during the 85 KIAS points. During the test program, several data points were flown at 200 feet AGL and 105 KIAS. Although workload slightly increased at the lower altitudes due to ground rush, performance standards did not suffer and desired performance was still attained. Likewise, control forces and deflections as well as aircraft controllability was never in question at these lower altitudes.

The difficulty of the maneuver to fly was assigned a Cooper-Harper rating based off of the following criteria:

> **Desired:** Maintain pitch and bank to within ±5 degrees of entry, peak, and exit parameters as discussed earlier in the test procedures section. Airspeed must have been maintained within ±5 knots of entry and peak airspeed parameters. At the conclusion of the maneuver, the pilot must have rolled out within ±10 degrees of the initial heading.
>
> **Adequate:** Maintain pitch and bank to within ±10 degrees of entry, peak, and exit parameters as discussed earlier in the test procedures section. Airspeed must have been maintained within -5 to +10 knots of entry and peak airspeed parameters. At the conclusion of the maneuver, the pilot must have rolled out within ±20 degrees of the initial heading.

Figure 78 illustrates the Cooper-Harper Ratings for each test pilot on the test team. The project pilots had diverse flying backgrounds, but the Cooper-Harper Ratings were similar among all the pilots. Pilot 1 was a C-130E pilot, pilot 2 was an F-15C pilot with a commercial sailplane license, and pilot 3 was an AV-8B pilot. Pilots 1 and 3 had no previous glider experience. A level II Cooper Harper rating was assigned by two of the test team pilots and a level I was assigned by the remaining pilot on the test team (See Appendix G. Cooper-Harper Rating Scale). Desired performance was achieved by each team member. However, moderate pilot compensation was required to attain desired performance because of the required precision of the maneuver. Overall, the DS FTT was executed with tolerable pilot workload primarily due to the advanced avionics and maneuver quality assistance provided by the FTEs and the FTNs from the rear cockpit. During the maneuver the FTE/N would call the altitude change from start altitude so the pilot could remove it from his cross check. In addition, the FTE/N was the primary safety monitor for terminating the maneuver due to a low energy state or descending through minimum altitudes during DS FTT maneuvers.

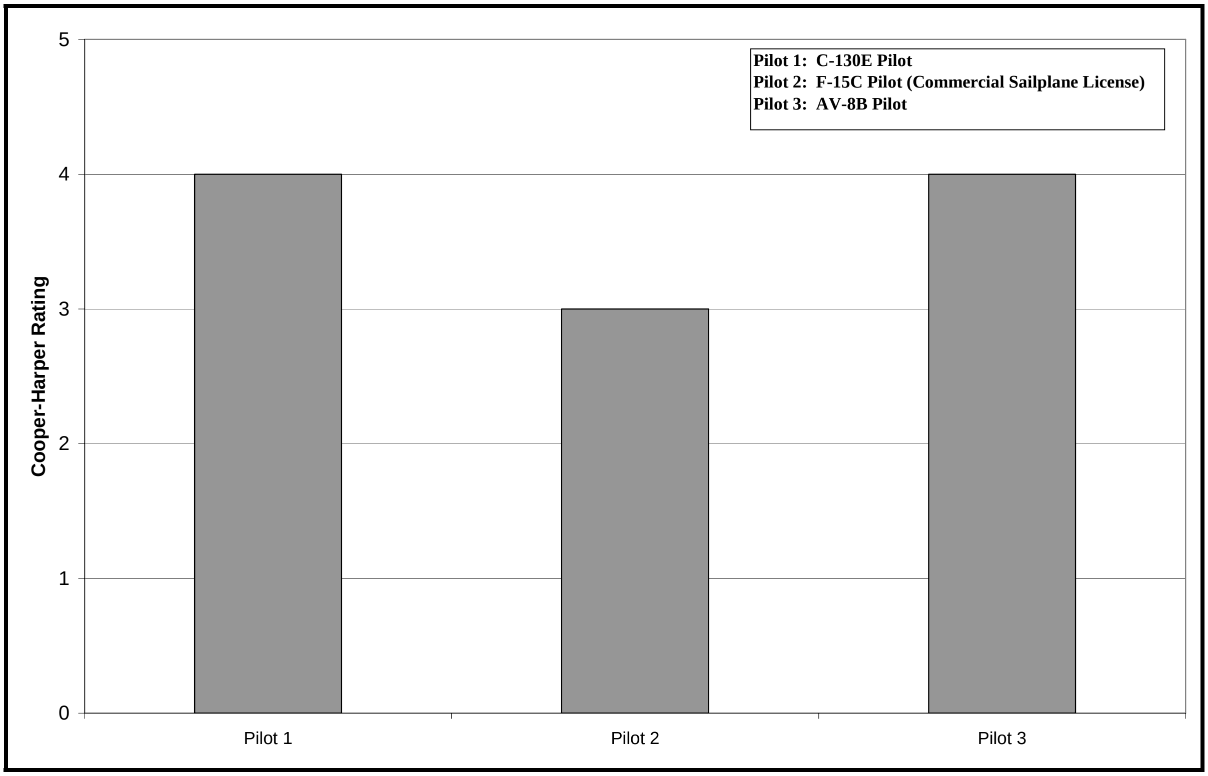

Figure 78. Cooper-Harper Ratings

Overall, the ability to extract energy from horizontal wind shear did exist. However, the data also indicated that the energy gained was relatively small. During the test window, relatively light wind shear profiles were generated by the mild temperature inversion and boundary layer effects experienced in the flight test area. The strongest wind shear encountered during the test window equated to an increase of 2.5 knots per 100 feet. Hence, little energy was available to extract from the wind shear. Although more difficult to map precisely, stronger wind shears can be generated when the wind is partially blocked by an obstacle. This situation exists on the leeward side of mountain ridges and might provide the best opportunity to experience dynamic soaring.

In addition, the L-23 drag penalties incurred due to aircraft design possibly outweighed much of the energy benefit gained during the hairpin maneuvers. The test aircraft L-23 suffered from high parasite drag due to the fixed landing gear, metal rivet construction, and imperfections in the fit of major components (canopy, flight control surfaces, etc). Typical competition sailplanes feature modern glass composite construction and sleek low drag designs. Gaps between canopies and flight control surfaces are typically sealed with tape in order to present a seamless surface to the wind. As a result, competition sailplanes can have lift to drag ratios in excess of 60:1 vice the 24:1 glide ratio of the test aircraft. As a result, low drag sailplanes are better suited for extracting energy via dynamic soaring techniques. A high performance glider, with lower drag, and increased maneuverability, would possibly see an enhanced positive net effect from the dynamic soaring maneuvers in wind shear.

The avionics, test instrumentation included in the glider, and weather support for these flights were invaluable in order to fly accurate maneuvers. The attitude display allowed for accurate and repeatable maneuvers in pitch and roll. In addition, the airspeed and altitude readouts were clear and sensible. Likewise, the GPS moving map display coupled with the hands on stick (HOS) activated ground track symbology maximized the precision to which the DS FTT maneuvers could be flown. These avionics were unique to this aircraft and would not be present in a typical production sailplane. Furthermore, atmospheric data were collected using dedicated weather balloons and mobile SODAR. A typical sailplane pilot would not have access to these resources to accurately map the atmosphere around the sailplane. Strong shears can be felt on tow in the form of turbulence, and temperature inversions can be indicated by low haze or drifting columns of smoke or dust. However, these indications are ultimately only an approximation made by the pilot in the cockpit real time. Hence, maneuver precision and energy extraction from wind shear would suffer in a production sailplane with a typical soaring pilot.

The dynamic soaring maneuver was not difficult to fly given the special instrumentation and crew coordination employed during flight testing for this research. However, level II ratings were assigned due to the precision required in order to standardize data collection. Dynamic soaring theory indicates that it is possible to extract energy from horizontal wind shear using maneuvers other than the DS FTT used for this research. These maneuvers may require less precision in order to be performed and may be able to be executed with a standard sailplane's instrumentation.

Finally, the data indicated that the dynamic soaring maneuver was more beneficial at the high speed points from 95-105 KIAS. In order to obtain these entry speeds in the L-23 from a start airspeed of 60 KIAS, 700-800 feet of altitude were lost during the dive. This is not a realistic profile for a pilot who is trying to maximize glider energy state because it involved sacrificing significant altitude. Since precise wind shear data would not be known, this dive might ultimately result in a loss of energy that may not be recovered. Hence, from an energy height standpoint, hairpin maneuvers in uncertain atmospheric conditions would be risky for a soaring pilot to perform.

In summary, the dynamic soaring maneuver was a relatively mild maneuver that was easy to fly, but the precision required for flight test data collection increased the workload significantly. Valid data were collected throughout testing that proved the theory of dynamic soaring. However, in a production sailplane that lacks specialized instrumentation and detailed atmospheric data, the risk to a sailplane's energy state by performing dynamic soaring maneuvers may be outweighed by the energy benefits gained by basic static soaring techniques, such as thermal, ridge lift, etc.

V. Conclusions and Recommendations

This research represented the first documented study into the viability of dynamic soaring for full size sailplanes. The results from this research will have a direct impact on the design of the next generation of airborne robotic space explorers as well as enhancing flight techniques employed in the sport of soaring. Trajectory dynamic optimization was performed in addition to numerous modeling and simulation trials in specially developed flight simulators. Custom built dynamic soaring electronic flight displays were developed for this research in order to aid flight crews in flying the correct trajectory and to facilitate data acquisition. This research and development created a solid foundation for actual dynamic soaring flight test. As a result, the results from dynamic soaring flight test proved to be very successful as all test points were flown and all objectives were met.

Extensive mathematical modeling and simulation revealed some important dynamic soaring conclusions that were used in the development of flight test techniques and data analysis protocols. The first was that when encountering a wind shear, the sailplane must either climb while facing a headwind or descend while traveling with a tailwind in order to realize an energy benefit. Furthermore, so long as the entry speed into the maneuver was set beforehand, the control inputs and resulting shape of the optimal dynamic soaring profile were relatively unaffected by the strength of the wind shear. Once the shape of the hairpin dynamic soaring profile was known, the anti-hairpin trajectory was its mirror image with respect to the prevailing wind shear direction. These conclusions were important since it meant that the maneuvers were trainable and repeatable to soaring pilots or programmable to an airborne robotic explorer Analysis also indicated that the greatest exchange of energy with the wind shear occurred while the sailplane was climbing or descending through the wind shear layers. The energy exchanged by the turn reversal at the peak of the maneuver was negligible in comparison. In general, higher speeds increase the potential energy gaining performance of the sailplane from the wind shear, but at the risk of incurring increased penalties from induced and parasite drag, increased over-*g* potential, and downrange distance. Based on this conclusion, for the L-23 Super Blanik, entering the dynamic soaring profile at approximately 95 KIAS represented a good compromise between net energy benefit, operational limitations of the aircraft, and downrange distance achieved. Lastly, on the scale of full sized sailplanes, dynamic soaring required strong wind shears and was best achieved by using a blend of moderate to fast entry airspeeds with smooth control inputs to avoid an over-*g*. Overall, this project proved that full size sailplanes could extract energy from horizontal wind shears, although the utility of the energy extraction could be marginal depending on the flight conditions and type of sailplane used. Recommendations for future dynamic soaring research are provided in the next section.

Future Dynamic Soaring Research Recommendations

Future dynamic research projects should focus on addressing four recommendations provided by this project. These recommendations are provided below in order of priority.

Table 7. Summary of Future Dynamic Soaring Research Recommendations

Priority	*Recommendation*
1	**Conduct dynamic soaring research in the stronger wind shears generated by orthographic features**
2	**Conduct dynamic soaring research in high performance sailplanes**
3	**Investigate alternate dynamic soaring maneuvers that require less precision and instrumentation**
4	**Build a dynamic maneuvering drag polar model**

Rationale for Recommendations

Future dynamic soaring research should be conducted in the stronger wind shears generated by orthographic features. Although this project successfully proved the theory of dynamic soaring for full size sailplanes, the amount of energy benefit, from mathematical predictions, flight simulator results, and actual flight test, was relatively small. The strongest wind shear encountered during this test program equated to a 2.5 knot increase per 100 feet of altitude gain. Hence, little energy was available to extract from the wind shear. It is very likely that stronger wind shears than those encountered during this test program could be generated by flying on the leeward side of mountain ridges when the winds are perpendicular to the ridge line. Although these wind shear profiles would be harder to map due to the complexity of the flow fields, this scenario represents the best opportunity to experience suitable dynamic soaring conditions.

Future dynamic soaring research should also be conducted in high performance sailplanes. The low aerodynamic performance of the L-23 sailplane mitigated much of the energy gain realized by flying the hairpin maneuvers in the light wind shears present during the test window. Data analysis and a comparison of the flight test with dynamic optimization results and APEX simulator data indicated that more energy could be extracted from the atmosphere with stronger wind shears and low drag profile sailplanes. Data analysis further indicated that faster entry speeds were ideal for dynamic soaring since this allowed the sailplane to penetrate higher through the wind shear. At these higher speeds, however, parasite drag dominates the performance of the L-23 sailplane.

Future research should also investigate alternate dynamic soaring maneuvers that require less precision and instrumentation. Because of the ground breaking nature of this flight research and the limitations of the environment and sailplane described above, accurate knowledge of atmospheric wind shear conditions and precise control of the dynamic soaring maneuvers were critical. Such precision was required in order to best position the sailplane to take advantage of the wind shear and to ensure the repeatability of the maneuvers. This required advanced custom built avionics and dedicated weather monitoring support. The required precision generated additional workload for the aircrew since they had to constantly monitor the position and strength of the wind shears and use the electronic displays to track the sailplane's attitude and flight condition within tight tolerances through the dynamic soaring flight test technique. Since this project proved the basic existence of dynamic soaring for full size sailplanes, future research should expand the practical knowledge base of this technique by discovering maneuvers that require less instrumentation and precision to successfully extract energy from horizontal wind shears. Maneuvers of this type would be much easier for a typical soaring pilot to perform in a sailplane equipped with standard avionics.

Finally, future research should develop a dynamic maneuvering drag polar to aid in modeling and simulation efforts. The MATLAB® dynamic optimization routine and APEX flight simulator were excellent research tools to study the effects of dynamic soaring in various wind shears. The model used for both tools, however, featured a non-maneuvering drag polar. Although the predicted energy height results from modeling and simulation closely matched the basic trends of flight data, the predicted energy losses were consistently less than flight test energy losses. Essentially, the flight simulator predicted better dynamic soaring performance than what was attained by the L-23.

Bibliography

1. Aviv, Yam-Shahor, et al. *USAF TPS L-23 Super Blanik Aerodynamic Determination, Evaluation, and Reporting Program*, Test Management Project, AFFTC-TIM-05-08, Edwards AFB, California, December 2005.

2. Bryson, A.E. Jr. *Dynamic Optimization*. Addison Wesley Longman, Inc., Menlo Park, CA, 1999.

3. Borror, Sean, et al. *USAF TPS L-23 Super Blanik Drag Polar and Preliminary Investigation of Dynamic Soaring*, Test Management Project, AFFTC-TIM-04-04, USAF TPS, Edwards AFB CA, June 2004.

4. Boslough, Mark B.E. *Autonomous dynamic soaring Platform for Distributed Mobile Sensor Arrays*, SAND2002-1896, Sandia National Laboratories, Albuquerque NM, 2002.

5. Circling Hawk Paragliding. www.circlinghawk.com/crazybirds.html

6. Civil Air Patrol National Technology Center. https://ntc.cap.af.mil/ops/DOT/school/NCPSC/GliderNCPSC/CAPF_5_glider/soaringtechniques.htm

7. Experimental Aircraft Association. http://www.eaa.org

8. FAA (U.S. Department of Transportation Federal Aviation Administration). *Airplane Flying Handbook*. FAA-H-8083-3A, Oklahoma City OK, 2004.

9. Fiddlers Green. http://www.fiddlersgreen.net/index.php?pg=956

10. Gordon, Randel, et al. *USAF TPS L-23 Shear Wind Observed Optimized Path Investigation for NASA*, Test Management Project, AFFTC-TIM-06-02, Edwards AFB CA, June 2006.

11. Hoppi's Segelflug-seiton. http://www.alpenstreknsegelflug.de/texte/english/glidingvideos.htm

12. Invention Psychology. http://invention.psychology.msstate.edu/i/Lilienthal/Lilienthal.html

13. Jackson, Michael R., Zhao, Yiyuan J., and Slattery, Rhonda A. *Sensitivity of Trajectory Prediction in Air Traffic Management*. Journal of Guidance, Control, and Dynamics, 22(2), 219-228, 1999.

Bibliography (Cont.)

14. Larson, Reid A., Mears, Mark J, and Blue, Paul A. *Path Planning for Unmanned Aerial Vehicles to Goal States in Operational Environments*. AIAA Infotech@Aerospace Conference, Arlington, Virginia, September 2005.

15. Leonardo. http://www.leonardo.net/

16 LET. *L-23 Super Blanik Sailplane Flight Manual*. Do-L23.1012.5, Czech Republic, December 1993.

17. Lord Rayleigh. *The Soaring of Birds,* Nature, 27, 534-535, 1883.

18. Library of Congress. http://memory.loc.gov/ammem/wrighthtml/wrightphot.html

19. Lissaman, Peter. *Wind Energy Extraction by Birds and Flight Vehicles*. AIAA Aerospace Sciences Meeting and Exhibit, Reno, Nevada, January 2005.

20. Meriam, J. L., and Kraige, L. G. *Engineering Mechanics, Volume 2, Dynamics*, Second Edition, John Wiley & Sons, Inc., New York, NY, 1986.

21. NASA Dryden Fight Research Center. http://www.dfrc.nasa.gov

22. Physics and Advanced Technologies. http://www-pat.llnl.gov/Research/scattering/LordRayleigh.html

23. Reichmann, Helmut. *Streckensegelflug*, 1978. Reprinted as *Cross Country Soaring* by the Soaring Society of America, 1978.

24. Short, Simine and US Soaring Teams. *History of Gliding & Soaring*, Soaring Society of America, 2004.

25. Vintage Sailplanes. http://vintagesailplanes.de/REIHER.HTM

26. Zhao, Yiyuan J. *Optimal Patterns of Glider Dynamic Soaring*. Optimal Control Applications and Methods, 25, 67-89, 2004.

Appendix A. Instrumentation and Displays Sensors

The instrumentation system installed on the L-23 consisted of an Inertial Measurement Unit (IMU), an air data probe and transducers, control surface position transducers, analog-to-digital converter, a temperature probe and two tablet PC displays. The IMU and analog-to-digital converter were mounted on an adjustable plate and aligned with the centerline of the aircraft. The centerline was defined by the rib running along the top surface of the aft fuselage. The plate was then tilted to align it with the aircraft fuselage reference line. The fuselage reference line was defined by two marks on the side of the glider at the forward and aft ends. The plate was tilted left and right to align with the leading edge of the wing. Finally, a laser sight was used to align the air data probe with the fuselage reference line and center it along the aircraft centerline. All angular measurements were therefore referenced to a body axis coordinate system whose x-axis was aligned with the fuselage reference line and a y-axis aligned with the wing leading edge at the root.

Guidestar GS-111m

An Athena Controls Guidestar 111m (GS-111m) inertial measurement unit (IMU) served as the central component in the instrumentation system. The GS-111m used accelerometers, angular rate sensors, GPS, and a magnetometer to compute a full inertial attitude solution. Pitot-static pressures from a nose-mounted 5-hole probe were measured by the GS-111m to determine airspeed, altitude, angle-of-attack (AOA), and angle-of-sideslip (AOS). Pressure transducers on the TPS GS-111m had a dynamic range of ±26,221.9 Pascals for AOA and AOS, and 16,596 Pascals for dynamic pressure. Total air temperature was measured by a resistive temperature detector (RTD) mounted under the right wing. The RTD voltage was sampled by a 14 bit analog-to-digital input on the GS-111m. Data were sampled and written to a 32 Megabyte onboard memory chip for post-flight download. The GS-111m updated its navigation solution at 50 Hertz. The data sampling rate was software selectable with currently available rates of either 25 Hertz or 50 Hertz. The 50 Hertz sampling rate was used for this program. The GS-111m was modified to accept a digital signal from an analog-to-digital converter that was wired to the position transducers. This hardware modification consisted of a circuit board housed in a generic black box that could be mounted anywhere in the proximity of the GS-111m and connected to the GS-111m using an RS-232 serial cable. The interface control document can be obtained from Athena Controls. A full description of the GS-111m can be obtained by contacting Athena Controls.

Air Data Probe

An air data probe purchased from Computer Instruments Corporation was used to measure static pressure, total pressure, AOA, and AOS. The initial design called for a constant 0.75 inch outer diameter probe. This was modified by increasing the diameter of the aft end up to 1.25 inches to provide sufficient wall thickness for attachment to the boom. The AOA and AOS measurements were made using a pressure differential, total pressure, and a scale factor. The probe had a scale factor of 4.526366 1/radian. During a previous project the air data probe was calibrated using a trailing cone (reference 1).\

Resistive Temperature Detector

The RTD purchased from Computer Instruments Corporation was used to measure total temperature. The platinum RTD had a nominal resistance of 500 Ohm and a scale factor of

0.00385 Ohms/Ohm/degrees C. The RTD was powered by an Action Instruments Ultra Slimpak G418-0001. A full description of this device may be obtained by contacting Computer Instruments Corporation. The output voltage of the RTD was sampled by a 14 bit analog-to-digital converter on the

GS-111m. During a previous project an ice bath calibration of the RTD connected to the GS-111m resulted in the following relationship between RTD resistance and measured voltage:

$$R\_RTD = 474.0085 \text{ Ohm} + 61.6398 \text{ Ohm/volt} * \text{Voltage} \tag{72}$$

A platinum RTD had a sensitivity curve with a slope of 0.00385 Ohms/Ohm/degrees C over the temp range [-10 +50] degrees C. This gave a relationship between RTD resistance and temperature:

$$T(°C) = -257.3989 \text{ C} + 0.5148 \text{ C/Ohm} * R\_RTD \tag{73}$$

Combining these equations gives a relationship between voltage measured by the IMU and total air temperature:

$$T(°C) =(0.5148 * (474.0085 + (\text{Voltage} * 61.6398))) - 257.3989 \tag{74}$$

Surface Position Transducers

String potentiometers (5K Ohm) made by Space Age Technologies were mounted to measure control surface deflections of the elevator, rudder, left and right aileron and elevator trim tab cable. The potentiometers were mounted in front of the surfaces and connected to the surface with a steel cable. Wiring to the potentiometers was run internally from the DAS pallet to the mounting point for the potentiometer. During a previous project calibration curves were created using a digital inclinometer to measure the angle of the control surface and plot it versus the voltage output for the elevator, ailerons and trim tab. Calibration of the rudder was accomplished by finding the center of rotation on the top of the rudder. A protractor was then placed above this point and deflection angles were read using the seam of the rudder that described the left-right plane of symmetry. All control surface calibration curves were linear.

GS-111m Interface

Interface to the GS-111m was made via five serial ports accessible through 51 pin connectors. Each serial port was configured for RS-232 communication at 115.2 Kilobits/second. The slow data rate was chosen primarily to ensure reliable communication with the Motion Computing tablet PC used for cockpit data display. Operationally, only ports 1-3 were used.

Laptop PC Interface

Serial port 1 was used to interface with a laptop PC for IMU initialization. After applying power to the IMU, an Athena Graphical User Interface (GUI) was used to set internal IMU parameters and switch the IMU into the Air Mode. After initialization, the laptop was disconnected prior to flight.

Tablet PC

Serial port 2 was used to communicate with a Motion Computing tablet PC. The tablet PC displayed flight parameters in the cockpit (see Figure A-1) and had the capability to start and stop data logging via a HOS controls. The tablet PC in the front cockpit was connected to the GS-111m using a serial to USB connector cable. Data from the tablet PC in the front cockpit were passed to the tablet PC in the rear cockpit via an Ethernet cable.

Point-to-Point Protocol Terminal

Serial port 3 was configured for a point-to-point protocol (PPP) connection to a PC. The port speed was set by Athena Controls to be 115.2 Kilobits/second. The port was used to download test data to a laptop using WS-FTP 6.0 software. The data were transferred simply to empty the memory of the GS-111m for the next flight.

Data Acquisition

The list of parameters written to memory on the GS-111m was software programmable, but required support from Athena to perform. Reconfiguring the GS-111m could be accomplished with a simple spreadsheet based program which produced a configuration file that must be downloaded to the unit. A 50 Hertz recording rate was used. Data logged by the Guidestar was saved in time and date tagged files using the convention: INSmmmddhhmmssyyyy. The TPS customized data stream occupied frame 4 as listed in the serial interface spec addendum and took 128 bytes. At 50 Hertz, data frame 4 consumed 3.125 Kilobytes/second. In addition to frame 4, the following frames were stored to onboard memory: Frame 2 at 1 Hertz = 173 bytes/second, Frame 3 at 10 Hertz = 740 bytes/second, Frame 8 at 50 Hertz = 1650 bytes/second.

In addition to the data recorded on the GS-111m the tablet PC recorded data in .bin and .csv file formats. File recording was controlled using the HOS control on the stick in the front cockpit. The first time this button was pushed started recording data while simultaneously zeroing the maneuver downrange and cross range distance and altitude. The next time the button was pushed the file was stopped and logged to the tablet PC using the following naming conventions: TPSmmddyyyy hh_mm_ss.bin and TPScalcmmddyyyy hh_mm_ss.csv. Because the tablet PC offered a simpler interface it was used as the primary data acquisition system, and the GS-111m was only used as a backup data source in case the tablet PC failed to record (this never happened).

Appendix B. Sample Flight Test Dynamic soaring Results

The Athena data acquisition system recorded the sailplane inertial velocities (North/East/Down), inertial positions (North Position/ East Position/Down Position), Euler rates (P/Q/R), and Euler angles (θ/Φ/ψ) through a blended GPS/INS navigation solution. A standard coordinate transformation matrix was then used to convert inertial velocities to body fixed velocities (U/V/W) assuming a flat non-rotating Earth reference frame. This assumption was valid due to the slow speed of the sailplane, and the short time frame and size of the maneuver with respect to the earth's surface. Indicated airspeed was recorded from the test Pitot-static boom via a calibrated transducer. Pitot-static and geometric energy heights were recorded on the Tablet PC via algorithms pre-programmed into the DynaSoar 3.0 software avionics package. All data was automatically logged individually per maneuver by date and time on the Tablet PC in the form of a Microsoft Excel spreadsheet and a .bin file. The .bin file was used to replay the sortie on the DynaSoar 3.0 display for post flight analysis. The excel spreadsheet was imported into MATLAB® and filtered through a first order low-pass Butterworth filter in order to eliminate high-frequency noise while still preserving the fidelity of the raw data. The resulting data file was then plotted and archived for analysis. An example plot set of a typical dynamic soaring maneuver is provided below reference

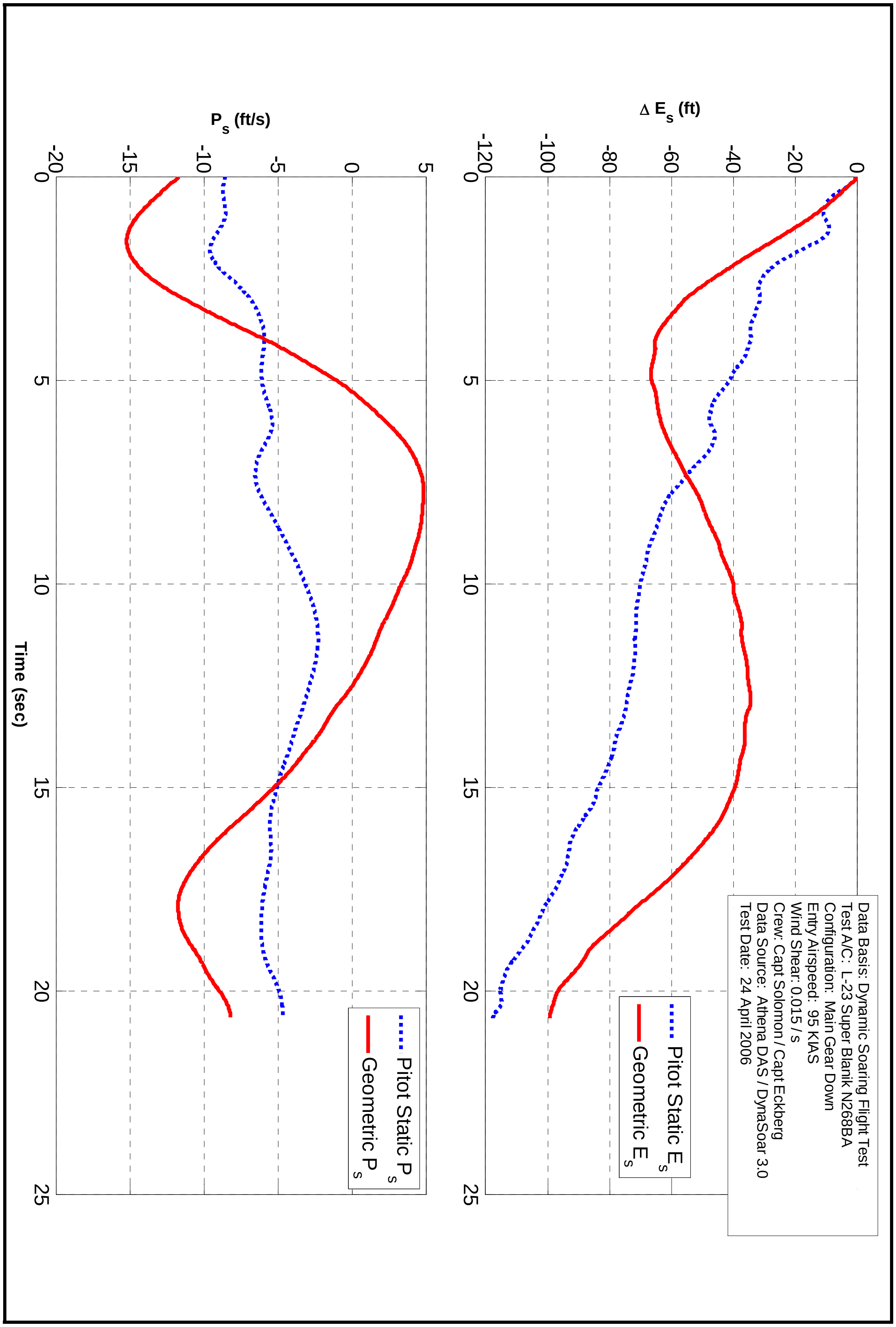

Figure 79. Sample Plot of Pitot-static and Geometric Energy

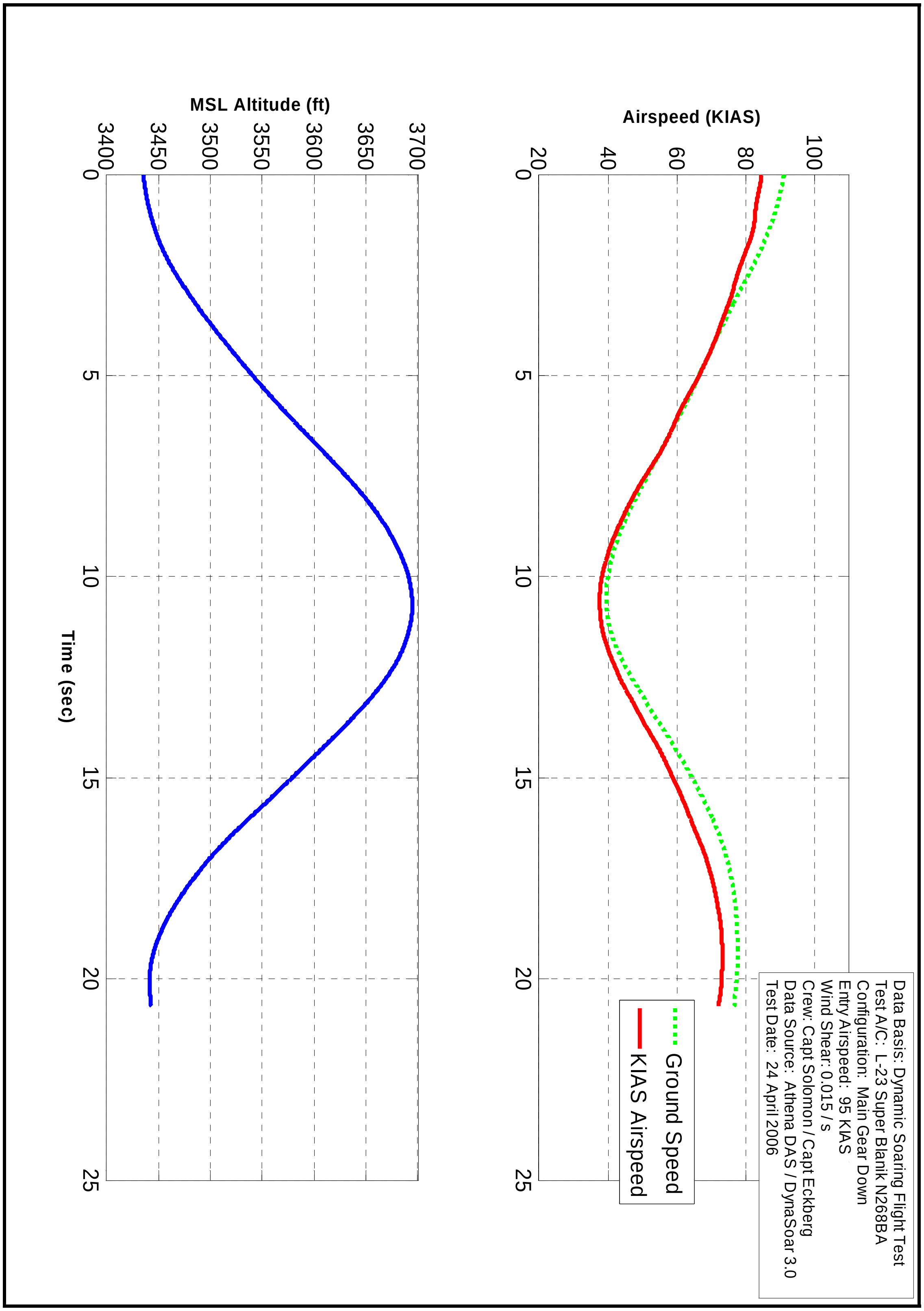

Figure 80. Sample Plot of Indicated Airspeed, Ground Speed, and Altitude

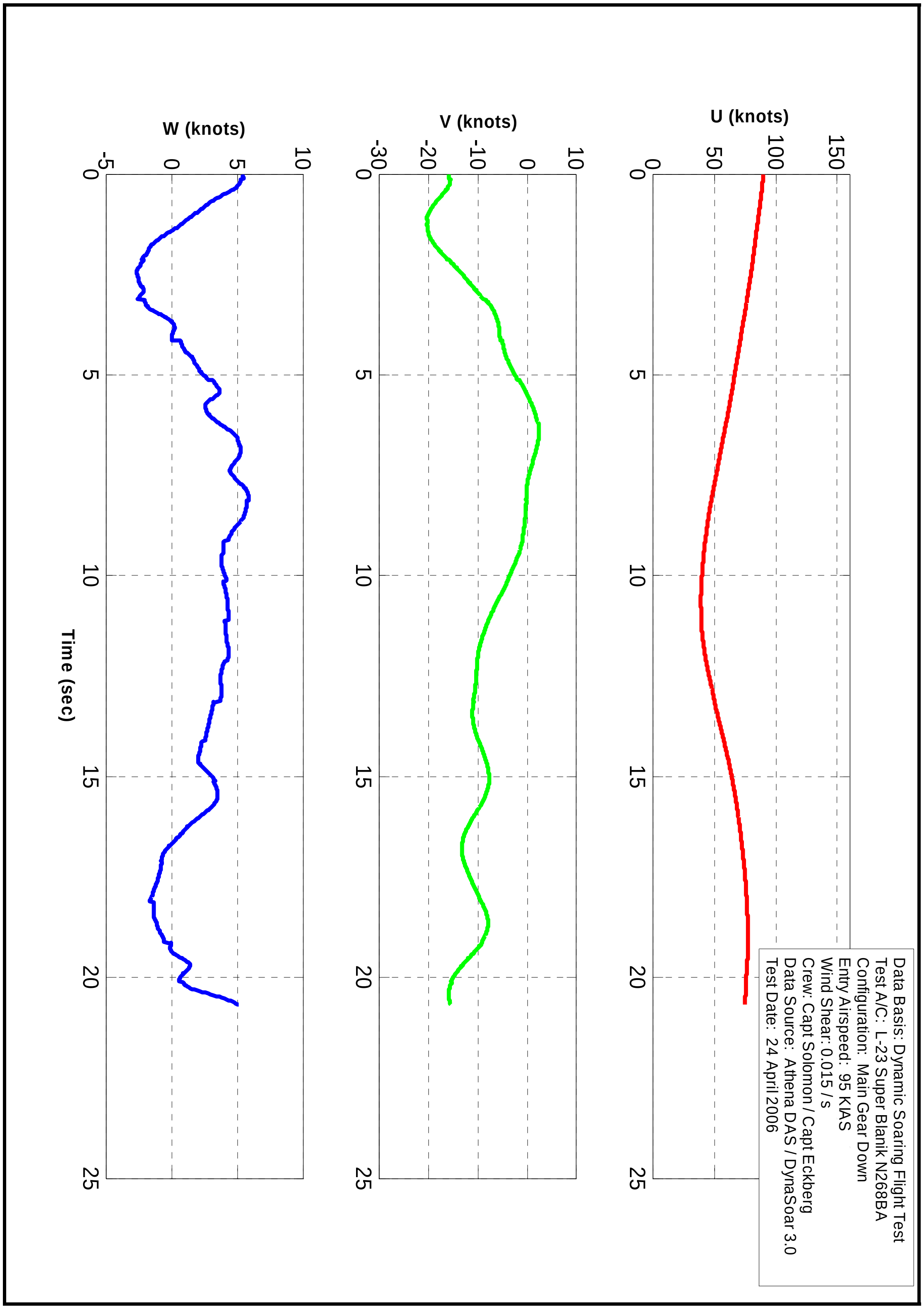

Data Basis: Dynamic Soaring Flight Test
Test A/C: L-23 Super Blanik N268BA
Configuration: Main Gear Down
Entry Airspeed: 95 KIAS
Wind Shear: 0.015 / s
Crew: Capt Solomon / Capt Eckberg
Data Source: Athena DAS / DynaSoar 3.0
Test Date: 24 April 2006

Figure 81. Sample Plot of Body Fixed Velocities

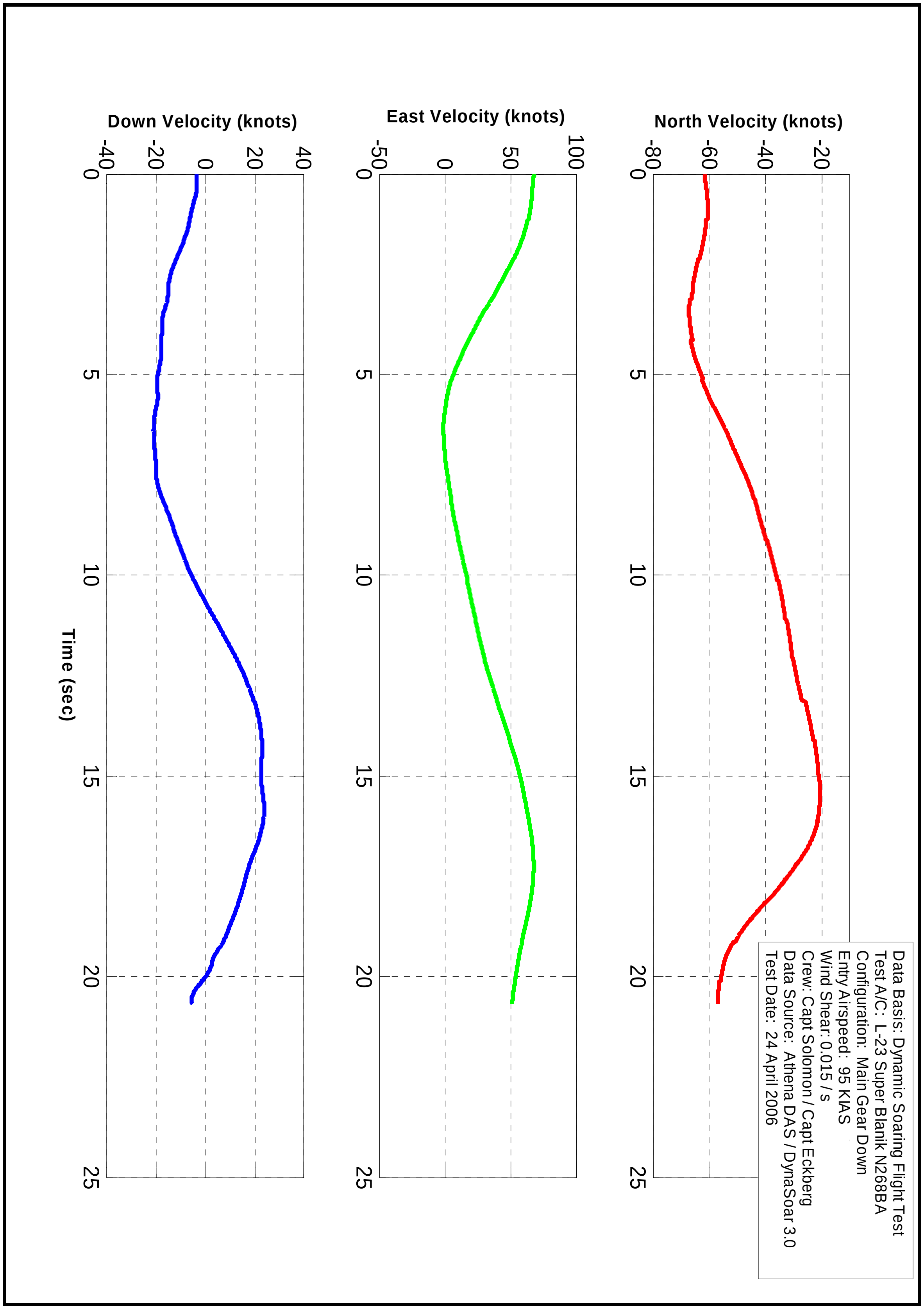

Data Basis: Dynamic Soaring Flight Test
Test A/C: L-23 Super Blanik N268BA
Configuration: Main Gear Down
Entry Airspeed: 95 KIAS
Wind Shear: 0.015 / s
Crew: Capt Solomon / Capt Eckberg
Data Source: Athena DAS / DynaSoar 3.0
Test Date: 24 April 2006

Figure 82. Sample Plot of Inertial Velocities

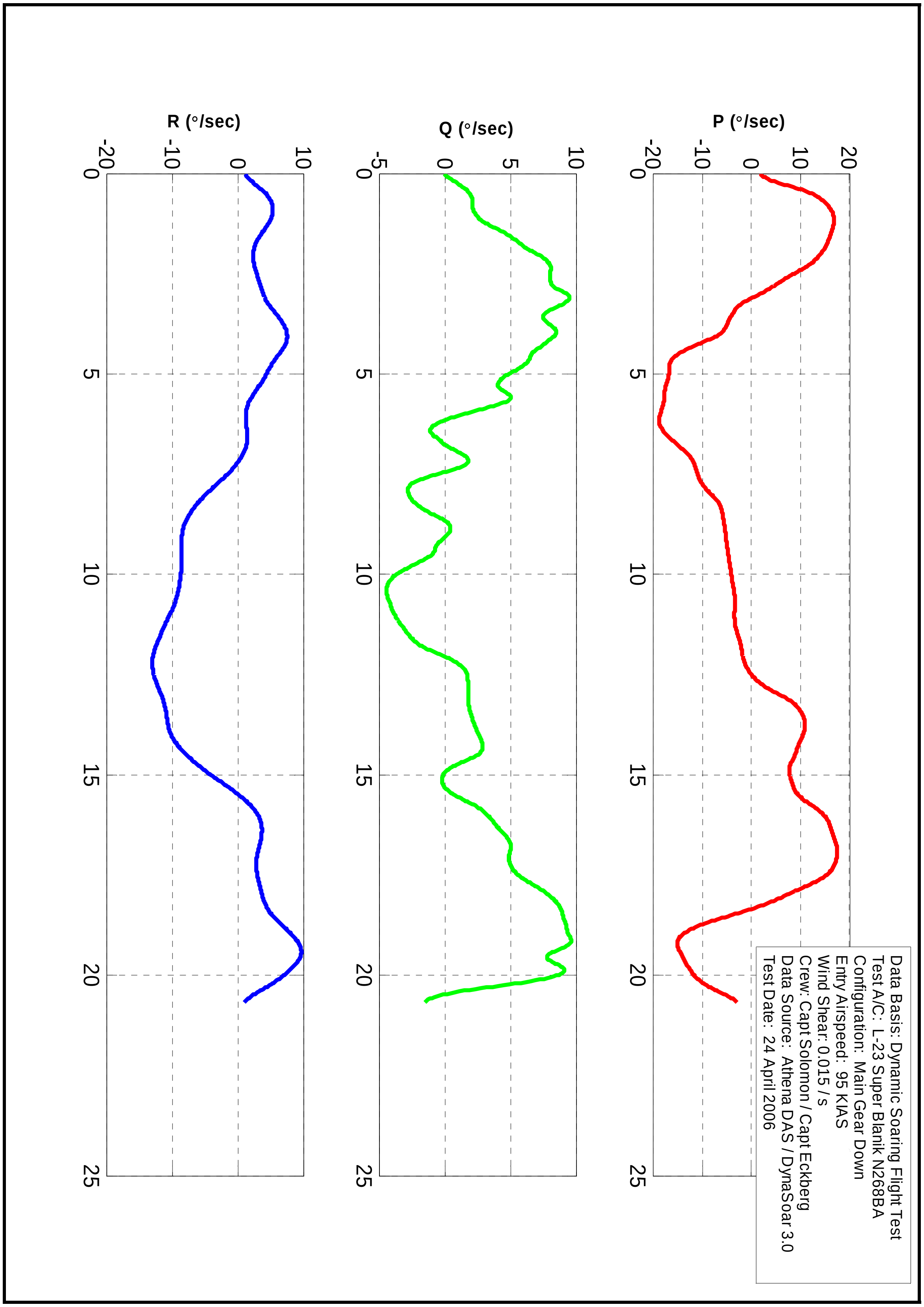

Data Basis: Dynamic Soaring Flight Test
Test A/C: L-23 Super Blanik N268BA
Configuration: Main Gear Down
Entry Airspeed: 95 KIAS
Wind Shear: 0.015 / s
Crew: Capt Solomon / Capt Eckberg
Data Source: Athena DAS / DynaSoar 3.0
Test Date: 24 April 2006

Figure 83. Sample Plot of Euler Angle Rates

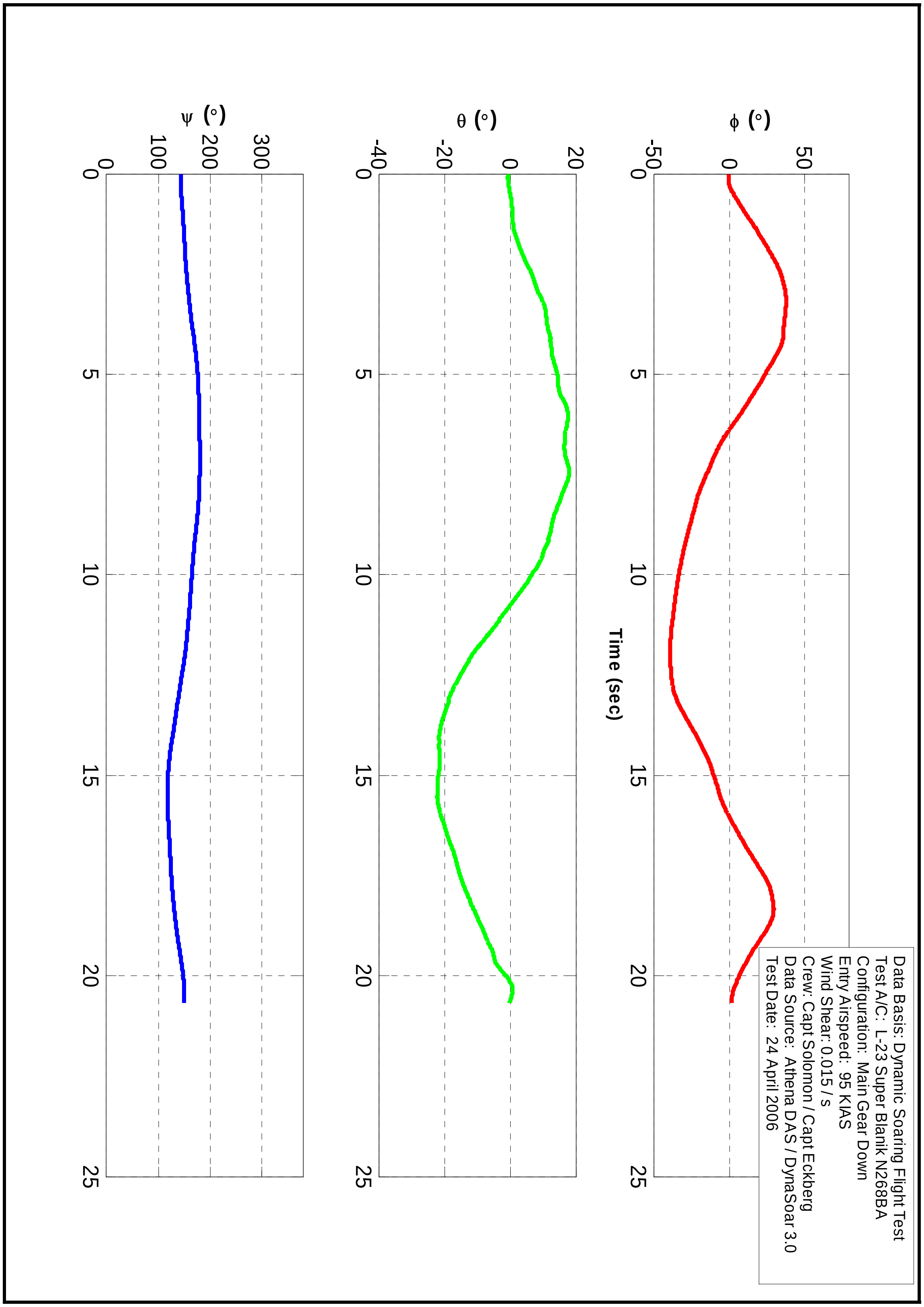

Figure 84. Sample Plot of Euler Angles

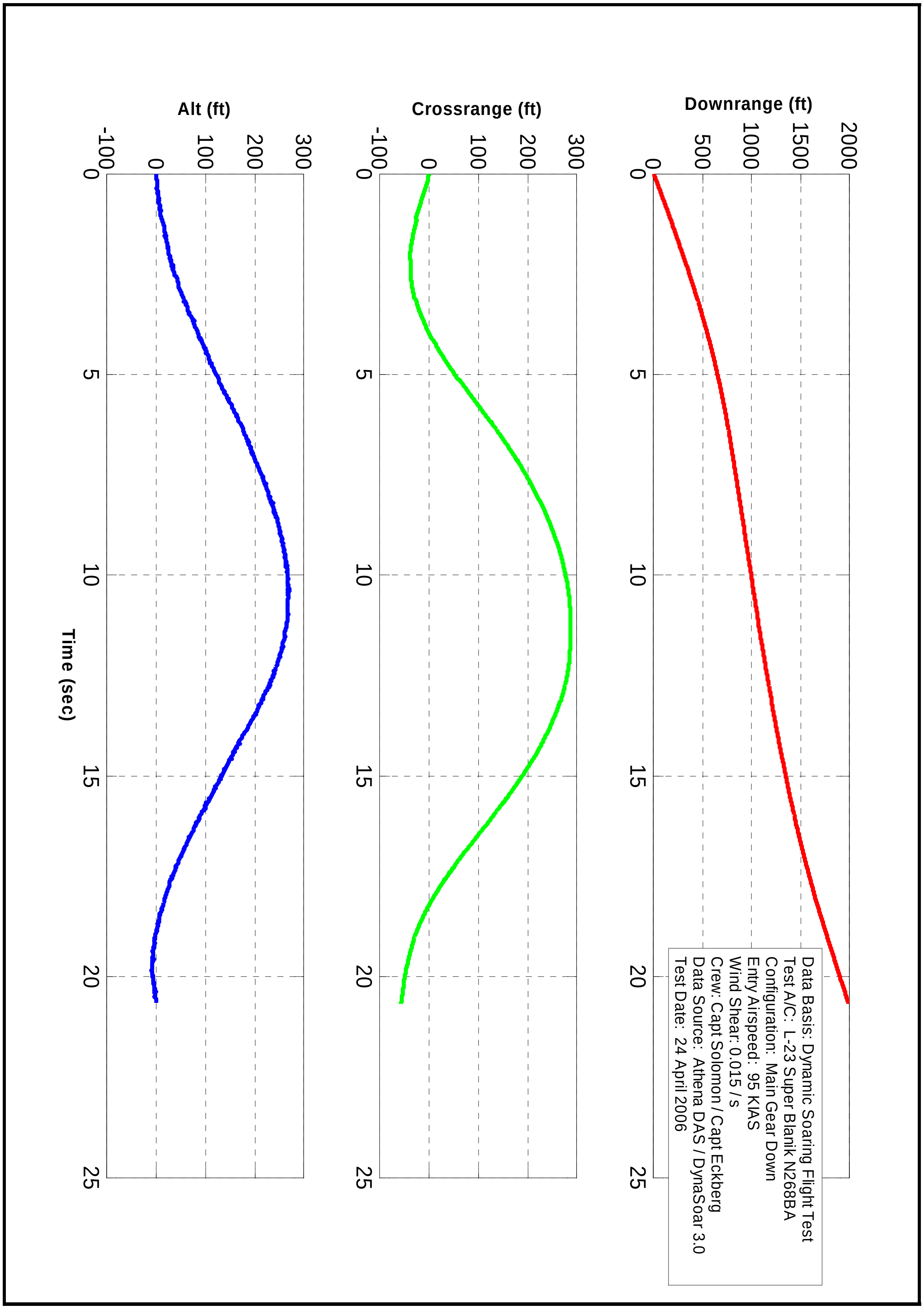

Figure 85. Sample Plot of Inertial Position Relative to Maneuver Point

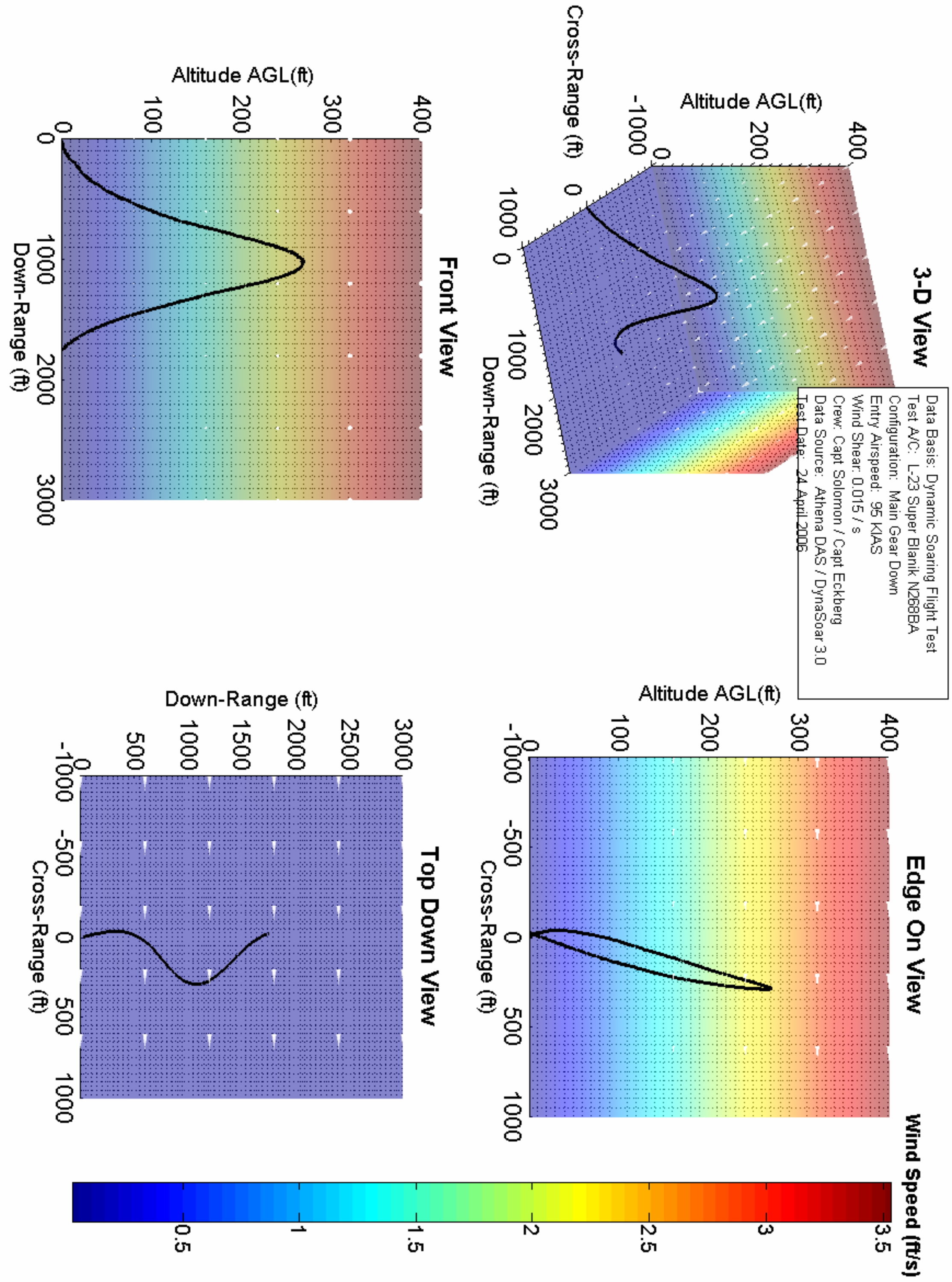

Figure 86. Sample Plot of Sailplane Ground Track and Altitude

Appendix C. Design of Experiments Analysis

Design of experiments statistical analysis was used to determine interactions between all the controllable and uncontrollable factors. The controllable factors were pilots, entry airspeed, and maneuver type. The predominant uncontrollable factor was wind shear. The following table shows the factors considered and their possible values.

Table 8. DOE Factors Considered

Factors	Values
Pilots	-1 (Pilot 1), 0 (Pilot 2), 1 (Pilot 3)
Entry Airspeed	-1 (85 KIAS), 0 (95 KIAS), 1 (105 KIAS)
Maneuver Type	-1 (Anti-hairpin), 1 (Hairpin)
Wind Shear	Variable (-0.009/sec to 0.040/sec)

The following factors and interactions were considered for the model: wind shear, wind shear squared, entry speed, entry speed squared, wind shear × entry speed, wind shear × entry speed squared, wind shear squared × entry speed, and wind shear squared × entry speed squared.

After analyzing the effects and interactions of these factors four primary effects were declared active by the DOE analysis. The magnitude of these effects is shown in Table C-2. The pilot factor was treated as a block effect, which means the only effect of the pilot was to move the model up or down, but not affect the slope. Pilots could not interact with other factors. Entry airspeed was designed as a factor, but analyzed as a continuous variable (or covariate), as some variation occurred in targeting the airspeeds. For the purposes of the DOE analysis an anti-hairpin maneuver was considered the same as a hairpin maneuver in a negative wind shear (i.e. wind speed decreasing with altitude). As maneuver type was used to apply a sign to the wind sheer, it does not appear in the ANOVA table as an active effect.

Table 9. Pitot-static Energy Model Statistics

	Model Value	-95% Confidence	+95% Confidence	F	p-value
Mean	-160.2	-166.9	-153.4	2213.1	0.0000
Wind Shear	557.3	336.5	778.1	25.0	0.0000
Speed	-3.8	-4.3	-3.3	263.8	0.0000
Speed^2	-0.09	-0.18	-0.003	4.2	0.0433
Pilot 1,3	8.6	3.7	13.6	13.8	0.0000
Pilot 2	-16.1	-22.2	-9.94	13.8	0.0000

The p-value indicates the alpha error (confidence equals 1 - α-error), which is the probability of a false positive. That is, saying that something happened, when in actuality it occurred by chance. So, in plain speak, there is a 1 in 20 chance that these dynamic soaring maneuvers will show the entry speed squared impacts the difference in energy height lost when it actually does not have an impact. Likewise, the F-ratio is an indication of confidence. As F-ratio increases it becomes less likely that differences in the outcome of the test are due to chance. If the factors have no effect then the F-ratio will be near a value of one. The confidence interval indicates that 95 percent of the time the coefficients in the model should fall within the interval given.

Regarding the term power that was mentioned in the body of the report, using an α-error cut-off of 21 percent (i.e. the highest confidence term not included in the model had 21 percent alpha error associated with it) the following chart could be produced. Power, which is defined as 1 - β-error, indicates how likely one is to miss a change in the response variable. Power quantifies how likely it is there is a term in the model that creates a difference of some size. The curve in Figure C-1 shows the β-error of this test. As shown below the test was capable of detecting a 10 energy height feet change 99.9 percent of the time.

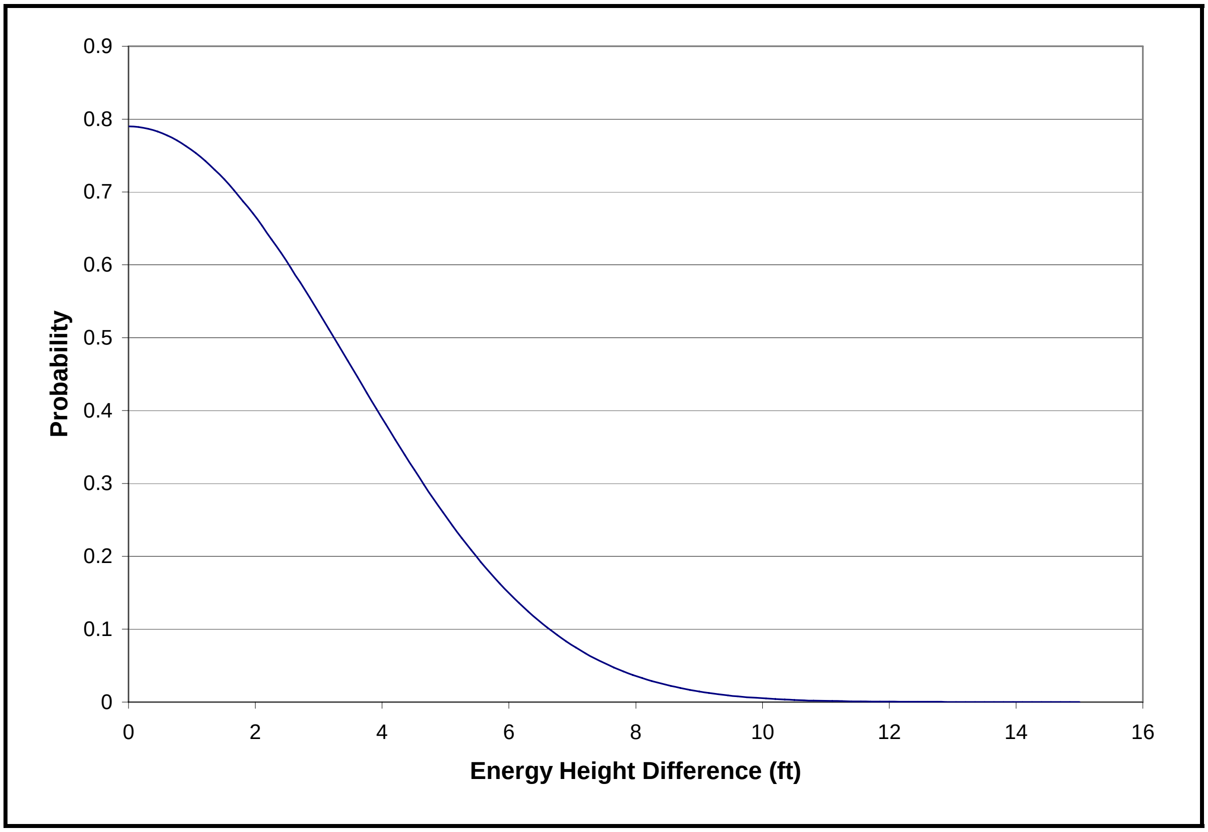

Figure 87. Plot of the Chances of Missing a Difference in Energy Height

Appendix D. Total Energy Probe Theory

(Adapted from notes by Mr. Joe Wurts, Lockheed-Martin Engineer and dynamic soaring expert.)

The total energy for an aircraft is defined as the sum of the kinetic energy, and the potential energy due to altitude and gravity.

$$E = \tfrac{1}{2} mV^2 + mgh \tag{75}$$

Where m is the mass, V is velocity, g is acceleration due to gravity, and h is the current altitude.

Dividing by mg allows us to define specific energy height (units in feet):

$$E_s = \frac{V^2}{2g} + h \tag{76}$$

The first term in this equation is the kinetic energy expressed in units of altitude, and is the amount of energy gained when something drops from the specific total energy altitude to the current altitude. The second term is simply the current altitude.

The change in static atmospheric pressure between the total energy height and the current height can be defined as

$$\Delta p = -\rho g \Delta h \tag{77}$$

assuming that the change in air density between these two altitudes is small compared to the total density (i.e., incompressible theory, which holds up quite well for sailplanes). Here ρ is air density and Δh is the difference in altitude between the total energy height and the current altitude.

Then from the second equation above, and assuming a constant total energy, it can be shown that:

$$\Delta h = \frac{V^2}{2g} \tag{78}$$

Substituting Δh from Eq. (77) into Eq. (78) provides the definition of the change in static pressure between the total energy height and the current height as:

$$\Delta p = -\tfrac{1}{2}\rho V^2 \tag{79}$$

From Bernoulli's equation we know the dynamic pressure due to the flight velocity is:

$$\bar{q} = \tfrac{1}{2}\rho V^2 \tag{80}$$

The $\bar{q}$ term is the difference between the total pressure and the static pressure measured by a Pitot-static tube, assuming the c_p on the total pressure is +1. By comparing Eq. (79) and Eq. (80) the conclusion can be drawn that the change in static pressure between the total energy height and the current height is the negative of the dynamic pressure. To obtain the total energy height in terms of pressure, all one needs to do is find a measurement of negative dynamic pressure, i.e. find a source for a c_p of -1, and measure the pressure from this source.

The sailplane community long ago worked this out, and found that a suitable source of negative dynamic pressure can be obtained on the back portion of a cylinder oriented perpendicular to the airflow. An altimeter that is connected to the same line as a typical total energy variometer that is mounted in a sailplane will show the total energy height as its displayed altitude. Neglecting drag, the altitude shown on the altimeter would be the altitude that one could achieve if one converted the flight speed back into altitude.

Appendix E. Flight Test Results

The table below shows the data points collected during the course of the test window. The data shaded in gray was not used in the data analysis because the wind data was questionable.

Table 10. 80-90 KIAS Entry Speed Data Points

Date	Time (L)	Hairpin or Anti-Hairpin	Aircrew	Entry Airspeed (KIAS)	Entry Altitude Baro Inertial(ft)	Wind Shear (1/s)	Wind Direction	Mnvr Run-In Heading	Pitot-static ΔEs	Pitot-static Max Es	Geometric ΔEs	Geometric Max Es	Exit Airspeed (KIAS)	Exit Altitude (ft)	
10-Apr-06	9:13:25	Anti-Hairpin	Baase/Ryan	80	2801	-0.005	235	218	-91	0	-69	53	67	2830	NOSHEAR
10-Apr-06	9:11:23	Hairpin	Baase/Ryan	87	3506	-0.010	225	011	-182	0	-123	0	64	3563	
10-Apr-06	9:12:16	Hairpin	Baase/Ryan	80	3158	-0.007	235	014	-110	25	-113	0	68	3165	
10-Apr-06	9:30:29	Hairpin	Baase/Ryan	86	2772	-0.005	235	026	-159	42	-171	0	69	2789	
26-Apr-06	9:06:46	Anti-Hairpin	Falls/Eckberg	84	2878	-0.009	230	135	-124	4	-112	6	71	2880	
10-Apr-06	12:23:22	Anti-Hairpin	Gordon/Eckberg	86	3750	-0.007	235	146	-167	0	-133	30	69	3760	
24-Apr-06	8:54:10	Anti-Hairpin	Falls/Smith	85	2726	-0.004	231	48	-151	0	-149	0	68	2738	
14-Apr-06	8:31:39	Anti-Hairpin	Falls/Erb	89	2605	0.002	235	190	-180	8	-182	34	69	2610	
24-Apr-06	7:41:45	Anti-Hairpin	Baase/Ryan	84	2914	0.003	300	26	-136	4	-80	61	71	2903	
24-Apr-06	7:54:52	Anti-Hairpin	Baase/Ryan	84	3306	0.010	340	231	-145	7	-119	0	66	3320	
26-Apr-06	9:01:19	Anti-Hairpin	Falls/Eckberg	85	6009	0.010	145	183	-158	0	-145	0	66	6030	
10-Apr-06	12:09:23	Hairpin	Gordon/Eckberg	85	3400	-0.007	235	150	-177	0	-152	0	66	3390	
3-May-06	7:25:37	Hairpin	Gordon/Eckberg	86	3031	-0.005	270	145	-241	0	-215	0	61	3026	
14-Apr-06	8:19:05	Hairpin	Falls/Erb	87	2603	0.000	235	193	-156	0	-77	53	70	2605	
24-Apr-06	7:38:49	Hairpin	Baase/Ryan	85	4055	0.003	320	49	n/a	9	-199	2	85	4055	
24-Apr-06	9:35:30	Hairpin	Baase/Eckberg	84	3626	0.004	240	177	n/a	3	-89	0	72	3636	
24-Apr-06	9:36:47	Hairpin	Baase/Eckberg	88	3069	0.004	240	360	-158	1	-120	0	80	3055	
3-May-06	7:20:48	Hairpin	Gordon/Eckberg	85	5691	0.008	023	319	-165	3	-115	26	66	5712	
24-Apr-06	9:49:41	NO SHEAR	Baase/Eckberg	84	3684	0.000	240	182	-169	0	-112	0	65	3708	
24-Apr-06	9:50:48	NO SHEAR	Baase/Eckberg	85	3091	0.000	200	005	-152	0	-146	0	68	3104	
Date	Time (L)	Hairpin or Anti-Hairpin	Aircrew	Entry Airspeed (KIAS)	Entry Altitude Baro Inertial(ft)	Wind Shear (1/s)	Wind Direction	Mnvr Run-In Heading	Pitot-static ΔEs	Pitot-static Max Es	Geometric ΔEs	Geometric Max Es	Exit Airspeed (KIAS)	Exit Altitude (ft)	
24-Apr-06	10:34:34	Anti-Hairpin	Baase/Eckberg	84	3504	0.016	240	137	-174	10	-145	0	69	3485	SIGNIFICANT SHEAR
3-May-06	8:47:36	Anti-Hairpin	Baase/Ryan	84	3984	0.016	305	231	-129	0	-83	10	70	4001	
26-Apr-06	8:59:23	Anti-Hairpin	Falls/Eckberg	85	7064	0.018	098	360	-164	0	-143	0	70	7072	
14-Apr-06	7:58:32	Anti-Hairpin	Falls/Erb	88	3870	0.024	192	360	-145	0	-138	0	73	3900	
3-May-06	8:06:54	Anti-Hairpin	Gordon/Eckberg	84	3978	0.034	003	231	-178	0	-147	0	67	3975	
28-Apr-06	9:30:51	Hairpin	Falls/Eckberg	84	3096	0.011	330	093	-132	0	-99	0	72	3110	
19-Apr-06	7:50:34	Hairpin	Gordon/Eckberg	85	2600	0.012	All Over	325	-160	0	-150	0	68	2600	
26-Apr-06	9:59:58	Hairpin	Falls/Eckberg	84	5948	0.013	090	180	-153	9	-145	0	72	5936	
24-Apr-06	10:21:31	Hairpin	Baase/Eckberg	85	3435	0.015	240	143	-124	0	-100	0	73	3441	
26-Apr-06	8:34:46	Hairpin	Falls/Eckberg	85	6027	0.015	135	180	-148	0	-122	0	72	6010	
24-Apr-06	9:05:41	Hairpin	Falls/Smith	85	2797	0.016	157	238	-134	0	-98	0	70	2820	
3-May-06	7:52:40	Hairpin	Gordon/Eckberg	85	3956	0.016	300	046	-161	0	-132	0	68	3971	
3-May-06	8:28:59	Hairpin	Baase/Ryan	85	3968	0.016	305	046	-143	0	-132	0	71	3975	
26-Apr-06	8:32:44	Hairpin	Falls/Eckberg	84	7077	0.018	098	360	-139	0	-111	0	72	7085	
26-Apr-06	9:57:54	Hairpin	Falls/Eckberg	86	7054	0.018	090	360	-191	0	-154	0	68	7063	
14-Apr-06	8:15:37	Hairpin	Falls/Erb	88	3782	0.019	235	190	-193	0	-150	94	68	3802	
24-Apr-06	7:23:37	Hairpin	Baase/Ryan	85	3342	0.020	310	32	-145	0	-84	0	68	3348	
28-Apr-06	9:29:56	Hairpin	Falls/Eckberg	83	3575	0.030	360	090	-119	20	-103	0	73	3580	
14-Apr-06	8:28:40	Hairpin	Falls/Erb	88	3710	-0.027	235	360	Invalid	0	-183	0	73	3669	NEG SHEAR
24-Apr-06	7:25:27	Hairpin	Baase/Ryan	84	2599	-0.022	269	209	-139	0	-93	0	67	2616	
24-Apr-06	7:42:57	Anti-Hairpin	Baase/Ryan	84	2502	-0.020	250	214	-109	10	-118	58	66	2549	
24-Apr-06	7:24:24	Hairpin	Baase/Ryan	84	2990	-0.016	310	27	-136	3	-103	0	68	2998	

Table 11. 90-100 KIAS Entry Speed Data Points

Date	Time (L)	Hairpin or Anti-Hairpin	Aircrew	Entry Airspeed (KIAS)	Entry Altitude Baro Intertial (ft)	Wind Shear (1/s)	Wind Direction	Mnvr Run-In Heading	Pitot-static ΔEs	Pitot-static Max Es	Geometric ΔEs	Geometric Max Es	Exit Airspeed (KIAS)	Exit Altitude (ft)	
10-Apr-06	9:29:41	Anti-Hairpin	Baase/Ryan	96	3186	-0.007	235	028	-213	6	-245	0	72	3235	NO SHEAR
10-Apr-06	9:28:27	Anti-Hairpin	Baase/Ryan	99	4020	-0.002	225	209	-258	0	-161	34	72	4054	
10-Apr-06	9:41:44	Hairpin	Baase/Ryan	98	3166	-0.007	235	213	-168	0	-127	59	81	3184	
10-Apr-06	12:22:21	Anti-Hairpin	Gordon/Eckberg	94	4220	-0.007	235	330	-183	12	-170	22	79	4200	
10-Apr-06	12:21:12	Anti-Hairpin	Gordon/Eckberg	96	4800	-0.007	235	160	-183	23	-150	17	79	4840	
21-Apr-06	10:36:37	Anti-Hairpin	Gordon/Ryan	94	3125	-0.004	240	330	-215	5	-182	0	75	3120	
28-Apr-06	9:13:34	Anti-Hairpin	Falk/Eckberg	94	4514	0.004	001	092	-167	0	-134	28	80	4513	
3-May-06	9:23:06	Anti-Hairpin	Baase/Ryan	95	4721	0.005	305	230	-166	9	-133	26	78	4749	
24-Apr-06	8:06:36	Anti-Hairpin	Baase/Ryan	94	3550	0.010	340	228	-200	3	-153	0	71	3580	
14-Apr-06	8:58:49	Anti-Hairpin	Baase/Erb	94	3743	0.010	235	326	-179	0	-167	0	76	3767	
21-Apr-06	12:07:16	Hairpin	Gordon/Eckberg	95	4600	-0.007	235	152	n/a	17	-191	0	74	4650	
10-Apr-06	12:08:21	Hairpin	Gordon/Eckberg	95	3800	-0.007	235	323	-217	0	-165	10	74	3800	
21-Apr-06	10:15:57	Hairpin	Gordon/Ryan	92	3030	0.001	240	328	-190	18	-173	0	71	3040	
28-Apr-06	8:58:32	Hairpin	Falk/Eckberg	94	4523	0.004	001	096	-166	8	-146	3	77	4543	
24-Apr-06	7:40:10	Hairpin	Baase/Ryan	93	3506	0.010	340	233	-146	0	-143	0	77	3523	
17-Apr-06	7:57:17	Hairpin	Baase/Ryan	93	4082	0.005	290	160	-287	0	-287	0	61	4091	

Date	Time (L)	Hairpin or Anti-Hairpin	Aircrew	Entry Airspeed (KIAS)	Entry Altitude Baro Intertial(ft)	Wind Shear (1/s)	Wind Direction	Mnvr Run-In Heading	Pitot-static ΔEs	Pitot-static Max Es	Geometric ΔEs	Geometric Max Es	Exit Airspeed (KIAS)	Exit Altitude (ft)	
28-Apr-06	9:16:12	Anti-Hairpin	Falk/Eckberg	94	3160	0.011	330	273	-217	6	-185	0	72	3157	SIGNIFICANT SHEAR
3-May-06	7:24:17	Anti-Hairpin	Gordon/Eckberg	95	3640	0.011	270	320	-266	0	-206	0	71	3627	
14-Apr-06	9:21:42	Anti-Hairpin	Baase/Erb	94	3858	0.014	235	318	-167	0	-133	18	77	3878	
28-Apr-06	7:45:10	Anti-Hairpin	Falk/Ryan	94	3446	0.019	000	100	-180	0	-174	0	74	3484	
14-Apr-06	9:00:57	Anti-Hairpin	Baase/Erb	93	2911	0.016	235	148	-190	9	-185	17	71	2944	
28-Apr-06	9:14:23	Anti-Hairpin	Falk/Eckberg	95	4015	0.028	003	091	-237	0	-235	0	74	4005	
28-Apr-06	9:15:23	Anti-Hairpin	Falk/Eckberg	95	3507	0.030	360	271	-204	7	-167	0	75	3520	
28-Apr-06	7:44:11	Anti-Hairpin	Falk/Ryan	95	4049	0.030	003	284	-213	8	-224	6	78	4042	
17-Apr-06	7:58:14	Anti-Hairpin	Baase/Ryan	92	3262	0.030	302	336	-268	0	-165	118	61	3288	
17-Apr-06	7:59:07	Hairpin	Baase/Ryan	91	2594	0.021	287	332	-84	56	-79	230	80	2660	
17-Apr-06	9:39:14	Hairpin	Gordon/Erb	95	2700	0.027	234	153	-303	1	-182	2	74	2720	
17-Apr-06	9:57:14	Hairpin	Gordon/Erb	95	2690	0.027	234	140	n/a	0	-167	36	75	2700	
28-Apr-06	9:01:12	Hairpin	Falk/Eckberg	94	3262	0.011	330	274	-182	0	-142	0	79	3260	
3-May-06	9:00:37	Hairpin	Baase/Ryan	95	4781	0.012	305	050	-183	1	-147	0	78	4809	
28-Apr-06	7:21:55	Hairpin	Gordon/Eckberg	95	5026	0.013	320	318	n/a	0	-162	4	72	5070	
14-Apr-06	7:28:24	Hairpin	Falk/Ryan	94	3519	0.014	340	096	n/a	6	-129	0	79	3546	
14-Apr-06	8:50:27	Hairpin	Baase/Erb	93	2819	0.021	235	150	-208	0	-152	53	71	2836	
14-Apr-06	9:24:34	Hairpin	Baase/Erb	94	2750	0.024	235	160	-242	0	-186	-21	69	2769	
28-Apr-06	8:59:17	Hairpin	Falk/Eckberg	94	4045	0.028	003	094	-146	10	-121	25	80	4065	
28-Apr-06	9:00:21	Hairpin	Falk/Eckberg	96	3608	0.030	360	272	-158	0	-136	0	82	3620	
28-Apr-06	7:27:07	Hairpin	Falk/Ryan	97	4080	0.040	010	281	-202	0	-160	0	78	4099	

Table 12. 100-110 KIAS Entry Speed Data Points

Date	Time (L)	Hairpin or Anti-Hairpin	Aircrew	Entry Airspeed (KIAS)	Entry Altitude Baro Inertial (ft)	Wind Shear (1/s)	Wind Direction	Mnvr Run-In Heading	Pilot data ΔEs	Pilot data Max Es	Geometric ΔEs	Geometric Max Es	Exit Airspeed (KIAS)	Exit Altitude (ft)	
10-Apr-06	9:10:22	Hairpin	Baase/Ryan	101	4007	-0.002	225	200	-253	0	-175	0	81	3991	NO SHEAR
21-Apr-06	10:14:33	Anti-Hairpin	Gordon/Ryan	101	3760	-0.001	250	140	-275	0	-255	0	80	3770	
24-Apr-06	8:53:06	Anti-Hairpin	Falls/Smith	104	3080	0.001	188	228	-221	0	-163	0	85	3096	
3-May-06	8:05:27	Anti-Hairpin	Gordon/Eckberg	103	4715	0.005	315	050	-275	0	-239	0	80	4720	
24-Apr-06	10:33:14	Anti-Hairpin	Baase/Eckberg	104	3956	0.006	240	320	-252	0	-237	0	86	3960	
19-Apr-06	7:49:21	Anti-Hairpin	Gordon/Eckberg	103	3020	0.008	60	140	-286	0	-247	0	75	3060	
3-May-06	9:24:26	Anti-Hairpin	Baase/Ryan	104	3952	0.009	270	053	-218	7	-207	0	90	3918	
26-Apr-06	7:48:39	Anti-Hairpin	Falls/Eckberg	104	6060	0.010	145	360	-263	0	-212	0	86	6043	
3-May-06	8:46:01	Anti-Hairpin	Baase/Ryan	104	4775	0.010	315	053	-254	0	-218	0	86	4767	
21-Apr-06	10:35:29	Hairpin	Gordon/Ryan	108	3900	-0.001	250	150	-298	0	-268	0	80	3930	
24-Apr-06	8:40:33	Hairpin	Falls/Smith	103	3065	0.001	188	236	-222	0	-169	0	82	3105	
24-Apr-06	9:33:36	Hairpin	Baase/Eckberg	103	4219	0.003	320	051	n/a	21	-234	0	89	4188	
3-May-06	7:51:15	Hairpin	Gordon/Eckberg	105	4803	0.005	315	047	-299	0	-257	0	80	4823	
19-Apr-06	7:07:33	Hairpin	Gordon/G-man	103	3140	0.008	60	145	-261	4	-214	0	78	3170	
3-May-06	8:27:20	Hairpin	Baase/Ryan	104	4800	0.008	325	227	-269	0	-194	0	80	4827	
24-Apr-06	10:20:28	Hairpin	Baase/Eckberg	105	3811	0.009	240	322	-219	12	-211	0	88	3790	
3-May-06	7:23:03	Hairpin	Gordon/Eckberg	103	4278	0.010	300	140	-273	0	-257	0	77	4305	
21-Apr	10:12:44	Hairpin	Gordon/Ryan	104	6110	-0.027	170	50	-306	0	-285	0	78	6150	NEG SHEAR
26-Apr-06	9:05:38	Hairpin	Falls/Eckberg	103	3072	-0.013	225	321	-229	0	-170	0	83	3117	
26-Apr-06	8:37:35	Hairpin	Falls/Eckberg	105	3074	-0.013	225	315	-232	0	-163	0	83	3121	

Date	Time (L)	Hairpin or Anti-Hairpin	Aircrew	Entry Airspeed (KIAS)	Entry Altitude Baro Inertial (ft)	Wind Shear (1/s)	Wind Direction	Mnvr Run-In Heading	Pilot data ΔEs	Pilot data Max Es	Geometric ΔEs	Geometric Max Es	Exit Airspeed (KIAS)	Exit Altitude (ft)	
28-Apr-06	8:33:06	Anti-Hairpin	Falls/Eckberg	105	3372	0.011	270	095	-239	0	-185	0	83	3406	SIGNIFICANT SHEAR
24-Apr-06	9:48:29	Anti-Hairpin	Baase/Eckberg	104	4205	0.012	250	050	-251	9	-231	0	82	4230	
26-Apr-06	7:50:07	Anti-Hairpin	Falls/Eckberg	104	6860	0.012	095	180	-254	0	-193	0	84	6885	
21-Apr-06	8:17:47	Anti-Hairpin	Baase/Ryan	104	2754	0.015	220	311	-254	0	-221	0	84	2721	
24-Apr-06	7:53:30	Anti-Hairpin	Baase/Ryan	103	3709	0.019	330	57	-241	0	-192	0	81	3711	
28-Apr	7:43:18	Anti-Hairpin	Falls/Ryan	103	4583	0.019	010	284	-290	0	-185	3	80	4589	
19-Apr-06	9:36:18	Anti-Hairpin	Falls/Smith	101	3218	0.021	17	134	-222	0	-171	2	84	3198	
24-Apr-06	9:16:57	Anti-Hairpin	Falls/Smith	102	3486	0.023	54	56	-226	0	-215	0	85	3465	
21-Apr-06	8:04:52	Anti-Hairpin	Falls/Smith	104	2570	0.023	201	315	262	0	-229	12	85	2612	
26-Apr-06	9:00:17	Anti-Hairpin	Falls/Eckberg	104	6280	0.024	090	360	-253	0	-215	0	84	6290	
19-Apr-06	8:45:03	Anti-Hairpin	Baase/Ryan	104	3158	0.026	65	142	-263	0	-215	0	83	3130	
26-Apr-06	8:58:03	Anti-Hairpin	Falls/Eckberg	104	7506	0.027	095	181	-249	0	-225	0	86	7505	
24-Apr-06	8:51:36	Anti-Hairpin	Falls/Smith	103	4039	0.029	305	57	-237	0	-193	0	84	4039	
3-May-06	9:01:58	Hairpin	Baase/Ryan	104	3985	0.011	270	233	-228	0	-173	0	84	4010	
28-Apr-06	7:57:30	Hairpin	Falls/Ryan	105	4556	0.011	025	277	275	0	-219	30	82	4592	
21-Apr-06	7:28:40	Hairpin	Falls/Forger	106	2535	0.013	210	300	-205	0	-209	0	74	2608	
28-Apr-06	8:12:11	Hairpin	Falls/Ryan	103	3341	0.014	345	275	-195	0	-152	0	84	3380	
21-Apr-06	8:39:27	Hairpin	Baase/Ryan	104	2736	0.018	220	316	-206	37	-178	34	80	2771	
24-Apr-06	9:04:11	Hairpin	Falls/Smith	103	3530	0.021	59	55	-191	3	-166	0	87	3543	
19-Apr-06	9:24:08	Hairpin	Falls/Smith	103	3226	0.021	17	147	-222	0	-162	0	83	3227	
19-Apr-06	8:55:06	Hairpin	Gordon/Eckberg	104	3260	0.023	50	140	n/a	0	-208	0	82	3275	
21-Apr-06	7:54:16	Hairpin	Falls/Smith	105	2692	0.023	201	312	-247	0	-202	0	86	2668	
26-Apr-06	9:58:54	Hairpin	Falls/Eckberg	102	6220	0.024	095	360	-210	3	-178	0	85	6240	
26-Apr-06	8:33:54	Hairpin	Falls/Eckberg	104	6268	0.024	095	177	-160	0	-171	0	87	6277	
19-Apr-06	9:06:33	Hairpin	Baase/Ryan	104	3179	0.026	65	137	-217	0	-160	17	86	3187	
26-Apr-06	8:31:33	Hairpin	Falls/Eckberg	105	7437	0.027	095	360	-249	12	-201	0	84	7468	
26-Apr-06	9:56:37	Hairpin	Falls/Eckberg	103	7520	0.027	093	184	-184	12	-142	57	90	7535	
24-Apr-06	8:39:01	Hairpin	Falls/Smith	103	3945	0.029	305	54	-189	0	-140	0	86	3975	
28-Apr-06	7:58:36	Hairpin	Falls/Ryan	104	3866	0.032	360	097	-214	4	-189	0	87	3874	
28-Apr-06	7:26:17	Hairpin	Falls/Ryan	105	4542	0.036	010	269	-243	0	-181	8	85	4561	

Appendix F. Rational for Discarded Data Sets

Several data points from two different days were discarded from both analysis methods because the wind data from these two days were either suspect or not collected in a timely manner. For instance, most of the data points flown by pilot 1 at 95 KIAS occurred on 10 April 2006, which happened to coincide with minimal weather data collection. Specifically, only one weather balloon was launched, and furthermore, the weather data was collected about 2 hours after the data flights were completed. Not only did this prevent the team from targeting shear layers during the flights, but it called into question the accuracy of the wind data attributed to these test points. This emphasizes the need for timely weather data collected at short time intervals.

Additional data points were removed from the data analysis for flights on 17 April 2006. These data points were removed because the wind data gathered during the test points were questionable. The data were not gathered using the NASA weather balloons due to a system malfunction. Instead data collected from an Edwards AFB balloon launched prior to the flights was used as the weather reference. However, the wind speeds shown by the balloon did not match the winds experienced by the test team or the wind calls from the control tower. The disparity was likely due to a weather system that was moving through the local area during the testing, which caused localized wind shears. All three of the test points that occurred during a single sortie on this day showed up as significant outliers. Of particular note is that, a hairpin maneuver flown during this sortie resulted in a loss of only 15 feet of energy height. During this maneuver the aircrew clearly experienced the existence of a strong shear layer (much stronger than any shear layers felt throughout the rest of the program). (The aircrew generally noted shear layer entry throughout the test program by the existence of turbulence, which could be felt in the seat of the pants.) However, the wind data from the USAF balloon did not show this shear layer.

This sortie provided a good indication that not only does the phenomenon of dynamic soaring exist, but the effect of the phenomenon increases with increasing wind shear strength. Additionally, the data from 17 April indicate the need for precise and accurate wind data collection capabilities.

These data from 10 and 17 April 2006 are shaded in gray in the tables in Appendix E. Flight Test Results .

Appendix G. Cooper-Harper Rating Scale

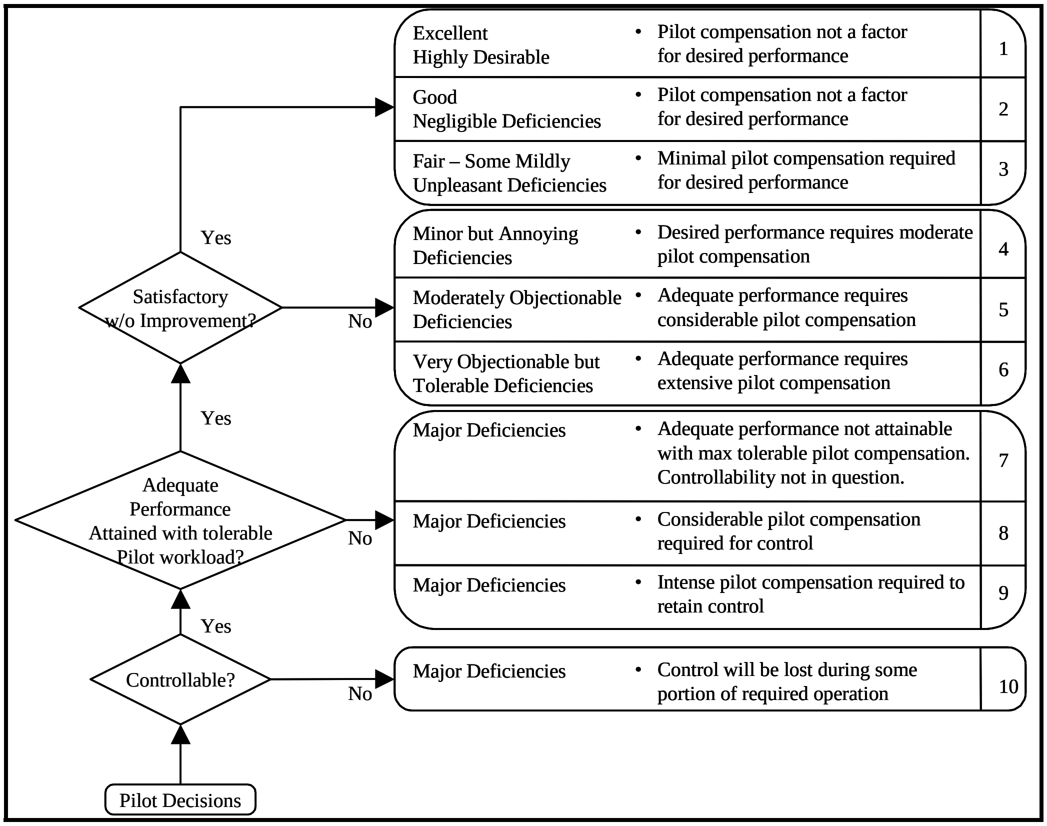

Excellent Highly Desirable	• Pilot compensation not a factor for desired performance	1
Good Negligible Deficiencies	• Pilot compensation not a factor for desired performance	2
Fair – Some Mildly Unpleasant Deficiencies	• Minimal pilot compensation required for desired performance	3
Minor but Annoying Deficiencies	• Desired performance requires moderate pilot compensation	4
Moderately Objectionable Deficiencies	• Adequate performance requires considerable pilot compensation	5
Very Objectionable but Tolerable Deficiencies	• Adequate performance requires extensive pilot compensation	6
Major Deficiencies	• Adequate performance not attainable with max tolerable pilot compensation. Controllability not in question.	7
Major Deficiencies	• Considerable pilot compensation required for control	8
Major Deficiencies	• Intense pilot compensation required to retain control	9
Major Deficiencies	• Control will be lost during some portion of required operation	10

Figure 88. Cooper-Harper Ref. NASA TND-5153

Vita

Captain Randel J. Gordon was born in Poughkeepsie, New York. He graduated from Wallkill Senior High School in Wallkill, New York in 1994. He entered the US Air Force Academy immediately after graduation and earned a Bachelor of Science degree in Aeronautical Engineering, graduated in the top 10% of his class, and was commissioned in May of 1998.

His first assignment was at Laughlin AFB as a student in Specialized Undergraduate Pilot Training in August of 1998. He was the Distinguished Graduate of class 99-13 at Laughlin and received his Pilot rating in August of 1999. Upon graduation of SUPT, Capt Gordon was assigned to Introduction to Fighter Fundamentals (IFF) in Columbus AFB, MS where he again was the Distinguished Graduate of his class. Following this assignment he was sent to Tyndall AFB to learn to fly F-15C's. In the summer of 2005, Capt Gordon married. He was subsequently assigned to the 19th Fighter Squadron and 3rd Operations Support Squadron at Elmendorf AFB AK achieving numerous awards for flight leadership and officership. Capt Gordon was accepted to the joint Air Force Institute of Technology / Test Pilot School program in the winter of 2003. This coincided with the birth of his son, Marcus Gordon in December of 2003.

Capt Gordon graduated in the top three order of merit from his US Air Force Test Pilot School class in June of 2006 and is currently assigned to the 40th FTS at Eglin AFB FL to fly the F-15C and F-15E. He has flown over 50 different aircraft and holds FAA ratings as a single engine Commercial pilot, and Sailplane Commercial pilot.

REPORT DOCUMENTATION PAGE	*Form Approved* *OMB No. 074-0188*

1. REPORT DATE *(DD-MM-YYYY)* Sep 2006	**2. REPORT TYPE** **Master's Thesis**	**3. DATES COVERED** *(From – To)* Mar 2004 - Sep 2006

4. TITLE AND SUBTITLE Optimal Dynamic Soaring for Full Size Sailplanes	**5a. CONTRACT NUMBER**
	5b. GRANT NUMBER
	5c. PROGRAM ELEMENT NUMBER
6. AUTHOR(S) Gordon, Randel J. Captain USAF	**5d. PROJECT NUMBER**
	5e. TASK NUMBER
	5f. WORK UNIT NUMBER
7. PERFORMING ORGANIZATION NAMES(S) AND ADDRESS(S) Air Force Institute of Technology Graduate School of Engineering and Management (AFIT/EN) 2950 Hobson Way WPAFB OH 4543-7765	**8. PERFORMING ORGANIZATION REPORT NUMBER** **AFIT/GAE/ENY06-S04**
9. SPONSORING/MONITORING AGENCY NAME(S) AND ADDRESS(ES) Air Force Flight Test Center 412th Test Wing USAF Test Pilot School 220 South Wolfe Ave Edwards AFB CA 93524-6485	**10. SPONSOR/MONITOR'S ACRONYM(S)**
	11. SPONSOR/MONITOR'S REPORT NUMBER(S)

12. DISTRIBUTION/AVAILABILITY STATEMENT
APPROVED FOR PUBLIC RELEASE; DISTRIBUTION UNLIMITED.

13. SUPPLEMENTARY NOTES

14. ABSTRACT

Dynamic soaring is a unique flying technique designed to allow air vehicles to extract energy from horizontal wind shears. Dynamic soaring has been used by seabirds like the Albatross to fly hundreds of kilometers a day across the ocean. Small hobby radio controlled sailplanes have also used this technique to achieve sustained speeds of over 200 miles per hour from just a simple hand toss. Dynamic soaring, however, has never before been studied for use on full size aircraft. The primary goal of this research was to prove or disprove the viability of dynamic soaring for enhancing a full size aircraft's total energy by using a manned sailplane as a demonstration air vehicle. The results of this study will have a direct impact on the sport of soaring, as well as the design of the next generation of large, sailplane-like, robotic planetary explorers for the National Aeronautics and Space Administration (NASA).

This research began with a point mass optimization study of an L-23 Super Blanik sailplane. The primary goal of this study was to develop and analyze optimal dynamic soaring trajectories for full size sailplanes. A prototype 6 degrees of freedom (DOF) flight simulator was then developed at the Air Force Research Laboratory's Aerospace Vehicles Technology Assessment and Simulation Branch (AFRL/VACD) and implemented on their Large Amplitude Multi-Mode Aerospace Research Simulator (LAMARS). This simulator helped to validate the dynamic soaring aircraft equations of motion derived for this research and built operational simulator development experience. This experience was then incorporated into a full dynamic soaring research simulator developed at the NASA Dryden Flight Research Facility (NASA DFRC). This NASA simulator was used to develop advanced dynamic soaring flight displays, flight test techniques, and aircrew coordination procedures. Flight test were successfully accomplished using an instrumented L-23 Super Blanik sailplane and advanced weather monitoring equipment. Through modeling and simulation, flight test, and mathematical analysis, this research provided the first documented proof of the energy benefits realized using dynamic soaring techniques in full size sailplanes.

15. SUBJECT TERMS

SENIOR ShWOOPIN, dynamic soaring, L-23 Super Blanik, Flight Testing, Atmospheric Wind Gradients, Atmospheric Energy Extraction, Wind Shear, Sailplanes, Gliders, Gliding, Wind Velocity, Aerodynamic drag, drag Reduction, lift to drag Ratio, Dynamic Optimization

16. SECURITY CLASSIFICATION OF:			**17. LIMITATION OF ABSTRACT**	**18. NUMBER OF PAGES**	**19a. NAME OF RESPONSIBLE PERSON** Paul A. Blue, Maj, USAF
REPORT U	**ABSTRACT** U	**c. THIS PAGE** U	UU	185	**19b. TELEPHONE NUMBER** *(Include area code)* (937) 255-3636, ext 4714 (paul.blue@afit.edu)

Standard Form 298 (Rev. 8-98)